

Theoretical Description of Excited States and Optical Properties of Transition Metal Complexes in the Framework of the Bethe–Salpeter Equation

Zur Erlangung des akademischen Grades einer

DOKTORIN DER NATURWISSENSCHAFTEN

(Dr. rer. nat)

von der KIT-Fakultät für Chemie und Biowissenschaften

des Karlsruher Instituts für Technologie (KIT)

genehmigte

DISSERTATION

von

M.Sc. Xin Gui

1. Referent: Prof. Dr. Willem M. Klopper

2. Referent: PD Dr. Michael E. Harding

Tag der mündlichen Prüfung: 8. Dezember 2020

Contents

1	Introduction	1
2	Theoretical background	3
2.1	Density functional theory (DFT)	3
2.1.1	The Kohn–Sham equations	3
2.1.2	Time-dependent DFT: linear response theory	4
2.2	Many-body Green’s function	8
2.2.1	The quasiparticle equations	8
2.2.2	One-particle Green’s function and <i>GW</i> approximation	9
2.2.3	Response functions	12
2.2.4	Two-particle Green’s function and Bethe–Salpeter equation	14
2.3	Calculation of quasiparticle energies in <i>GW</i>	16
2.3.1	Separation of self-energy	16
2.3.2	<i>GW</i> variants with different levels of self-consistency	18
2.3.3	<i>GW</i> variants for evaluation of correlation self-energy	18
2.4	Computational details	22
3	Performance assessment of BSE with different <i>GW</i> starting points	25
3.1	Valence excited states	25
3.2	Charge-transfer states	29
3.3	Timings	31
3.4	Conclusion	34
4	Photoinitiated charge-transfer in a triangular silver(I) hydride complex	35
4.1	Introduction	35
4.2	Structural examination and geometry optimization	35
4.3	Optical properties and electronic structure	37
4.4	Conclusion	40
5	A tetranuclear silver(I) iodide complex: cube and chair isomers	43

5.1	Introduction	43
5.2	Cubane-like isomer	44
5.2.1	Structural examination and geometry optimization	44
5.2.2	Absorption spectra	44
5.3	Chair-like isomer	48
5.3.1	Geometry optimization	48
5.3.2	Absorption spectra	49
5.4	Conclusion	49
6	Photosensitizers based on heteroleptic copper(I) complexes	53
6.1	Introduction	53
6.2	Copper(I) complexes with triazole–quinoline/quinoxaline ligands	54
6.2.1	Structural examination and geometry optimization	54
6.2.2	Absorption spectra	54
6.2.3	Structures of the first triplet excited state (T_1)	58
6.3	Copper(I) complexes with triazole–pyridine ligands	60
6.3.1	Structural examination and geometry optimization	60
6.3.2	Absorption spectra	60
6.3.3	Rotation of the benzene bridging unit	60
6.3.4	Structures of the first triplet excited state (T_1)	66
6.4	Conclusion	67
7	Highly luminescent gold(III) pincer complexes	69
7.1	Introduction	69
7.2	Geometry optimization	70
7.3	Excited state calculations at the S_0 geometry	71
7.4	Two-component excited state calculations at the T_1 geometry	72
7.5	Conclusion	78
8	Bimetallic gold(I) amidinate complexes as model systems for investigation of photophysical properties	81
8.1	Introduction	81
8.2	Structural examination and geometry optimization	82
8.3	Excited state calculations at the S_0 geometry	84
8.4	Two-component excited state calculations at the T_1 geometry	86
8.5	Conclusion	88

9 Summary	91
A Appendix	95
A.1 Diagrammatic representation	95
B List of Publications	97
C Permissions for reuse or republication	99

List of notations

Abbreviations

Chap.	chapter
Appx.	appendix
Eq.(s)	equation(s)
Ref.(s)	reference(s)
Fig.	figure
Tab.	table

Acronyms

HF	Hartree–Fock
KS	Kohn–Sham
QP	quasiparticle
RPA	random phase approximation
(TD)DFT	(time-dependent) density functional theory
MBPT	many-body perturbation theory
BSE	Bethe–Salpeter equation
RI	resolution-of-the-identity
HOMO	highest occupied molecular orbital
LUMO	lowest unoccupied molecular orbital
LC	ligand-centered
MLCT	metal-to-ligand charge transfer

Symbols

i, j, k, \dots	occupied orbitals
a, b, c, \dots	virtual orbitals
p, q, r, \dots	arbitrary orbitals

$$v_{pq,rs} = (pq|sr) = \iint d\mathbf{r}_1 d\mathbf{r}_2 \phi_p^*(\mathbf{r}_1) \phi_q(\mathbf{r}_1) r_{12}^{-1} \phi_s^*(\mathbf{r}_2) \phi_r(\mathbf{r}_2)$$

1 Introduction

A fundamental understanding of multinuclear transition metal complexes and clusters will lead to new applications in the field of photonics, optoelectronics and photocatalysis. Various experimental techniques have been developed for synthesis and characterization of ligand-stabilized multimetallic complexes, including synthetic molecular chemistry, mass spectrometry, UV/Vis absorption and luminescence spectroscopy. The main focus of this thesis, as funded by the Transregional Collaborative Research Center "Cooperative Effects in Homo- and Heterometallic Complexes (3MET)", lies on the theoretical description of the electronic structure and optical properties of di-, tri-, and tetranuclear transition metal complexes containing the coinage metals copper, silver and gold, hoping to provide more insights into the multimetallic complexes with typically three (but also two or four) metal centers.

The goals of this thesis include structure determination in ground and electronically excited states, *ab initio* calculation of vertical and adiabatic excitation energies, and most importantly, prediction and interpretation of absorption and emission spectra of oligonuclear transition metal complexes. On the other hand, the intermetallic cooperative interactions^[1] within d^8/d^{10} electron configurations, which is the key topic of 3MET, will also be investigated here. Various examples on short $d^{10}-d^{10}$ distances are documented for all three coinage metals. Instead of repelling each other, attractive interactions between two closed-shell metal cations are very commonly observed, which are weaker than most covalent or ionic bonds but stronger than van der Waals interactions. This metallophilic attraction can lead to the formation of dimers, oligomers and polymers, and their electronic structures and luminescence behavior are strongly affected by the arrangement of the metal centers. Therefore, it is interesting to see how the catalytic and optical properties are influenced by the cooperativity between metal centers.

Computational methods based on time-dependent density functional theory (TDDFT) and Green's function, namely *GW* approximation and Bethe-Salpeter equation (BSE) will be employed in this thesis. Nowadays, TDDFT in its effective linear-response (LR) formalism has been the most applied *ab initio* method for excited states. This popularity is due to the favorable N^4 scaling with system size, the availability of analytic first and second derivatives, and ease of coupling to environmental models. However, it suffers from strong dependency on the exchange-correlation functional, and it is system and state dependent.^[2] In recent years, the

GW/BSE approach has attracted considerable interest in computing molecular excitation energies, and highly promising results have been presented.^[3–23] The BSE formalism is very similar to TDDFT in the language of linear response and hence shares the same N^4 scaling with system size as TDDFT, whereas it can overcome the TDDFT limitations associated with charge-transfer (CT) excitations, which are particularly problematic for standard exchange-correlation functionals.^[24,25] Charge-transfer states play a central role in many 3MET complexes, either with metal-to-ligand or ligand-to-metal character. Therefore, an appropriate description of such CT excitations is crucial for computing optical spectroscopy.

Since BSE computations normally require quasiparticle energies from preceding GW calculations on input, the quality of the GW energy levels strongly affects the accuracy of the BSE excitation energies. There are various GW starting points for the BSE step. The non-self-consistent $GW(G_0W_0)$ ^[26] is computationally very efficient, but the lack of self-consistency results in great dependency on the reference orbitals, which is undesirable. On the other hand, fully self-consistent GW theory (scGW)^[27–29] seems computationally too expensive. Therefore, partially self-consistent schemes such as eigenvalue-only self-consistent GW (evGW)^[30] and quasiparticle self-consistent GW (qsGW)^[31,32] can be good alternatives. The evGW scheme admittedly still depends on the reference orbitals, yet much less than G_0W_0 , while qsGW totally removes the dependency on the starting points, and it is also computationally more demanding than evGW. The quasiparticle energies can be computed for *all* orbital levels using the full spectral representation of the density response function (SR-GW).^[5] However, it is computationally very expensive and scales as N^6 with system size. When quasiparticle energies are only needed for a few orbitals near the Fermi level, the analytic continuation (AC-GW)^[30,33–35] and contour deformation (CD-GW)^[36] variants provide efficient low-scaling (N^4) alternatives to the computation of correlation self-energy. Compared to AC-GW, CD-GW yields more robust results for core orbitals, which are critical for accurate description of core-level spectroscopy.

This thesis is organized as follows. First, the quantum chemistry methods used in the present work, namely TDDFT and GW/BSE, are briefly recapitulated in Chap. 2. Then, an extensive accuracy assessment of TDDFT and GW/BSE methods is given in Chap. 3 for singlet and triplet valence excited states, as well as charge-transfer excited states, which provides benchmark for further real-world applications. Next, multiple applications of TDDFT and GW/BSE to transition metal complexes are presented, including a trinuclear silver(I) hydride complex (Chap. 4) and a tetranuclear silver(I) halide complex (Chap. 5), a series of heteroleptic copper(I) complexes as potential candidates for photosensitizers (Chap. 6), a series of highly luminescent gold(III) pincer complexes (Chap. 7) and a series of dinuclear amidinate gold(I) complexes as model systems for investigation of photophysical properties (Chap. 8). Lastly, the main conclusions of this thesis are summarized in Chap. 9.

2 Theoretical background

In this chapter, the quantum chemistry methods used in the present work will be briefly reviewed. A comprehensive aspect of the underlying fundamental principles of theoretical chemistry and computational methods can be found in many textbooks^[37–39], and thus will not be described here in every detail. Since my work has been mainly concerned with the application of the methods rather than the implementation or development, I will only present the key ideas and equations behind the related methods, namely time-dependent density functional theory (TDDFT) and Green’s function based Bethe–Salpeter equation (BSE). The main theoretical frameworks of TDDFT and *GW*/BSE will be outlined and compared, since these two methods share similarities in many aspects. The details of derivation can be found in Ref.s 40 and 41 for TDDFT, and in Ref.s 42 and 43 for *GW*/BSE.

2.1 Density functional theory (DFT)

2.1.1 The Kohn–Sham equations

In the Kohn–Sham (KS) scheme^[44,45], an interacting electrons system can be described in terms of an auxiliary non-interacting electrons system that has exactly the same ground state electron density as the real system, and the Kohn–Sham energies and wavefunctions can be obtained by solving the Schrödinger equation

$$\left[-\frac{1}{2}\nabla^2 + V_{\text{ext}}(\mathbf{r}) + V_{\text{H}}(\mathbf{r}) + V_{\text{XC}}(\rho(\mathbf{r})) \right] \phi_i(\mathbf{r}) = \varepsilon_i \phi_i(\mathbf{r}) \quad (2.1)$$

with the density given by

$$\rho(\mathbf{r}) = \sum_i \phi_i^*(\mathbf{r})\phi_i(\mathbf{r}) \quad (2.2)$$

where V_{ext} , V_{H} and V_{XC} are the external potential (i.e. nuclear attraction and any applied field), the Hartree potential (i.e. Coulomb repulsion), and the exchange-correlation potential, respectively.

2.1.2 Time-dependent DFT: linear response theory

In linear response (LR) theory^[40], the density induced by an external time-dependent (TD) perturbative field can be expressed in terms of the real interacting system as

$$\rho^{(1)}(\mathbf{r}, t) = \int d\mathbf{r}' \chi(\mathbf{r}, \mathbf{r}', t - t') V_{\text{ext}}(\mathbf{r}', t') \quad (2.3)$$

or in terms of the fictitious non-interacting system as

$$\rho^{(1)}(\mathbf{r}, t) = \int d\mathbf{r}' \chi_0(\mathbf{r}, \mathbf{r}', t - t') V_{\text{tot}}(\mathbf{r}', t') \quad (2.4)$$

The response functions χ and χ_0 are called polarizabilities of the interacting and non-interacting systems, respectively.

Analogous to the static KS equation, V_{tot} is defined as

$$\begin{aligned} V_{\text{tot}}(\mathbf{r}, t) &= V_{\text{ext}}(\mathbf{r}, t) + V_{\text{H}}(\mathbf{r}, t) + V_{\text{XC}}(\rho(\mathbf{r}), t) \\ &= V_{\text{ext}}(\mathbf{r}, t) + \int d\mathbf{r}' v(\mathbf{r}, \mathbf{r}') \rho(\mathbf{r}', t') + \int d\mathbf{r}' f_{\text{XC}}(\mathbf{r}, \mathbf{r}', t, t') \rho(\mathbf{r}', t') \end{aligned} \quad (2.5)$$

where $f_{\text{XC}} = \delta V_{\text{XC}} / \delta \rho$ is the exchange-correlation kernel that takes into account all the dynamical exchange and correlation effects.

Hence, the two response functions are related via Eq.s (2.3) to (2.5) as

$$\begin{aligned} \chi &= \frac{\delta \rho}{\delta V_{\text{ext}}} = \frac{\delta \rho}{\delta V_{\text{tot}}} \frac{\delta V_{\text{tot}}}{\delta V_{\text{ext}}} = \chi_0 \left(\frac{\delta V_{\text{ext}}}{\delta V_{\text{ext}}} + \frac{\delta V_{\text{H}}}{\delta V_{\text{ext}}} + \frac{\delta V_{\text{XC}}}{\delta V_{\text{ext}}} \right) \\ &= \chi_0 \left(1 + \frac{\delta V_{\text{H}}}{\delta \rho} \frac{\delta \rho}{\delta V_{\text{ext}}} + \frac{\delta V_{\text{XC}}}{\delta \rho} \frac{\delta \rho}{\delta V_{\text{ext}}} \right) \\ &= \chi_0 + \chi_0 (v + f_{\text{XC}}) \chi \end{aligned} \quad (2.6)$$

The Kubo formula^[46] for the response function reads

$$\chi(\mathbf{r}, \mathbf{r}', \tau) = -\theta(\tau) \langle \Psi_0^N | [\rho(\mathbf{r}, t), \rho(\mathbf{r}', t')] | \Psi_0^N \rangle \quad (2.7)$$

where $|\Psi_0^N\rangle$ is the ground state with N electrons and energy E_0^N ; θ is the Heaviside step function and $\tau = t - t'$; if $\tau > 0$, then $\theta = 1$, otherwise $\theta = 0$.

By introducing the completeness relation for the ground state, and using the relation $\rho(\mathbf{r}, t) = e^{iE_0^N t} \rho(\mathbf{r}) e^{-iE_0^N t}$, Eq. (2.7) becomes

$$\begin{aligned} \chi(\mathbf{r}, \mathbf{r}', \tau) &= -\theta(\tau) \sum_{J \neq 0} \left[\langle \Psi_0^N | \rho(\mathbf{r}) | \Psi_J^N \rangle \langle \Psi_J^N | \rho(\mathbf{r}') | \Psi_0^N \rangle e^{-i(E_J^N - E_0^N)\tau} \right. \\ &\quad \left. - \langle \Psi_0^N | \rho(\mathbf{r}') | \Psi_J^N \rangle \langle \Psi_J^N | \rho(\mathbf{r}) | \Psi_0^N \rangle e^{-i(E_0^N - E_J^N)\tau} \right] \\ &= -\theta(\tau) \sum_{J \neq 0} \left[f_J(\mathbf{r}) f_J^*(\mathbf{r}') e^{-i\mathcal{E}_J \tau} - f_J^*(\mathbf{r}) f_J(\mathbf{r}') e^{i\mathcal{E}_J \tau} \right] \end{aligned} \quad (2.8)$$

where $|\Psi_J^N\rangle$ is the J -th excited state with N electrons and energy E_J^N ; $f_J(\mathbf{r}) = \langle \Psi_0^N | \rho(\mathbf{r}) | \Psi_J^N \rangle$; $\mathcal{E}_J = E_J^N - E_0^N$ corresponds to the excitation energy.

The Fourier transform of χ in frequency domain gives a spectral representation

$$\chi(\mathbf{r}, \mathbf{r}', \omega) = \sum_{J \neq 0} \left[\frac{f_J(\mathbf{r}) f_J^*(\mathbf{r}')}{\omega - \mathcal{E}_J + i\eta} - \frac{f_J^*(\mathbf{r}) f_J(\mathbf{r}')}{\omega + \mathcal{E}_J + i\eta} \right] \quad (2.9)$$

where η is a positive infinitesimal. The two terms represent excitation and de-excitation, respectively, and the poles of χ correspond to the excitation energies.

In order to obtain the independent-particle polarizability χ_0 , we rewrite the density in second quantization framework

$$\rho(\mathbf{r}) = \psi(\mathbf{r}) \psi^\dagger(\mathbf{r}) = \sum_{pq} \phi_p(\mathbf{r}) \phi_q^*(\mathbf{r}) a_p a_q^\dagger \quad (2.10)$$

where $\psi(\mathbf{r})$ and $\psi^\dagger(\mathbf{r})$ are the field operators, and a_p and a_q^\dagger are the annihilation and creation operators, respectively. Then we have

$$f_J(\mathbf{r}) = \sum_{pq} \langle \Psi_0^N | \phi_p(\mathbf{r}) \phi_q^*(\mathbf{r}) a_p a_q^\dagger | \Psi_J^N \rangle = \sum_{ia} \phi_i^*(\mathbf{r}) \phi_a(\mathbf{r}) \quad (2.11)$$

Hence, χ_0 is nonzero only for occupied-virtual pairs. It can be easily built from the ground-state KS orbitals and energies, which is the well-known expression

$$\chi_0^{\text{KS}}(\mathbf{r}, \mathbf{r}', \omega) = \sum_{ia} \left[\frac{\phi_i^*(\mathbf{r}) \phi_a(\mathbf{r}) \phi_a^*(\mathbf{r}') \phi_i(\mathbf{r}')}{\omega - (\varepsilon_a - \varepsilon_i) + i\eta} - \frac{\phi_i(\mathbf{r}) \phi_a^*(\mathbf{r}) \phi_a(\mathbf{r}') \phi_i^*(\mathbf{r}')}{\omega + (\varepsilon_a - \varepsilon_i) + i\eta} \right] \quad (2.12)$$

The full polarizability χ can then be obtained if an expression for f_{XC} is known. The simplest approximation is the random phase approximation (RPA), i.e. set the kernel to zero ($f_{\text{XC}}^{\text{RPA}} = 0$). Another widely used approximation is the adiabatic local density approximation (ALDA), i.e.

the kernel is taken as the adiabatic functional derivative of the static LDA exchange-correlation potential

$$f_{\text{XC}}^{\text{ALDA}}(\mathbf{r}, \mathbf{r}') = \frac{\partial V_{\text{XC}}^{\text{LDA}}(\rho(\mathbf{r}))}{\partial \rho(\mathbf{r})} \delta(\mathbf{r} - \mathbf{r}') \quad (2.13)$$

Matrix representation

The time-dependent KS orbitals are given by

$$\phi_i(\mathbf{r}, t) = \phi_i(\mathbf{r}) e^{-i\varepsilon_i t} \quad (2.14)$$

and the time-dependent perturbed KS orbitals are given by

$$\phi_i^{(1)}(\mathbf{r}, t) = \phi_i^{(1,+)}(\mathbf{r}) e^{-i(\varepsilon_i + \omega)t} + \phi_i^{(1,-)}(\mathbf{r}) e^{-i(\varepsilon_i - \omega)t} \quad (2.15)$$

where both terms can be expanded as linear combinations of virtual orbitals

$$\phi_i^{(1,+)}(\mathbf{r}) = \sum_a X_{ia} \phi_a(\mathbf{r}) \quad (2.16)$$

$$\phi_i^{(1,-)}(\mathbf{r}) = \sum_a Y_{ia}^* \phi_a(\mathbf{r}) \quad (2.17)$$

From Eq.s (2.14) and (2.15), we have the time-dependent induced density expanded over the occupied orbitals as

$$\begin{aligned} \rho^{(1)}(\mathbf{r}, t) &= \sum_i \left[\phi_i^{(1)}(\mathbf{r}, t) \phi_i^*(\mathbf{r}, t) + \phi_i^{(1)*}(\mathbf{r}, t) \phi_i(\mathbf{r}, t) \right] \\ &= \sum_i \left\{ \left[\phi_i^{(1,+)}(\mathbf{r}) \phi_i^*(\mathbf{r}) + \phi_i^{(1,-)*}(\mathbf{r}) \phi_i(\mathbf{r}) \right] e^{-i\omega t} \right. \\ &\quad \left. + \left[\phi_i^{(1,+)*}(\mathbf{r}) \phi_i(\mathbf{r}) + \phi_i^{(1,-)}(\mathbf{r}) \phi_i^*(\mathbf{r}) \right] e^{i\omega t} \right\} \end{aligned} \quad (2.18)$$

And $\rho^{(1)}(\mathbf{r}, t)$ is translated in frequency domain as

$$\rho^{(1)}(\mathbf{r}, t) = \rho^{(1)}(\mathbf{r}, \omega) e^{-i\omega t} + \rho^{(1)}(\mathbf{r}, -\omega) e^{i\omega t} \quad (2.19)$$

Compare Eq. (2.18) with (2.19), we have

$$\begin{aligned} \rho^{(1)}(\mathbf{r}, \omega) &= \sum_i \left[\phi_i^{(1,+)}(\mathbf{r}) \phi_i^*(\mathbf{r}) + \phi_i^{(1,-)*}(\mathbf{r}) \phi_i(\mathbf{r}) \right] \\ &= \sum_{ia} \left[\phi_i^*(\mathbf{r}) \phi_a(\mathbf{r}) X_{ia} + \phi_i(\mathbf{r}) \phi_a^*(\mathbf{r}) Y_{ia} \right] \end{aligned} \quad (2.20)$$

For the purpose of implementation, we now reformulate Eq.s (2.4) and (2.5) in terms of the response of the density matrix P

$$\delta P_{ia} = \sum_{jb} \chi_{ia,jb}^{\text{KS}} \delta V_{jb}^{\text{tot}} \quad (2.21)$$

$$\delta V_{ia}^{\text{tot}} = \delta V_{ia}^{\text{ext}} + \sum_{jb} K_{ia,jb} \delta P_{jb} \quad (2.22)$$

where the kernel K is given by

$$\begin{aligned} K_{ia,jb} &= (ia|v|bj) + (ia|f_{\text{XC}}|bj) \\ &= \iint d\mathbf{r} d\mathbf{r}' \phi_i^*(\mathbf{r}) \phi_a(\mathbf{r}) \left[\frac{1}{|\mathbf{r}-\mathbf{r}'|} + f_{\text{XC}}(\mathbf{r}, \mathbf{r}') \right] \phi_b^*(\mathbf{r}') \phi_j(\mathbf{r}') \end{aligned} \quad (2.23)$$

The two linear equations Eq.s (2.21) and (2.22) are coupled together in terms of P

$$\sum_{jb} \left[(\chi_{ia,jb}^{\text{KS}})^{-1} - K_{ia,jb} \right] \delta P_{jb} = \delta V_{ia}^{\text{ext}} \quad (2.24)$$

We can split δP into the excitation and de-excitation parts, i.e. $\delta P_{jb\tau}$ and $\delta P_{bj\tau}$, and rewrite Eq. (2.24) as two equations

$$\sum_{jb} \left[(\chi_{ia,jb}^{\text{KS}})^{-1} - K_{ia,jb} \right] \delta P_{jb} - \sum_{jb} K_{ia,bj} \delta P_{bj} = \delta V_{ia}^{\text{ext}} \quad (2.25)$$

$$\sum_{jb} \left[(\chi_{ai,bj}^{\text{KS}})^{-1} - K_{ai,bj} \right] \delta P_{bj} - \sum_{jb} K_{ai,jb} \delta P_{jb} = \delta V_{ai}^{\text{ext}} \quad (2.26)$$

which can be expressed in matrix representation as

$$\left[\begin{pmatrix} \mathbf{A} & \mathbf{B} \\ \mathbf{B}^* & \mathbf{A}^* \end{pmatrix} - \omega \begin{pmatrix} \mathbf{1} & \mathbf{0} \\ \mathbf{0} & -\mathbf{1} \end{pmatrix} \right] \begin{pmatrix} \mathbf{X} \\ \mathbf{Y} \end{pmatrix} = \begin{pmatrix} \mathbf{V} \\ \mathbf{V}^* \end{pmatrix} \quad (2.27)$$

In case of free oscillations, $\delta V^{\text{ext}} = 0$, and then we have

$$\begin{pmatrix} \mathbf{A} & \mathbf{B} \\ \mathbf{B}^* & \mathbf{A}^* \end{pmatrix} \begin{pmatrix} \mathbf{X} \\ \mathbf{Y} \end{pmatrix} = \omega \begin{pmatrix} \mathbf{1} & \mathbf{0} \\ \mathbf{0} & -\mathbf{1} \end{pmatrix} \begin{pmatrix} \mathbf{X} \\ \mathbf{Y} \end{pmatrix} \quad (2.28)$$

where the matrix elements are

$$A_{ia,jb} = (\varepsilon_a - \varepsilon_i) \delta_{ij} \delta_{ab} + v_{ia,jb} + f_{ia,jb}^{\text{XC}} \quad (2.29)$$

$$B_{ia,jb} = v_{ia,bj} + f_{ia,bj}^{\text{XC}} \quad (2.30)$$

with $v_{pq,rs} = (pq|sr)$ and $f_{pq,rs}^{\text{XC}} = (pq|f_{\text{XC}}|sr)$. Eq. (2.28) is known as the Casida's equation^[41] in TDDFT. Note that:

- If f_{XC} is replaced by the Hartree–Fock exchange, then it is equal to time-dependent HF (TDHF), also called RPA with exchange (RPAX);
- If f_{XC} is set to zero, then it is equal to direct RPA (dRPA).

For triplets, the orbital-rotation matrix $\mathbf{A} - \mathbf{B}$ has only contributions from f_{XC} and the differences of orbital energies. If one of the eigenvalues approaches zero, then the corresponding triplet excitation energy will also be significantly underestimated. One solution to the triplet problem is the Tamm–Dancoff approximation (TDA)^[47], which assumes $\mathbf{B} = \mathbf{0}$.

2.2 Many-body Green's function

2.2.1 The quasiparticle equations

An alternative scheme for description of the response of strongly interacting particles is to map onto weakly interacting quasiparticles (QPs), i.e. individual electrons plus a surrounding charge cloud of the other electrons, which interact via the screened Coulomb potential rather than the bare Coulomb potential. This scheme provides a better representation of the electrons within the many-body perturbation theory (MBPT) framework, and the quasiparticle energies and wavefunctions can be obtained by solving the Schrödinger-like equation

$$\left[-\frac{1}{2} \nabla^2 + V_{\text{ext}}(\mathbf{r}) + V_{\text{H}}(\mathbf{r}) \right] \phi_i(\mathbf{r}) + \int d\mathbf{r}' \Sigma(\mathbf{r}, \mathbf{r}', \varepsilon_i) \phi_i(\mathbf{r}') = \varepsilon_i \phi_i(\mathbf{r}) \quad (2.31)$$

where Σ is the self-energy that contains all the exchange and correlation effects. The quasiparticle equation (2.31) resembles the Kohn–Sham equation (2.1), replacing the adiabatic, local V_{XC} with the energy-dependent, non-local Σ . It can also be seen as an extension of the Hartree–Fock equation, replacing the bare exchange term with the exchange *and correlation* term.

2.2.2 One-particle Green's function and GW approximation

The one-particle Green's function is defined as

$$iG(1,2) = \langle \Psi_0^N | T \psi(1) \psi^\dagger(2) | \Psi_0^N \rangle = \theta(\tau) \langle \Psi_0^N | \psi(1) \psi^\dagger(2) | \Psi_0^N \rangle - \theta(-\tau) \langle \Psi_0^N | \psi^\dagger(2) \psi(1) | \Psi_0^N \rangle \quad (2.32)$$

where $|\Psi_0^N\rangle$ is the ground state with N electrons and energy E_0^N ; ψ and ψ^\dagger are the field operators, and the indices denote combined space, spin and time coordinates, e.g. $(1) = (\mathbf{r}_1, \sigma_1, t_1) = (\mathbf{x}_1, t_1)$, $\psi(1) = e^{iE_0^N t_1} \psi(\mathbf{x}_1) e^{-iE_0^N t_1}$; T is the Wick's time-ordering operator which orders the operators with later times to the left of earlier times, and $\tau = t_1 - t_2$. For $t_1 > t_2$, $G(1,2)$ describes the probability amplitude for the propagation of an electron from position \mathbf{r}_2 at time t_2 to position \mathbf{r}_1 at time t_1 , or the propagation of a hole in another way around, and vice versa.

By introducing the completeness relation for excited states, Eq. (2.32) becomes

$$\begin{aligned} iG(\mathbf{x}_1, \mathbf{x}_2, \tau) &= \theta(\tau) \sum_A \langle \Psi_0^N | \psi(\mathbf{x}_1) | \Psi_A^{N+1} \rangle \langle \Psi_A^{N+1} | \psi^\dagger(\mathbf{x}_2) | \Psi_0^N \rangle e^{-i(E_A^{N+1} - E_0^N)\tau} \\ &\quad - \theta(-\tau) \sum_I \langle \Psi_0^N | \psi^\dagger(\mathbf{x}_2) | \Psi_I^{N-1} \rangle \langle \Psi_I^{N-1} | \psi(\mathbf{x}_1) | \Psi_0^N \rangle e^{-i(E_0^N - E_I^{N-1})\tau} \\ &= \theta(\tau) \sum_A f_A(\mathbf{x}_1) f_A^*(\mathbf{x}_2) e^{-i\mathcal{E}_A \tau} - \theta(-\tau) \sum_I f_I(\mathbf{x}_1) f_I^*(\mathbf{x}_2) e^{-i\mathcal{E}_I \tau} \end{aligned} \quad (2.33)$$

where $|\Psi_A^{N+1}\rangle$ and $|\Psi_I^{N-1}\rangle$ are the A -th and I -th excited states with $N+1$ and $N-1$ electrons and energies E_A^{N+1} and E_I^{N-1} , respectively; $f_A(\mathbf{x}) = \langle \Psi_0^N | \psi(\mathbf{x}) | \Psi_A^{N+1} \rangle$ and $f_I(\mathbf{x}) = \langle \Psi_0^N | \psi^\dagger(\mathbf{x}) | \Psi_I^{N-1} \rangle$; $\mathcal{E}_A = E_A^{N+1} - E_0^N$ and $\mathcal{E}_I = E_0^N - E_I^{N-1}$ correspond to minus the electron affinities (EAs) and ionization potentials (IPs), which can be measured by direct and inverse photoemission spectroscopies, respectively.

The Fourier transform gives the Lehmann (spectral) representation of Green's function

$$G(\mathbf{x}_1, \mathbf{x}_2, \omega) = \sum_A \frac{f_A(\mathbf{x}_1) f_A^*(\mathbf{x}_2)}{\omega - \mathcal{E}_A + i\eta} + \sum_I \frac{f_I(\mathbf{x}_1) f_I^*(\mathbf{x}_2)}{\omega - \mathcal{E}_I - i\eta} \quad (2.34)$$

The singularities of G are poles lying along the real axis, which are located infinitesimally below the axis for virtual orbitals and above for occupied orbitals. Namely, by switching on the interaction, the poles are shifted along the real axis into the complex plane. Hence, given the exact $G(\mathbf{x}_1, \mathbf{x}_2, \omega)$, the exact EA and IP can be obtained from the poles of G .

The imaginary part of the Green function is called *spectral function*, which is closely related to direct and inverse photoemission spectra

$$A(\mathbf{x}_1, \mathbf{x}_2, \omega) = -\frac{1}{\pi} \text{Im}\{G(\mathbf{x}_1, \mathbf{x}_2, \omega)\} \quad (2.35)$$

For the non-interacting Green's function

$$G_0(\mathbf{x}_1, \mathbf{x}_2, \omega) = \sum_q \frac{\varphi_q(\mathbf{x}_1)\varphi_q^*(\mathbf{x}_2)}{\omega - \varepsilon_q + i\eta \text{sgn}(\varepsilon_q - \varepsilon_F)} \quad (2.36)$$

where ε_F is the Fermi level, which is chosen to lie between the highest occupied and lowest unoccupied orbitals. The spectral function is a δ function located at the eigenvalues of the Hamiltonian of the non-interacting system

$$A_0(\omega) = \delta(\omega - \varepsilon_q) \quad (2.37)$$

For the full Green's function, the spectral function becomes a Lorentzian function

$$A(\omega) \approx \frac{1}{\pi} \frac{\gamma/2}{(\omega - \varepsilon_q - \Delta\omega)^2 + (\gamma/2)^2} \quad (2.38)$$

The position of the peak represents the quasiparticle energy, which is shifted by with respect to the non-interacting case, and its full width at half maximum (FWHM), γ , represents the inverse lifetime of the corresponding quasiparticle.

Dyson's equation

In second quantization framework, the many-body Hamiltonian becomes $H = T + V_{\text{ext}} + V_{\text{H}}$ where

$$T = -\frac{1}{2} \int d\mathbf{r} \psi^\dagger(\mathbf{r}) \nabla^2 \psi(\mathbf{r}) \quad (2.39)$$

$$V_{\text{ext}} = \int d\mathbf{r} \psi^\dagger(\mathbf{r}) V_{\text{ext}}(\mathbf{r}) \psi(\mathbf{r}) \quad (2.40)$$

$$V_{\text{H}} = \frac{1}{2} \int d\mathbf{r} d\mathbf{r}' \psi^\dagger(\mathbf{r}) \psi^\dagger(\mathbf{r}') v(\mathbf{r} - \mathbf{r}') \psi(\mathbf{r}') \psi(\mathbf{r}) \quad (2.41)$$

The Heisenberg equation of motion for the field operator is

$$i \frac{\partial \psi}{\partial t} = [\psi, H] \quad (2.42)$$

from which the equation of motion of the Green's function can be derived as

$$\left[i \frac{\partial}{\partial t_1} - H_0(1) \right] G(1, 2) - \int d3 \Sigma(1, 3) G(3, 2) = \delta(1, 2) \quad (2.43)$$

with

$$H_0(1) = -\frac{1}{2} \nabla_1^2 + V_{\text{ext}}(1) + V_{\text{H}}(1) \quad (2.44)$$

When the self-energy $\Sigma = 0$, we obtain the non-interacting one-particle Green's function G_0

$$\left[i \frac{\partial}{\partial t_1} - H_0(1) \right] G_0(1, 2) = \delta(1, 2) \quad (2.45)$$

The full one-particle Green's function $G(1, 2)$ is linked to $G_0(1, 2)$ via Dyson's equation^[48,49]

$$G(1, 2) = G_0(1, 2) + \int d(34) G_0(1, 3) \Sigma(3, 4) G(4, 2) \quad (2.46)$$

Hedin's equations

Once an expression for the self-energy Σ is known, the energy levels of a molecule or the band structure of a solid can be calculated by determining the eigenvalues of the quasiparticle equation (2.31). The self-energy Σ is calculated via Hedin's equations^[50,51], which are five coupled integral equations (one is Dyson's equation) involving Green's function G_0 , G , the vertex correction function Γ , the *irreducible* polarizability P , and the screened Coulomb interaction W

$$\Sigma(1, 2) = i \int d(34) G(1, 3) \Gamma(3, 4; 2) W(4, 1^+) \quad (2.47)$$

$$G(1, 2) = G_0(1, 2) + \int d(34) G_0(1, 3) \Sigma(3, 4) G(4, 2) \quad (2.48)$$

$$\Gamma(1, 2; 3) = \delta(1, 2) \delta(1, 3) + \int d(4567) \frac{\delta \Sigma(1, 2)}{\delta G(4, 5)} G(4, 6) \Gamma(6, 7; 3) G(7, 5) \quad (2.49)$$

$$P(1, 2) = -i \int d(34) G(1, 3) \Gamma(3, 4; 2) G(4, 1^+) \quad (2.50)$$

$$W(1, 2) = v(1, 2) + \int d(34) v(1, 3) P(3, 4) W(4, 2) \quad (2.51)$$

where $(1^+) = (x_1, t_1 + \eta)$. A diagrammatic representation of the Hedin's equations can be found in Appx. A.1.

Hedin's equations can be solved in an iterative manner. We start with the assumption $\Sigma = 0$, and obtain successively $G = G_0$, $\Gamma = 1$, $P_0 = -iG_0G_0$ (independent-particle polarizability, or RPA polarizability), $W_0 = v + vPW_0$ (RPA screening W_{RPA}), and the updated $\Sigma = iG_0W_0$. In principle, this process should continue until full self-consistency is achieved. In practice, however, calculations usually stop after one round, or shortcut the vertex function Γ to pursue self-consistency for a reduced set of equations. Different schemes for GW approximation will be further discussed in Chap. 2.3.

2.2.3 Response functions

To solve the screening equation (2.51), an inversion via the dielectric function is required, which links the screened Coulomb interaction to the bare one

$$W(1,2) = \int d3 \varepsilon^{-1}(1,3) v(3,2) \quad (2.52)$$

where the dielectric function ε is defined as

$$\varepsilon(1,2) = \delta(1,2) - \int d3 v(1,3) P(3,2) \quad (2.53)$$

Here, P enters W via inversion, which is slightly inconvenient from a numerical point of view. Alternatively, W can be constructed from the *full* (reducible) polarizability χ , which is a central object of TDDFT.

In the language of linear response, χ and P represent the variation of the induced density upon an external potential V_{ext} and a (classical) total potential V_{tot} , respectively

$$\chi(1,2) = -i \frac{\delta G(1,1^+)}{\delta V_{\text{ext}}(2)} \quad (2.54)$$

$$P(1,2) = -i \frac{\delta G(1,1^+)}{\delta [V_{\text{ext}}(2) + V_{\text{H}}(2)]} \quad (2.55)$$

and χ relates to P and ε as

$$\chi(1,2) = P(1,2) + \int d(34) \chi(1,3) v(3,4) P(4,2) \quad (2.56)$$

The inverse dielectric function ε^{-1} can then be written in terms of χ as

$$\varepsilon^{-1}(1,2) = \delta(1,2) + \int d3 v(1,3) \chi(3,2) \quad (2.57)$$

The above relations can be expressed in a simplified way. If we insert $\chi = P + P v \chi$ (Eq. (2.56)) into $\varepsilon^{-1} = 1 + v \chi$ (Eq. (2.57)), then we obtain

$$\begin{aligned} \varepsilon^{-1} &= 1 + v(1 - P v)^{-1} P = 1 + (v^{-1} - P)^{-1} P \\ &= 1 + (1 - v P)^{-1} v P = (1 - v P)^{-1} \end{aligned} \quad (2.58)$$

which is Eq. (2.53).

Inserting Eq. (2.57) into Eq. (2.52), W can be expressed directly in terms of χ as

$$W(1,2) = v(1,2) + \int d(34) v(1,3) \chi(3,4) v(4,2) \quad (2.59)$$

or in terms of P as (using Eq. (2.56))

$$W = v + vPv + vPvPv + \dots \quad (2.60)$$

Matrix representation

Applying the resolution-of-the-identity (RI) approximation, the two-electron, four-center integrals are computed via three-center integrals

$$(pq|rs) \cong \sum_{PQ} (pq|P)(\mathbf{V}^{-1})_{PQ}(Q|rs) \quad (2.61)$$

where $V_{PQ} = (P|Q)$, and P, Q are the auxiliary basis sets. Since the matrix \mathbf{V} is real-valued, symmetric, and positive-definite, a Cholesky decomposition $\mathbf{V} = \mathbf{L}\mathbf{L}^T$ can be done, and we define the three-index intermediate

$$R_{P,rs} = \sum_Q (\mathbf{L}^{-1})_{PQ}(Q|rs) \quad (2.62)$$

The Coulomb and screened integrals can then be approximated as

$$v_{pq,rs} \cong \sum_P R_{pq,P} R_{P,rs} \quad (2.63)$$

$$W_{pq,rs} \cong \sum_{PQ} R_{pq,P} \epsilon_{PQ}^{-1} R_{Q,rs} \quad (2.64)$$

The inverse dielectric function is

$$\epsilon_{PQ}^{-1} = [\delta_{PQ} - \Pi_{PQ}(\omega)]^{-1} \quad (2.65)$$

where $\mathbf{\Pi}$ is the matrix representation of the density response function

$$\Pi_{PQ}(\omega) = \sum_{kc} \left[\frac{R_{kc,P} R_{Q,kc}}{\omega - (\epsilon_c - \epsilon_k)} - \frac{R_{ck,P} R_{Q,ck}}{\omega + (\epsilon_c - \epsilon_k)} \right] \quad (2.66)$$

If Kramers symmetry is obeyed, then Eq.(2.66) becomes

$$\Pi_{PQ}(\omega) = 2 \sum_{kc} \left[\frac{(\epsilon_c - \epsilon_k) R_{kc,P} R_{Q,kc}}{\omega^2 - (\epsilon_c - \epsilon_k)^2} \right] \quad (2.67)$$

Therefore, the matrix $\mathbf{\Pi}(\omega)$ is real-valued and symmetric.

We can rewrite the RI approximation in matrix notation for both Coulomb interaction and screened exchange

$$\mathbf{v} \cong \mathbf{R}^T \mathbf{R}, \mathbf{W} \cong \mathbf{R}^T \boldsymbol{\epsilon}^{-1} \mathbf{R} \quad (2.68)$$

Similarly, we expand the inverse dielectric function to calculate W

$$\boldsymbol{\epsilon} = \mathbf{1} - \mathbf{X}, \mathbf{X} = 2\mathbf{R}\mathbf{D}^{-1}\mathbf{R}^T \quad (2.69)$$

Therefore, we have

$$\mathbf{W} \cong \mathbf{R}^T \mathbf{R} + \mathbf{R}^T \mathbf{X} \mathbf{R} + \mathbf{R}^T \mathbf{X} \mathbf{R} \mathbf{R}^T \mathbf{X} \mathbf{R} + \dots \quad (2.70)$$

Although good results have been obtained with GW approximation for description of charged excitations, e.g. quasiparticle energy levels and photoemission spectra, it fails to properly describe neutral excitations, e.g. absorption spectra due to the definition of the polarizability P , where the interaction between the electron (described by $G(1,2)$) and the hole (described by $G(2,1^+)$) is missing. The inclusion of the vertex function $\Gamma(1,2,3)$ in the screening equation is then crucial for accurate description of two-particle excitations. This has been achieved by the Bethe–Salpeter equation (BSE).

2.2.4 Two-particle Green's function and Bethe–Salpeter equation

The two-particle Green's function is defined as

$$i^2 G(1,2;3,4) = \langle \Psi_0^N | T \psi(1) \psi(2) \psi^\dagger(4) \psi^\dagger(3) | \Psi_0^N \rangle \quad (2.71)$$

It can describe the propagation of different coupled pairs depending on the ordering of the four times. Here we are only interested in the neutral excitation, where an electron-hole is created.

The independent-particle polarizability L_0 describes the propagation of an electron and a hole separately

$$L_0(1,2;3,4) = -iG(1,4)G(2,3) \quad (2.72)$$

And the four-point polarizability L describes the propagation of two coupled particles minus that of the two independent ones

$$L(1,2;3,4) = iG(1,2;3,4) - iG(1,3)G(2,4) \quad (2.73)$$

The polarizability L is also linked to L_0 via a Dyson-like equation, which is known as the Bethe–Salpeter equation^[52]

$$L(1, 2; 3, 4) = L_0(1, 2; 3, 4) + \int d(5678)L_0(1, 6; 3, 5)K(5, 8; 6, 7)L(7, 2; 8, 4) \quad (2.74)$$

where the kernel K is

$$K(5, 6; 7, 8) = \delta(5, 6)\delta(7, 8)v(5, 7) + \Xi(5, 8; 6, 7) \quad (2.75)$$

with Ξ defined as

$$\Xi(5, 8; 6, 7) = i \frac{\delta\Sigma(5, 6)}{\delta G(7, 8)} \quad (2.76)$$

or in a simplified way

$$L = L_0 + L_0(v + \Xi)L \quad (2.77)$$

The Bethe–Salpeter equation (2.77) resembles the TDDFT equation (2.6), replacing the two-point exchange-correlation kernel f_{xc} ($\partial V_{xc}/\partial\rho$) by the four-point Bethe–Salpeter Hartree-exchange-correlation kernel Ξ ($\partial\Sigma/\partial G$). The presence of Ξ indicates the intrinsic two-particle character of the BSE.

Taking the GW approximation for Σ

$$\Xi = i \frac{\delta\Sigma}{\delta G} = \frac{-\delta(GW)}{\delta G} = -W - G \frac{\delta(W)}{\delta G} \approx -W \quad (2.78)$$

directly leads to

$$K(5, 6, 7, 8) = \delta(5, 6)\delta(7, 8)v(5, 7) - \delta(5, 7)\delta(6, 8)W(5, 6) \quad (2.79)$$

The standard implementation of the BSE formalism assumes an adiabatic approximation for W

$$W(1, 2) = W(\mathbf{r}_1, \mathbf{r}_2)\delta(t_1 - t_2) \quad (2.80)$$

which resembles the adiabatic approximation for f_{xc} in Eq. (2.13). Such a treatment leads to a formulation similar to the Casida's equation (2.28) for TDDFT or TDHF

$$\begin{pmatrix} \mathbf{A} & \mathbf{B} \\ \mathbf{B}^* & \mathbf{A}^* \end{pmatrix} \begin{pmatrix} \mathbf{X}_n \\ \mathbf{Y}_n \end{pmatrix} = \omega_n \begin{pmatrix} \mathbf{1} & \mathbf{0} \\ \mathbf{0} & -\mathbf{1} \end{pmatrix} \begin{pmatrix} \mathbf{X}_n \\ \mathbf{Y}_n \end{pmatrix} \quad (2.81)$$

where the matrix elements are

$$A_{ia,jb}^{\text{BSE}} = (\varepsilon_a^{\text{QP}} - \varepsilon_i^{\text{QP}}) \delta_{ij} \delta_{ab} + v_{ia,jb} - W_{ij,ab}^{\text{QP}} \quad (2.82)$$

$$B_{ia,jb}^{\text{BSE}} = v_{ia,bj} - W_{ib,aj}^{\text{QP}} \quad (2.83)$$

The only differences between BSE and TDDFT/TDHF are:

- The *quasiparticle energies* $\varepsilon_p^{\text{QP}}$ replace the Kohn–Sham or Hartree–Fock orbital energies;
- The *screened exchange* W replaces the Kohn–Sham exchange–correlation kernel or Hartree–Fock exchange interaction.

In addition, to improve the triplet excitation energies in BSE, a hybrid BSE/TDDFT ansatz, i.e. correlation-kernel-augmented BSE (cBSE)^[4], is constructed *ad hoc* as

$$A_{ia,jb}^{\text{cBSE}} = (\varepsilon_a^{\text{QP}} - \varepsilon_i^{\text{QP}}) \delta_{ij} \delta_{ab} + v_{ia,jb} + f_{ia,jb}^{\text{C}} - W_{ij,ab}^{\text{KS}} \quad (2.84)$$

$$B_{ia,jb}^{\text{cBSE}} = v_{ia,bj} + f_{ia,bj}^{\text{C}} - W_{ib,aj}^{\text{KS}} \quad (2.85)$$

which keeps the correlation part of the underlying density functional, and constructs the screened exchange with Kohn–Sham orbital energies. In this manner, the correct description of charge-transfer excitations is still retained.

2.3 Calculation of quasiparticle energies in GW

2.3.1 Separation of self-energy

Analogous to Eq. (2.20), the transition density for the m -th excited state is

$$\rho_m(\mathbf{x}) = \sum_{kc} [\phi_k^*(\mathbf{x}) \phi_c(\mathbf{x}) X_{kc}^m + \phi_k(\mathbf{x}) \phi_c^*(\mathbf{x}) Y_{kc}^m] \quad (2.86)$$

and analogous to Eq. (2.9), the polarizability χ is

$$\chi(\mathbf{x}, \mathbf{x}', \omega) = \sum_{m \neq 0} \left[\frac{\rho_m(\mathbf{x}) \rho_m^*(\mathbf{x}')}{\omega - \omega_m + i\eta} - \frac{\rho_m^*(\mathbf{x}) \rho_m(\mathbf{x}')}{\omega + \omega_m + i\eta} \right] \quad (2.87)$$

where ω_m is the excitation energy.

Then from Eq. (2.59), the screened exchange W is

$$W(\mathbf{x}, \mathbf{x}', \omega) = v(\mathbf{x} - \mathbf{x}') + \sum_{m \neq 0} \left[\frac{V_m(\mathbf{x}) V_m^*(\mathbf{x}')}{\omega - \omega_m + i\eta} - \frac{V_m^*(\mathbf{x}) V_m(\mathbf{x}')}{\omega + \omega_m + i\eta} \right] \quad (2.88)$$

where $V_m(\mathbf{x}) = \int d\mathbf{x}' v(\mathbf{x} - \mathbf{x}') \rho_m(\mathbf{x}')$.

According to the relation $\Sigma = iGW$

$$\Sigma(\mathbf{x}, \mathbf{x}', \omega) = \frac{i}{2\pi} \int d\omega' e^{i\eta\omega'} G(\mathbf{x}, \mathbf{x}', \omega + \omega') W(\mathbf{x}, \mathbf{x}', \omega') \quad (2.89)$$

the self-energy Σ can thus be separated into a frequency-independent exchange part Σ^X and a frequency-dependent correlation part Σ^C

$$\Sigma(\mathbf{x}, \mathbf{x}', \omega) = \Sigma^X(\mathbf{x}, \mathbf{x}') + \Sigma^C(\mathbf{x}, \mathbf{x}', \omega) \quad (2.90)$$

where Σ^X is nothing but Hartree–Fock exchange

$$\Sigma^X(\mathbf{x}, \mathbf{x}') = V^X(\mathbf{x}, \mathbf{x}') \quad (2.91)$$

$$\langle p | \Sigma^X | p \rangle = - \sum_k \langle pk | kp \rangle = - \langle p | K | p \rangle \quad (2.92)$$

and Σ^C reads

$$\Sigma^C(\mathbf{x}, \mathbf{x}', \omega) = \sum_{m \neq 0} \left[\sum_k \frac{V_m(\mathbf{x}) V_m^*(\mathbf{x}') \varphi_k(\mathbf{x}) \varphi_k^*(\mathbf{x}')}{\omega - \omega_m + 2i\eta} - \sum_c \frac{V_m^*(\mathbf{x}) V_m(\mathbf{x}') \varphi_c(\mathbf{x}) \varphi_c^*(\mathbf{x}')}{\omega + \omega_m + 2i\eta} \right] \quad (2.93)$$

Compare the quasiparticle equation (2.31) with the Kohn–Sham equation (2.1), the quasiparticle energies can be obtained in an iterative manner

$$\varepsilon_p^{(n+1)} = \varepsilon_p^{(0)} + \left\langle p \left| \Sigma^X + \Sigma^C \left(\varepsilon_p^{(n)} \right) - V_{XC} \right| p \right\rangle \quad (2.94)$$

where $\varepsilon_p^{(0)}$ is the Kohn–Sham orbital energy

$$\varepsilon_p^{(0)} = \langle p | h + J + V_{XC} | p \rangle \quad (2.95)$$

Then we have

$$\varepsilon_p^{(n+1)} = \left\langle p \left| h + J - K + \Sigma^C \left(\varepsilon_p^{(n)} \right) \right| p \right\rangle \quad (2.96)$$

2.3.2 GW variants with different levels of self-consistency

Non-self-consistent: (linearized) G_0W_0

In the G_0W_0 method, the QP energies are obtained after one simple iteration

$$\varepsilon_p^{(1)} = \left\langle p \left| h + J - K + \Sigma^C \left(\varepsilon_p^{(0)} \right) \right| p \right\rangle \quad (2.97)$$

In the *linearized* G_0W_0 method^[26], the QP energies are obtained after one *Newton's iteration*, i.e. as a first-order Taylor expansion around the KS solution

$$\begin{aligned} \varepsilon_p^{(1)} = & \left\langle p \left| h + J - K + \Sigma^C \left(\varepsilon_p^{(0)} \right) \right| p \right\rangle \\ & + \left\langle p \left| \frac{\partial \Sigma^C}{\partial \varepsilon} \left(\varepsilon_p^{(0)} \right) \right| p \right\rangle \left(\varepsilon_p^{(1)} - \varepsilon_p^{(0)} \right) \end{aligned} \quad (2.98)$$

Partially self-consistent: evGW and qsGW

In the eigenvalue-only self-consistent GW (evGW) method^[30], Eq. (2.96) is iterated until self-consistency is achieved. The QP energy reads

$$\varepsilon_p^{(n+1)} = h_{pp} + J_{pp} - K_{pp} + \left\langle p \left| \Sigma^C \left(\varepsilon_p^{(n)} \right) \right| p \right\rangle \quad (2.99)$$

Note that only the QP energies are updated while the KS orbitals remain unchanged.

In the quasiparticle self-consistent GW (qsGW) method^[31,53], not only the diagonal matrix elements $\langle p | \Sigma^C(\varepsilon_p) | p \rangle$, but also the off-diagonal matrix elements $\langle p | \Sigma^C(\varepsilon_s) | q \rangle$ are required, with $s = \{p, q\}$. The Fock matrix then reads

$$F_{pq}^{(n+1)} = h_{pq}^{(n)} + J_{pq}^{(n)} - K_{pq}^{(n)} + \frac{1}{2} \left\langle p^{(n)} \left| \Sigma^C \left(\varepsilon_p^{(n)} \right) + \Sigma^C \left(\varepsilon_q^{(n)} \right) \right| q^{(n)} \right\rangle \quad (2.100)$$

The Fock matrix is diagonalized to generate new QP vectors and energies, from which the new Fock matrix will be constructed. This is iterated until self-consistency is achieved, and both the QP orbitals and energies are updated.

2.3.3 GW variants for evaluation of correlation self-energy

Spectral representation (SR-GW)

Formally, the quasiparticle energies are computed for *all* orbital levels using the full spectral representation of the density response function. In this way, the correlation self-energy can be integrated analytically and no quadrature is involved, hence it yields the exact result and serves

as a benchmark for the low-scaling schemes. However, it is computationally very expensive and scales as N^6 with system size N .

The matrix elements of the correlation self-energy (Eq. (2.93)) are

$$\begin{aligned} \langle p | \Sigma^C(\varepsilon_s) | q \rangle = \sum_{m \neq 0} \left[\sum_k (kp | \rho_m)(kq | \rho_m) D_{k,s,m}^+ \right. \\ \left. + \sum_c (cp | \rho_m)(cq | \rho_m) D_{c,s,m}^- \right] \end{aligned} \quad (2.101)$$

where

$$D_{r,s,m}^\pm = \frac{\varepsilon_s - \varepsilon_r \pm \omega_m}{(\varepsilon_s - \varepsilon_r \pm \omega_m)^2 + \eta^2} \quad (2.102)$$

The required integrals $(pq | \rho_m)$ can be evaluated via an intermediate γ_m that contracts the excitation vectors into the subspace of the auxiliary basis sets

$$\gamma_{p,m} = \sum_{kc} [R_{P,kc} X_{kc}^m + R_{P,kc}^* Y_{kc}^m] \quad (2.103)$$

Then we have

$$(pq | \rho_m) = \sum_{kc} [(pq | kc) X_{kc}^m + (pq | ck) Y_{kc}^m] = \sum_P R_{pq,P} \gamma_{P,m} \quad (2.104)$$

The excitation vectors are computed with the dRPA approximation, using KS orbital energies in the case of G_0W_0 , and QP energies in the case of evGW and qsGW.

Analytic continuation (AC-GW)

The Green's function has a smooth form on the imaginary axis, whereas it usually exhibits many poles in the real frequency domain. Therefore, it is advantageous to first calculate the self-energy for imaginary frequencies, which can be efficiently computed using RI approximation, and then evaluate the self-energy for real frequencies via analytic continuation^[34].

Inserting Eqs. (2.36), (2.64) and (2.65) into Eq. (2.89), and we obtain

$$\begin{aligned} \Sigma_p(\mathbf{x}, \mathbf{x}', \omega) = \frac{i}{2\pi} \sum_q \int d\omega' \frac{1}{\omega + \omega' - \varepsilon_q + i\eta \operatorname{sgn}(\varepsilon_q - \varepsilon_F)} \\ \times \sum_{PQ} R_{pq,P} [1 - \Pi(\omega')]_{PQ}^{-1} R_{Q,qp} \end{aligned} \quad (2.105)$$

and the correlation part Σ^C is

$$\begin{aligned} \Sigma_p^C(\mathbf{x}, \mathbf{x}', \omega) = \frac{i}{2\pi} \sum_q \int d\omega' \frac{1}{\omega + \omega' - \varepsilon_q + i\eta \operatorname{sgn}(\varepsilon_q - \varepsilon_F)} \\ \times \sum_{PQ} R_{pq,P} \left\{ [1 - \Pi(\omega')]_{PQ}^{-1} - \delta_{PQ} \right\} R_{Q,qp} \end{aligned} \quad (2.106)$$

Likewise, for imaginary frequencies, we have

$$\begin{aligned} \Sigma_p^C(\mathbf{x}, \mathbf{x}', i\omega) = & -\frac{1}{2\pi} \sum_q \int d\omega' \frac{1}{i\omega + i\omega' - \varepsilon_q + i\eta \operatorname{sgn}(\varepsilon_q - \varepsilon_F)} \\ & \times \sum_{PQ} R_{pq,P} \left\{ [1 - \Pi(i\omega')]_{PQ}^{-1} - \delta_{PQ} \right\} R_{Q,qp} \end{aligned} \quad (2.107)$$

And similar to Eq. (2.67), for imaginary frequencies, we have

$$\Pi_{PQ}(i\omega) = -2 \sum_{kc} \left[\frac{(\varepsilon_c - \varepsilon_k) R_{kc,P} R_{Q,kc}}{\omega^2 + (\varepsilon_c - \varepsilon_k)^2} \right] \quad (2.108)$$

Since the matrix $\mathbf{1} - \Pi(i\omega)$ is positive-definite, Eq. (2.107) can be efficiently computed via a Cholesky decomposition $\mathbf{1} - \Pi(i\omega') = \mathbf{L}\mathbf{L}^T$

$$[1 - \Pi(i\omega')]_{PQ}^{-1} = \sum_R (L_{PR}^{-1})^T L_{RQ}^{-1} \quad (2.109)$$

$$\sum_{PQ} R_{pq,P} [1 - \Pi(i\omega')]_{PQ}^{-1} R_{Q,qp} = \sum_R \tilde{R}_{pq,R} \tilde{R}_{R,qp} \quad (2.110)$$

where

$$\tilde{R}_{R,qp} = \sum_Q L_{RQ}^{-1} R_{Q,qp} \quad (2.111)$$

For the grid points ω and ω' on the imaginary axis, $\Sigma_p^C(i\omega)$ is fit to an n -point Padé approximant

$$\Sigma_p^C(i\omega) \cong P_p(i\omega) = \frac{\sum_{j=0}^{n-1} a_j (i\omega)^j}{1 + \sum_{k=1}^n b_k (i\omega)^k} \quad (2.112)$$

In Eq. (2.112), replacing $i\omega$ with ω in P , Σ^C for real frequencies can then be obtained by means of analytic continuation.

In AC-GW, quasiparticle energies are calculated for HOMO and LUMO only, and the rest of the orbitals are shifted according to the new HOMO and LUMO while preserving the Kohn-Sham energy spacing. It has been demonstrated that the AC-GW variant is often not accurate enough when computing the self-energy for nonvalence states.^[36]

Contour deformation (CD-GW)

An alternative method is to calculate the self-energy directly on the real-frequency axis via the contour deformation technique^[36], thus avoiding the fitting procedure in analytic continuation. A contour is deformed into the complex plane such that the numerically unstable integration

at the poles is circumvented (see Figure 2.1), and $\Sigma^C(\omega)$ is transformed as a contour integral, $R^C(\omega)$, minus the integral along the imaginary axis, $I^C(\omega)$

$$\begin{aligned}\Sigma^C(\mathbf{x}, \mathbf{x}', \omega) &= R^C(\omega) - I^C(\omega) \\ &= \frac{i}{2\pi} \oint d\omega' e^{i\eta\omega'} G(\mathbf{x}, \mathbf{x}', \omega + \omega') W^C(\mathbf{x}, \mathbf{x}', \omega') \\ &\quad - \frac{1}{2\pi} \int d\omega' e^{i\eta\omega'} G(\mathbf{x}, \mathbf{x}', \omega + i\omega') W^C(\mathbf{x}, \mathbf{x}', i\omega')\end{aligned}\quad (2.113)$$

where the correlation part of the screened exchange is

$$W^C(\mathbf{x}, \mathbf{x}', i\omega) = W(\mathbf{x}, \mathbf{x}', i\omega) - v(\mathbf{x}, \mathbf{x}') \quad (2.114)$$

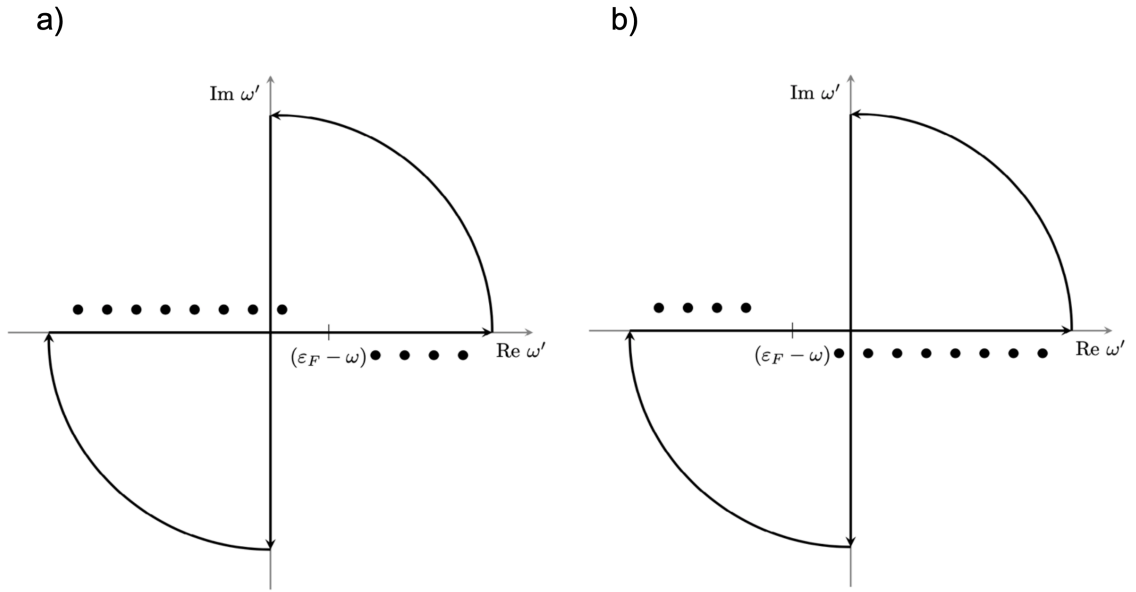


Figure 2.1: Contours used to evaluate $\Sigma(\omega)$ and circles representing poles of G . When seeking the quasiparticle energy for occupied states (a) or virtual states (b), the poles start entering the first quadrant (a) or the third quadrant (b), respectively.

The poles of G are located in the complex frequency domain

$$\omega' = \varepsilon_q - \omega - i\eta \operatorname{sgn}(\varepsilon_q - \varepsilon_F) \quad (2.115)$$

The contour integral $R^C(\omega)$ can be computed from the residues of the poles that are enclosed in the contour, i.e. in the first or third quadrants, which holds only for $\omega < \varepsilon_q < \varepsilon_F$ (Figure 2.1a) and $\omega > \varepsilon_q > \varepsilon_F$ (Figure 2.1b). When the poles lie *on* the contour (imaginary axis), i.e. $\omega = \varepsilon_q$,

they are considered as half of the respective residue^[54]. Employing the residue theorem, $R^C(\omega)$ is obtained as

$$R_p^C(\omega) = \sum_q f_q W_{pq}^C(|\varepsilon_q - \omega| + i\eta) \quad (2.116)$$

with

$$W_{pq}^C(|\varepsilon_q - \omega| + i\eta) = \sum_{PQ} R_{pq,P} \left\{ [1 - \Pi(|\varepsilon_q - \omega| + i\eta)]_{PQ}^{-1} - \delta_{PQ} \right\} R_{Q,qp} \quad (2.117)$$

and f_q as the contribution of the residue

$$f_q = \begin{cases} +1 & \text{if } \omega > \varepsilon_q > \varepsilon_F \\ +0.5 & \text{if } \omega = \varepsilon_q > \varepsilon_F \\ -0.5 & \text{if } \omega = \varepsilon_q < \varepsilon_F \\ -1 & \text{if } \omega < \varepsilon_q < \varepsilon_F \\ 0 & \text{else} \end{cases} \quad (2.118)$$

And the integral along the imaginary axis $I^C(\omega)$ can be obtained analogously to Eq. (2.107)

$$I_p^C(\omega) = -\frac{1}{2\pi} \sum_q \int d\omega' \frac{W_{pq}^C(i\omega')}{\omega + i\omega' - \varepsilon_q + i\eta \operatorname{sgn}(\varepsilon_q - \varepsilon_F)} \quad (2.119)$$

with

$$W_{pq}^C(i\omega) = \sum_{PQ} R_{pq,P} \left\{ [1 - \Pi(i\omega)]_{PQ}^{-1} - \delta_{PQ} \right\} R_{Q,qp} \quad (2.120)$$

In CD-GW, if quasiparticle energies are calculated for HOMO and LUMO only, then it is equivalent to AC-GW. Theoretically, when more orbitals are included in the calculation, the resulting excitation energies will be more accurate, and also the computation will be more demanding.

2.4 Computational details

All quantum-chemical calculations in this thesis were performed with the TURBOMOLE program package.^[55,56] The resolution-of-the-identity (RI) approximation was used for all two-electron integrals. The effective core potentials (ECPs)^[57] were used for second and third row transition elements (namely Ag and Au) to speed up the computation and more importantly, to account for the relativistic effects in both one-component (1c, scalar-relativistic) and two-component (2c, including spin-orbit coupling) frameworks. For non- and scalar-relativistic 1c

calculations, the def2-XVP basis sets^[58] together with the underlying def2-ecp ECPs were used. For quasirelativistic 2c calculations, the dhf-XVP-2c basis sets^[59] together with the underlying dhf-ecp-2c ECPs^[60] were used.

All orbital and auxiliary basis sets were taken from the TURBOMOLE basis-set library.^[56] The "Coulomb-fitting" auxiliary basis sets (denoted jbas) were used in the ground-state HF and DFT computations, and the "MP2-fitting" auxiliary basis sets (denoted cbas) were used in the excited-state TDDFT and GW/BSE computations. The ground-state Hartree–Fock (HF) and density functional theory (DFT) computations were carried out with the modules DSCF and RIDFT, and the self-consistent field convergence criterion `scf conv = 8` and DFT grid (m)4 were used. The geometry optimization was considered converged when the change in energy and cartesian gradients reached thresholds of 10^{-7} and 10^{-4} Hartree, respectively. The excited-state TDDFT and GW/BSE computations were carried out with the ESCF module, and the convergence criterion `rpaconv = 6` was used. Furthermore, in evGW and qsGW, the damping parameter was set to $\eta = 0.001$ in order to achieve rapid convergence. In AC-GW and CD-GW, 128 grid points were used, also 128 parameters were taken in the Padé approximant.

All the plots in this thesis were generated with Gnuplot^[61] and VMD^[62].

3 Performance assessment of BSE with different GW starting points

In this chapter, an extensive accuracy assessment of SR-GW/(c)BSE is presented for singlet and triplet valence excited states, as well as charge-transfer excited states. Furthermore, a computed electronic circular dichroism (ECD) spectrum of fullerene is displayed as a real-world example, and the timings measured for a few GW and BSE computations are also reported.

3.1 Valence excited states

The well-known benchmark set established by Thiel and co-workers^[63–65] consists of 28 small and medium-sized organic molecules. Excluding excited states with strong double-excited and Rydberg character, 93 singlet and 63 triplet valence excited states left in the benchmark were analyzed. Theoretical estimates at the level of approximate coupled-cluster singles, doubles and triples (CC3) calculations with aug-cc-pVTZ basis set were adopted as reference values for the vertical excitation energies. The estimates were based on an extensive literature study^[63–67] as well as *ab initio* computations of our own, and more details can be found in Ref. 5.

The deviations of singlet and triplet excitation energies computed in def2-TZVP basis set with respect to the CC3/aug-cc-pVTZ reference values are plotted in Figure 3.1, and the statistical analyses of singlets and triplets are listed in Tables 3.1 and 3.2, respectively. The PBE0 functional^[68,69] was used in the TDDFT, G_0W_0 /(c)BSE and evGW/(c)BSE calculations. As can be seen, the G_0W_0 -BSE energies are too low on average, and hence it is not recommended in combination with the presented PBE0 starting point. The TDDFT, evGW/BSE and qsGW/BSE methods show similar performance and achieve good accuracy in the case of singlet states. However, they systematically underestimate the triplet excitation energies. This underestimation of the triplet energies by the evGW/BSE model has also been addressed earlier in Ref. 70, where the authors suggested that fully self-consistent GW might improve the results. However, as shown in the present work, although the dependence on the reference orbitals is removed by the qsGW/BSE model, it hardly yields any improvement in comparison to the evGW/BSE model, and the triplet excitation energies are still much too low in the qsGW/BSE model. By adding the correlation kernel of the underlying density functional, the triplets are significantly

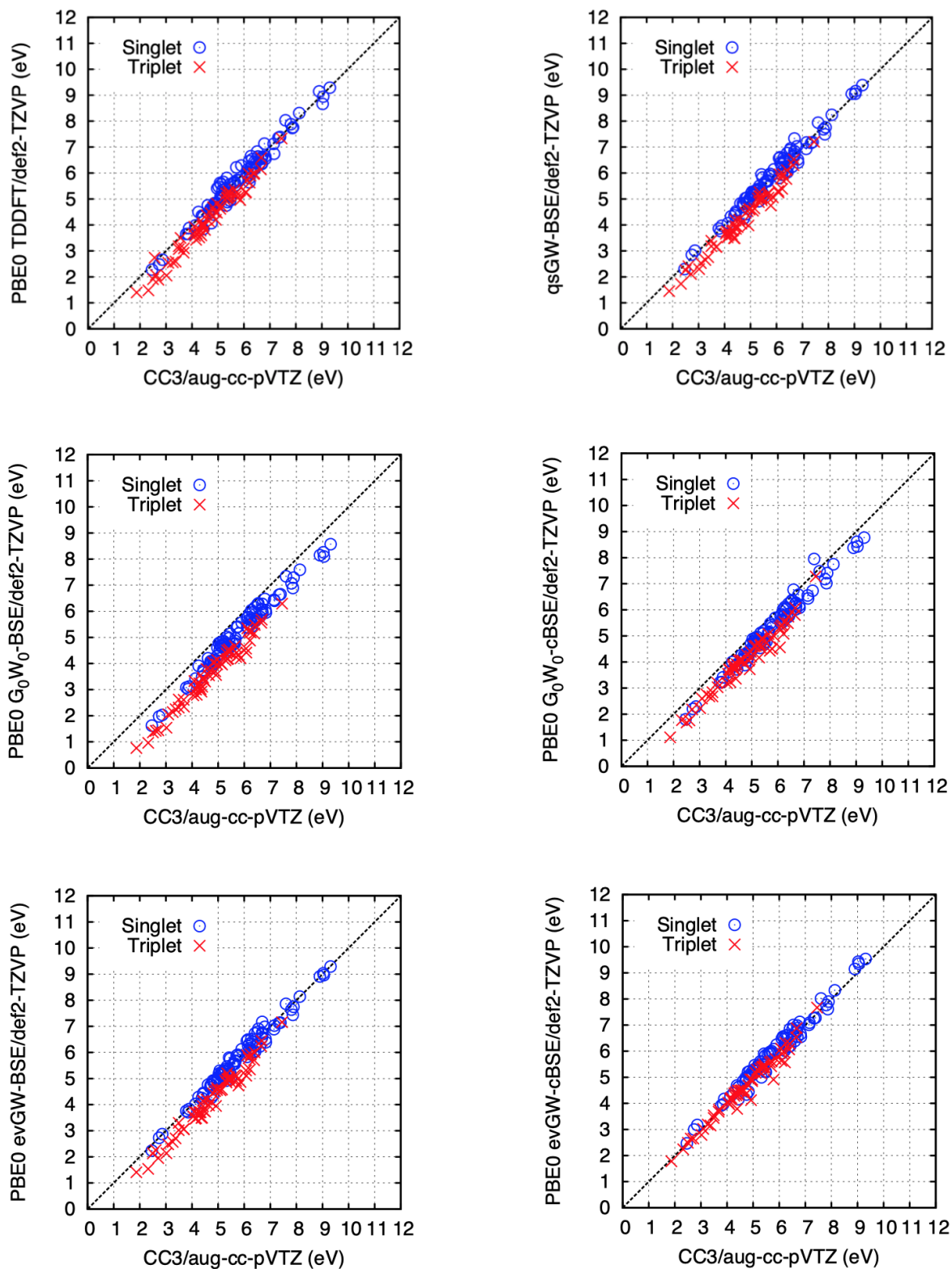


Figure 3.1: Plot of the computed singlet and triplet excitation energies against the reference CC3/aug-cc-pVTZ values.

Table 3.1: Deviations of singlet excitation energies (eV) obtained in the def2-TZVP basis with respect to the CC3/aug-cc-pVTZ reference.

	TDDFT	G_0W_0		evGW		qsGW
		BSE	cBSE	BSE	cBSE	BSE
MSD ^a	-0.06	-0.63	-0.46	-0.02	0.14	0.03
MAD ^b	0.21	0.63	0.48	0.16	0.23	0.18
RMS ^c	0.27	0.66	0.51	0.21	0.26	0.23
MAX ^d	0.68	0.97	0.87	0.48	0.48	0.64
MED ^e	0.15	0.70	0.51	0.12	0.24	0.14

^aMean signed deviation. ^bMean absolute deviation. ^cRoot-mean-square deviation.

^dMaximum absolute deviation. ^eMedian absolute deviation.

Table 3.2: Deviations of triplet excitation energies (eV) obtained in the def2-TZVP basis with respect to the CC3/aug-cc-pVTZ reference.

	TDDFT	G_0W_0		evGW		qsGW
		BSE	cBSE	BSE	cBSE	BSE
MSD	-0.48	-1.14	-0.70	-0.56	-0.09	-0.49
MAD	0.48	1.14	0.70	0.56	0.14	0.49
RMS	0.53	1.16	0.74	0.60	0.23	0.53
MAX	0.97	1.66	1.52	1.05	0.87	1.03
MED	0.47	1.12	0.65	0.54	0.07	0.48

improved in cBSE compared to the BSE counterparts (Table 3.2), without the singlets being obviously deteriorated (Table 3.1). In particular, the evGW/cBSE model provides an accurate and balanced description for both singlet and triplet excited state, and the overall performance is in good agreement with the CC3 reference.

Additional aug-cc-pVTZ calculations have been performed for TDDFT, evGW/(c)BSE and qsGW/BSE methods to investigate their basis set dependence. The statistical analyses with respect to the CC3/aug-cc-pVTZ reference data are given in Tables 3.3 and 3.4, while Tables 3.5 and 3.6 provide mutual comparisons between the def2-TZVP and aug-cc-pVTZ basis sets. As can be seen in Tables 3.5 and 3.6, for TDDFT and qsGW/BSE, the extension of the basis set with diffuse functions only leads to slight lowering in the excitation energies, and the def2-TZVP and aug-cc-pVTZ results are in perfect agreement. For these two methods, considering that

Table 3.3: Deviations of singlet excitation energies (eV) obtained in the aug-cc-pVTZ basis with respect to the CC3/aug-cc-pVTZ reference.

	TDDFT	evGW		qsGW
		BSE	cBSE	BSE
MSD	-0.13	-0.24	-0.09	-0.04
MAD	0.23	0.26	0.20	0.17
RMS	0.28	0.34	0.26	0.23
MAX	0.71	1.10	0.76	0.56
MED	0.17	0.18	0.19	0.12

Table 3.4: Deviations of triplet excitation energies (eV) obtained in the aug-cc-pVTZ basis with respect to the CC3/aug-cc-pVTZ reference.

	TDDFT	evGW		qsGW
		BSE	cBSE	BSE
MSD	-0.50	-0.84	-0.35	-0.52
MAD	0.50	0.84	0.35	0.52
RMS	0.54	0.90	0.46	0.55
MAX	0.96	1.97	1.48	1.07
MED	0.49	0.84	0.27	0.52

the computation is more expensive and that the assignment of the states is more difficult in the presence of diffuse functions, while the improvement of the excitation energies is rather minor, the smaller def2-TZVP basis set is adequate for the valence excited states of the Thiel’s test set studied in the present work. The basis set dependence is, however, much more pronounced for the evGW model. Compared to the other two methods, the lowering in both evGW/BSE and cBSE excitation energies due to the diffuse functions is twice as large for singlet states, and even an order of magnitude larger for triplet states. Though the singlet excitation energies of evGW/cBSE are still in very good agreement with the CC3 reference results (Table 3.3), and the triplet excitation energies are also greatly improved in comparison to evGW/BSE (Table 3.4). This ill-behavior caused by the presence of diffuse functions is an insufficiency of the underlying GW method,^[4,5] which vastly underestimates the lowest unoccupied molecular orbital (LUMO) in some cases, especially for acetamide and propanamide. Since (c)BSE rely on good

Table 3.5: Deviations of singlet excitation energies (eV) obtained in the aug-cc-pVTZ basis with respect to the def2-TZVP results.

	TDDFT	evGW		qsGW
		BSE	cBSE	BSE
MSD	-0.07	-0.22	-0.23	-0.08
MAD	0.08	0.22	0.23	0.08
RMS	0.12	0.29	0.30	0.11
MAX	0.53	1.02	1.08	0.46
MED	0.04	0.15	0.16	0.06

Table 3.6: Deviations of triplet excitation energies (eV) obtained in the aug-cc-pVTZ basis with respect to the def2-TZVP results.

	TDDFT	evGW		qsGW
		BSE	cBSE	BSE
MSD	-0.02	-0.28	-0.26	-0.03
MAD	0.02	0.28	0.27	0.03
RMS	0.03	0.38	0.36	0.04
MAX	0.10	1.01	1.06	0.14
MED	0.02	0.21	0.22	0.03

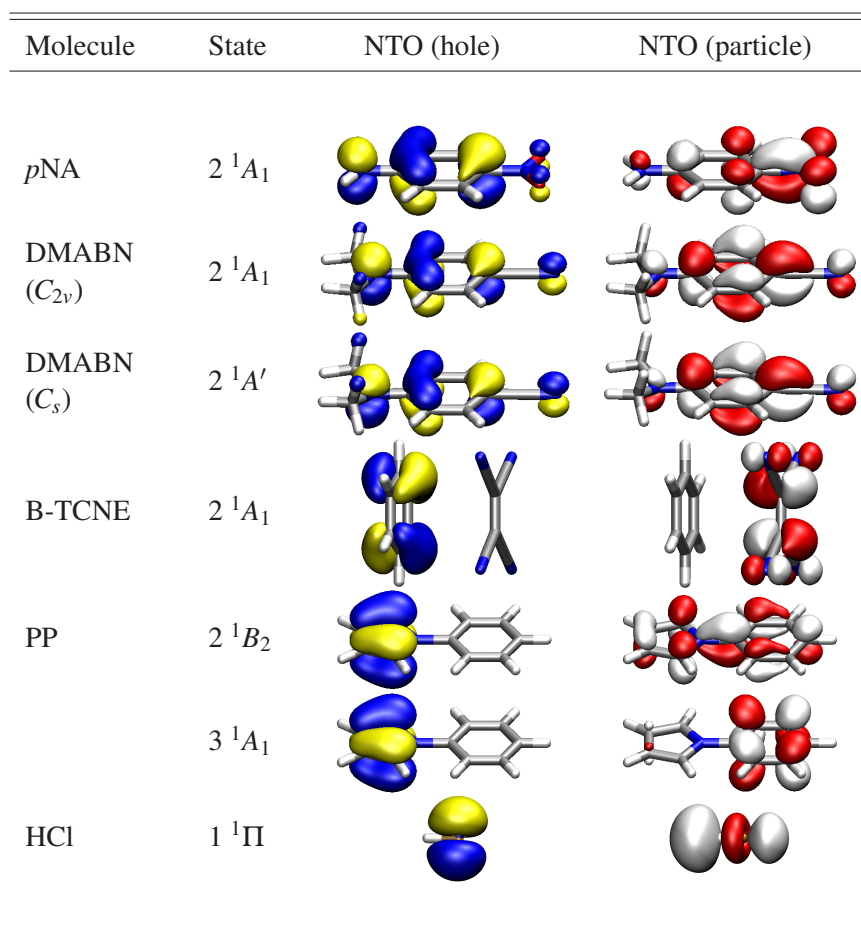
quasiparticle energies from a preceding GW calculation, the failure of obtaining them in GW will be automatically carried over to (c)BSE, which leads to the deterioration in the excitation energies with respect to the reference values. Therefore, the medium-sized def2-TZVP basis set is recommended for the evGW/(c)BSE model.

3.2 Charge-transfer states

The charge-transfer (CT) states of *para*-nitroaniline (pNA), dimethylaminobenzonitrile (DMABN), the benzene-tetracyanoethylene complex (B-TCNE), phenylpyrrole (PP), and HCl were investigated to validate the evGW/(c)BSE scheme. The excitation energies were calculated using the PBE0 functional and def2-TZVP basis set, and the CC3/aug-cc-pVTZ results (CC2/aug-cc-pVTZ for B-TCNE) are adopted as reference values (Table 3.7).

Table 3.7: Singlet excitation energies (eV) and diagnostics Λ of charge-transfer (CT) states.

Molecule	State	evGW-BSE	evGW-cBSE	Λ	Reference
<i>p</i> NA	2 1A_1	4.47	4.50	0.61	4.39
DMABN (C_{2v})	2 1A_1	4.86	4.98	0.74	4.86
DMABN (C_s)	2 $^1A'$	4.80	4.92	0.75	4.75
B-TCNE	2 1A_1	3.45	3.44	0.20	3.41
PP	2 1B_2	5.18	5.27	0.63	5.21
	3 1A_1	5.92	5.89	0.24	5.69
HCl	1 $^1\Pi$	7.66	7.82	0.51	7.81

Figure 3.2: Dominating occupied (blue/yellow) and virtual (red/white) natural transition orbitals (NTOs, iso-value: $\pm 0.04a_0^{-3/2}$) obtained from PBE0 evGW-BSE/def2-TZVP.

The diagnostic Λ is an overlap criterion of the dominating occupied and virtual natural transition orbitals (NTOs) of the respective excitation^[5,71], and smaller Λ corresponds to more prominent CT character. It can be seen that the evGW/BSE and cBSE results are in good mutual agreement with each other, and also compare well with the reference values. Especially for small values of Λ , i.e. B-TCNE and PP, the BSE and cBSE results are virtually identical due to the fact that they converge to the same asymptotic limit. And for larger values of Λ , the same trend as for standard singlet excitations is observed, i.e. cBSE gives slightly higher excitation energies in comparison with BSE. Therefore, BSE and cBSE treat CT excitations on the same footing and they both give correct results, which is an important advantage over TDDFT.

3.3 Timings

Tables 3.8 and 3.9 give the timings for the TDDFT and GW/BSE computations of 40 singlet excitation energies (five in each irreducible representation of the D_{2h} point group) of five aromatic hydrocarbons: benzene, naphthalene, anthracene, tetracene, and pentacene.

Table 3.8 shows that the CPU times for the TDDFT and BSE approaches are of the same order of magnitude, which is as expected^[72]. Furthermore, the CPU times for the evGW part of the calculations are fully acceptable, which is quite remarkable concerning the fact the the full response function is determined in every iteration in order to compute quasiparticle energies for all orbital levels. The CPU times for the qsGW calculations are an order of magnitude larger than for the evGW case, partly because many more iterations were needed to converge the calculations. Since in the present work, no significant advantage of qsGW in comparison with evGW is observed, the latter is recommended for real-world applications of the Bethe–Salpeter formalism.

The dRPA-response part of the GW code has been parallelized, but since not all parts of the whole calculation have been parallelized, the parallel efficiency is not very high on 8 or 16 processors (Table 3.9). According to Amdahl’s law, the speedup is limited by the serial part of the code. Nevertheless, Table 3.9 shows that in particular evGW calculations on larger systems such as pentacene in the def2-TZVP basis can be performed in reasonable time (ca. 17 minutes) on a standard Intel[®] Xeon[®] server node.

C₈₄ fullerene

In order to assess the performance of GW/BSE in real-world applications, a D_2 -symmetric isomer of the fullerene C₈₄ has been studied. As this is a chiral isomer, it offers the opportunity to simulate an electronic circular-dichroism (ECD) spectrum based on BSE calculations of singlet excited states. The calculations were performed for the enantiomer with (fA) configura-

Table 3.8: CPU times (min) for TDDFT and GW/BSE computations in the def2-TZVP basis on a single core of an Intel[®] Xeon[®] E5-2687W v2 (25M Cache, 3.40 GHz) processor. The number of iterations is given in the parentheses.

	TDDFT	evGW/BSE		qsGW/BSE	
		evGW	BSE	qsGW	BSE
Benzene	1.4(8)	0.4(6)	0.7(11)	2.5(13)	0.7(11)
Naphthalene	5.1(9)	2.3(5)	3.3(15)	23.7(17)	3.2(13)
Anthracene	12.5(8)	9.4(5)	9.4(13)	122.7(21)	9.6(13)
Tetracene	24.9(11)	35.6(6)	20.4(15)	510.9(28)	20.8(15)
Pentacene	44.8(9)	88.8(4)	41.5(18)	851.4(16)	40.4(16)

Table 3.9: Wall clock times (min) for GW computations in the def2-TZVP basis on different numbers of cores of an Intel[®] Xeon[®] E5-2687W v2 (25M Cache, 3.40 GHz) processor.

# Cores	evGW					qsGW				
	1	2	4	8	16	1	2	4	8	16
C ₆ H ₆	0.4	0.4	0.4	0.4	0.4	2.5	2.2	1.7	1.4	1.2
C ₁₀ H ₈	2.3	1.8	1.6	1.6	1.6	23.7	20.3	12.8	9.1	8.0
C ₁₄ H ₁₀	9.4	6.5	5.2	4.4	4.2	122.8	107.0	63.9	41.1	31.0
C ₁₈ H ₁₂	35.6	23.0	15.9	12.4	11.4	511.3	436.5	246.2	149.7	105.2
C ₂₂ H ₁₄	88.9	56.1	33.5	22.0	16.7	852.1	707.2	383.4	216.7	135.9

tion according to the configurational descriptor system of Thilgen, Herrmann and Diederich (Figure 3.3).^[73] Experimental ECD spectra were already reported for this enantiomer in the literature in the 1990s.^[74,75] TDDFT investigations followed soon.^[76–78]

In the present work, the equilibrium structure of the (*f*A)-*D*₂-C₈₄ enantiomer was optimized at the PBE0/def2-SVP level, the quasiparticle energies were determined at the evGW level, and 150 excitation energies (50 excitations in each of the irreducible representations *B*₁, *B*₂, and *B*₃) as well as rotatory strengths were computed using the BSE formalism. From these energies and rotatory strengths, the ECD spectrum were simulated as shown in Figure 3.4. In the simulation, the bands were broadened by means of Gaussians with full width at half maximum (FWHM) of 0.35 eV, and the spectrum was scaled by a factor of 1/14 (this is the same scaling factor as used in Ref. 76). It should be noted that the simulated spectrum was neither red- nor blue-shifted.

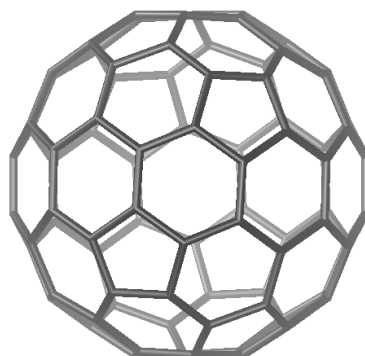


Figure 3.3: PBE0/def2-SVP structure of (*fA*)- D_2 - C_{84} . Reprinted with permission from Ref. 5. Copyright 2018 American Chemical Society.

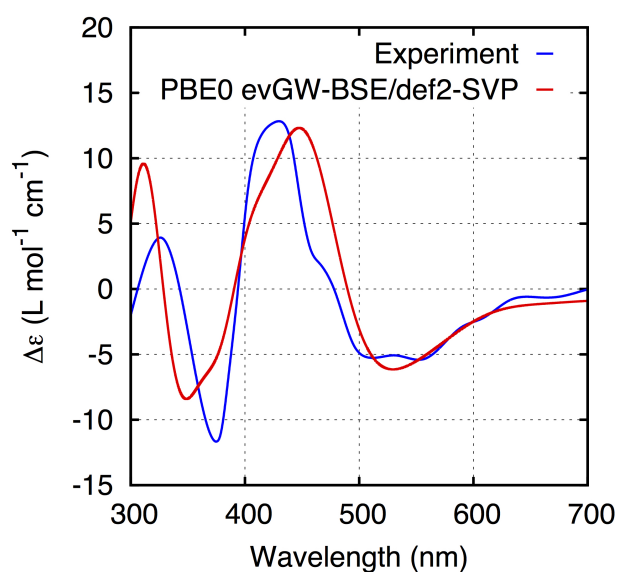


Figure 3.4: Simulated ECD spectrum of (*fA*)- D_2 - C_{84} compared to experiment^[74]. Gaussian broadening with FWHM = 0.35 eV. Calculated $\Delta\epsilon$ values were scaled with 1/14. Reprinted with permission from Ref. 5. Copyright 2018 American Chemical Society.

For C_{84} , the def2-SVP basis comprises 1,176 basis functions. With 252 doubly occupied orbitals, this yields a total tensor space of dimension 232,848. Fortunately, exploiting D_2 symmetry reduces the complexity of the calculation to four tensor spaces of sizes 58,206, 58,210, 58,216, and 58,216 for the four irreducible representations of the point group. On eight cores of an Intel[®] Xeon[®] E5-2687W v4 @ 3.00 GHz processor, the evGW calculation took 65 hours (five iterations). The subsequent BSE calculation took 185 hours on a single core of an Intel[®] Xeon[®] E5-4640 @ 2.40 GHz processor.

3.4 Conclusion

It has been demonstrated that the Bethe–Salpeter formalism is an interesting and valid alternative to the time-dependent DFT approach, and the CPU and wall-clock computation times of both the Bethe–Salpeter calculations themselves as well as the underlying GW calculations of the required quasiparticle energies are fully acceptable, thus allowing for real-world applications of the theory. In order to achieve the balance between accuracy and efficiency, our method of choice is $evGW/BSE$, or $evGW/cBSE$ when triplets are involved.

4 Photoinitiated charge-transfer in a triangular silver(I) hydride complex

4.1 Introduction

Multinuclear coinage metal hydrides (CMHs) are fascinating synthetic targets with promising applications in energy storage and photocatalysis.^[79,80] In catalytic studies, besides the dominating application of copper hydrides, interesting perspectives on silver and gold species have also gained much attention due to their distinctive (photo)reactivity. To better understand the photochemistry of CMHs as well as transition metal hydrides, more studies are needed to correlate the physico-optical properties of CMHs (UV spectra, cross-sections, types of transitions), their molecular structures (hydride coordinating motif), and the primary photoproducts. In this chapter, a trinuclear silver hydride $[\text{Ag}_3(\mu_3\text{-H})(\mu_2\text{-L}^{\text{Cy}})_3]^{2+}$ ($[\text{P}]^{2+}$, $\text{L}^{\text{Cy}} = \text{dcpm} = \text{bis}(\text{dicyclohexylphosphino})\text{methane}$) will be studied to further explore the silver-hydride-centered electronic transitions and the cooperative metallophilic interactions.

4.2 Structural examination and geometry optimization

In the solid-state structure of $[\text{P}](\text{PF}_6)_2$ (Figure 4.1a), the three silver centers are μ_3 -bridged by the central hydrido ligand, resulting in a distorted trigonal planar coordination for each silver site. Three silver atoms form a nearly equilateral triangle, and the average $\text{Ag}\cdots\text{Ag}$ distance is 3.082 Å, which is shorter than twice the van der Waals radius of silver (3.44 Å)^[81] and thus in the range of argentophilic $d^{10}\text{-}d^{10}$ interactions. The average $\text{Ag}\cdots\text{H}$ distance is 1.779 Å. A C_2 axis runs through the atoms Ag1 and H1, which determines the symmetry of the $(\widehat{\text{PP}})_3\text{Ag}_3(\text{H})$ core.

In the quantum chemical calculation, the ground-state equilibrium geometry of $[\text{P}]^{2+}$ was first optimized in C_2 symmetry at the PBE-D3(BJ) level of theory^[68,83,84] starting from the obtained X-ray diffraction structure. For the central hydrogen, the def2-TZVP basis set was used for geometry optimization and the def2-TZVPP basis set for further calculating the electronic excitation energies. The def2-SV(P) basis set was taken for all the other atoms. Because the calculated harmonic vibrational frequencies comprised one imaginary frequency, the geometry was re-optimized in C_1 symmetry yielding a true minimum with only real frequencies. This

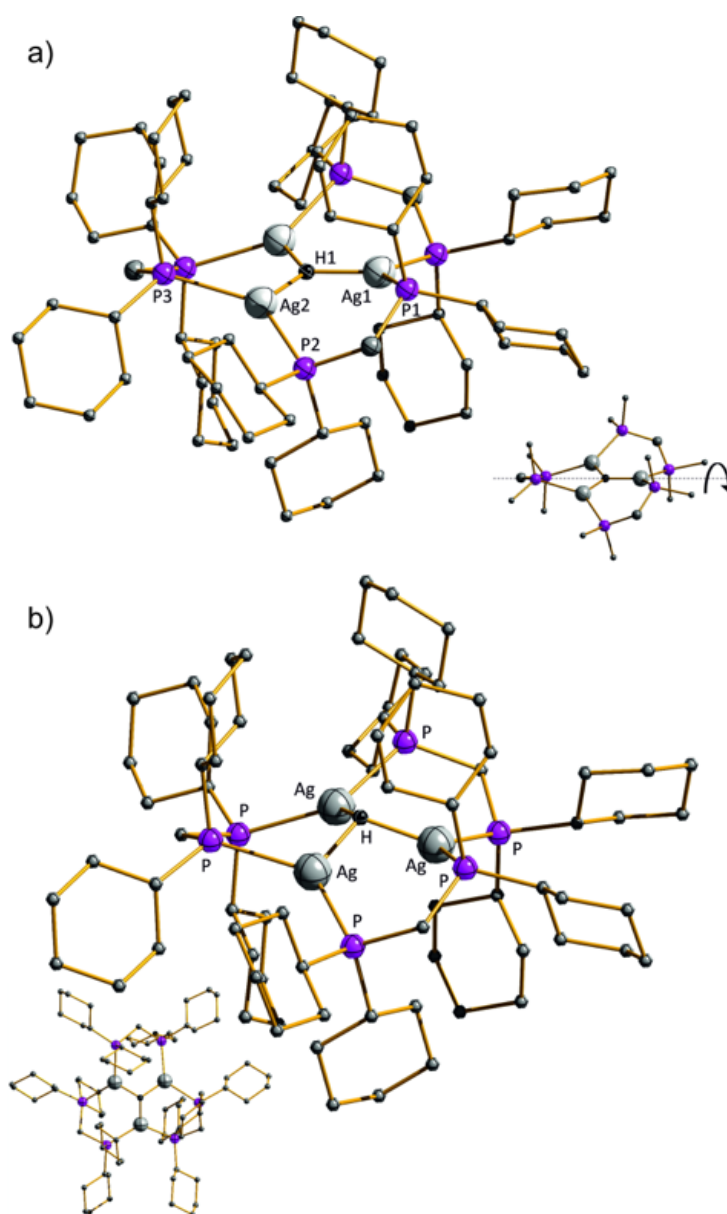


Figure 4.1: a) Solid-state structure of $[\text{P}](\text{PF}_6)_2$. Hydrogen atoms and hexafluorophosphate anions are omitted for clarity. Inset: illustration of the pseudo- C_2 axis passing through the Ag1 and H1 atoms. b) Optimized structure of $[\text{P}]^{2+}$ at the PBE-D3(BJ)/def2-SV(P) level of theory. Hydrogen atoms are omitted for clarity. Inset: top view. Reprinted with permission from Ref. 82. Copyright 2019 John Wiley & Sons.

optimized ground-state structure (Figure 4.1b) is in good agreement with the experimental X-ray diffraction results, featuring slightly shorter $\text{Ag}\cdots\text{Ag}$ distance (3.023 Å) and slightly longer $\text{Ag}\cdots\text{H}$ distance (1.853 Å). The main difference between the experimental and computed structures lies in the position of the central hydrogen atom and the accompanying $\text{Ag}\cdots\text{H}$ distance.

The calculation gave a clear preference for a position that is located out of the Ag_3 plane by around 0.6 \AA , whereas the experimental results exhibit an in-plane hydride localization. However, a small displacement of the hydride ligand cannot be completely ruled out. And this structure is further validated by comparison of the calculated electronic transitions with the experimental absorption spectrum. A natural population analysis revealed that the silver centers carry an average partial charge of $0.56e$, and the central hydrogen carries a partial charge of $-0.59e$, indicating its hydridic character.

4.3 Optical properties and electronic structure

At the optimized geometry, quasiparticle energies were determined at the *evGW* level with the PBE0 functional. The standard SR-GW was not applicable in this case. Therefore, the calculations were performed with the low-scaling AC-GW variant. The resulting orbitals near the Fermi level are presented in Figure 4.2. It can be seen that the HOMO-LUMO gap, which is much too small at the PBE0 level, is substantially increased at the *evGW* level, which aims to correct deficiencies in the PBE0 orbital energies. All the other orbital levels are shifted according to the new HOMO and LUMO while preserving the Kohn-Sham energy spacing, yielding larger excitation energies. The orbital plots identify the electronic interactions between the hydride and Ag_3 moieties, which allows the experimental absorption spectrum to be unraveled.

Based on the quasiparticle energies obtained from the *evGW* calculation, the singlet excitation energies were computed using the Bethe–Salpeter equation (BSE) formalism. The calculated spectrum together with the experimental UV/Vis absorption spectroscopy in the gas phase and solution are presented in Figure 4.3. The UV-PD spectrum of gaseous $[\text{P}]^{2+}$ (Figure 4.3a, black circles) displays a low-intensity band centered at around 320 nm , a broad asymmetric band peaking at around 252 nm with a shoulder at around 270 nm , and a rising edge of the fragment yield to higher photon energies starting at around 245 nm . The total fragment yield shows a linear dependence on the laser pulse energy, which indicates a one-photon absorption process and justifies the comparison with the linear absorption spectrum in solution. In fact, the overall shape of the UV-PD spectrum closely resembles the absorption spectrum in acetonitrile solution (Figure 4.3a, blue line), although a pronounced blueshift of around 1400 cm^{-1} is discernible with respect to the band maximum at 261 nm observed in the condensed phase. Additionally, the band at around 320 nm in the gas-phase spectrum is slightly broader and differently structured compared with its solution counterpart, and thus the corresponding solvation shift is difficult to ascertain.

The calculated absorption spectrum (Figure 4.3b) is in good agreement with the optical experimental spectra. Based on the *evGW*-BSE calculations, the weak, lowest-energy band at

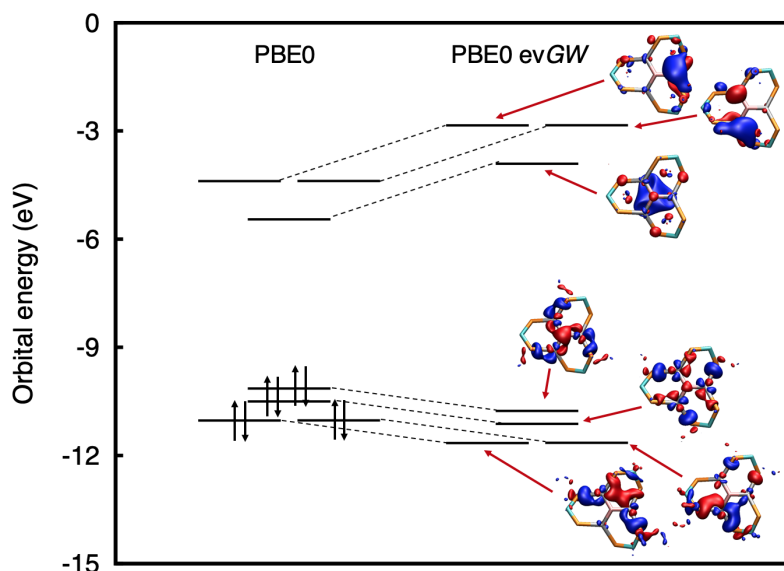


Figure 4.2: Energy levels of the orbitals HOMO-3 to LUMO+2 of $[P]^{2+}$ obtained at the PBE0/def2-SV(P) and PBE0 evGW/def2-SV(P) levels of theory. Orbitals are shown with an isovalue of $\pm 0.04a_0^{-3/2}$. Cyclohexyls and methylene hydrogen atoms are omitted for clarity. Reprinted with permission from Ref. 82. Copyright 2019 John Wiley & Sons.

around 320 nm, observed in both the gas phase and solution, is assigned to a $^1\text{HMCT}$ (hydride-to-metal charge-transfer) transition ($\lambda_{\text{calcd}} = 321 \text{ nm}$, S_1), hence electron density is transferred mainly from a hydride-centered orbital to a collective A_{g3} orbital (LUMO), as illustrated by the transition density plot shown in Figure 4.3b. Because the LUMO facilitates cooperative binding interactions (Figure 4.2), all the electronic transitions exhibiting significant LUMO contributions are expected to enhance the stability of the A_{g3} core. Further evidence of this assignment is provided by the fact that UV-PD mainly leads to fragments with an intact cluster core, which primarily displays ionic core fission. The distinct shoulder (ca. 270 nm), discernible by the apparent asymmetry of the broad PD band in the 280–245 nm spectral range, originates from two nearly degenerate S_3 and S_4 excited states ($\lambda_{\text{calcd}} = 261 \text{ nm}$) with mainly metal-centered character (^1MC). Furthermore, in excellent agreement with the experimental gas-phase maximum at around 252 nm, the calculated UV absorption spectrum is dominated by two almost degenerate transitions (S_5 and S_6) at 250 nm arising mainly from charge-transfer from hydride to silver-centered orbitals ($^1\text{HMCT}$), which corresponds to the absorption maximum in MeCN at around 261 nm. The experimentally observed increase in absorption below 240 nm, both in the gas phase and in solution, is assigned to the excitation of the ^1MC states.

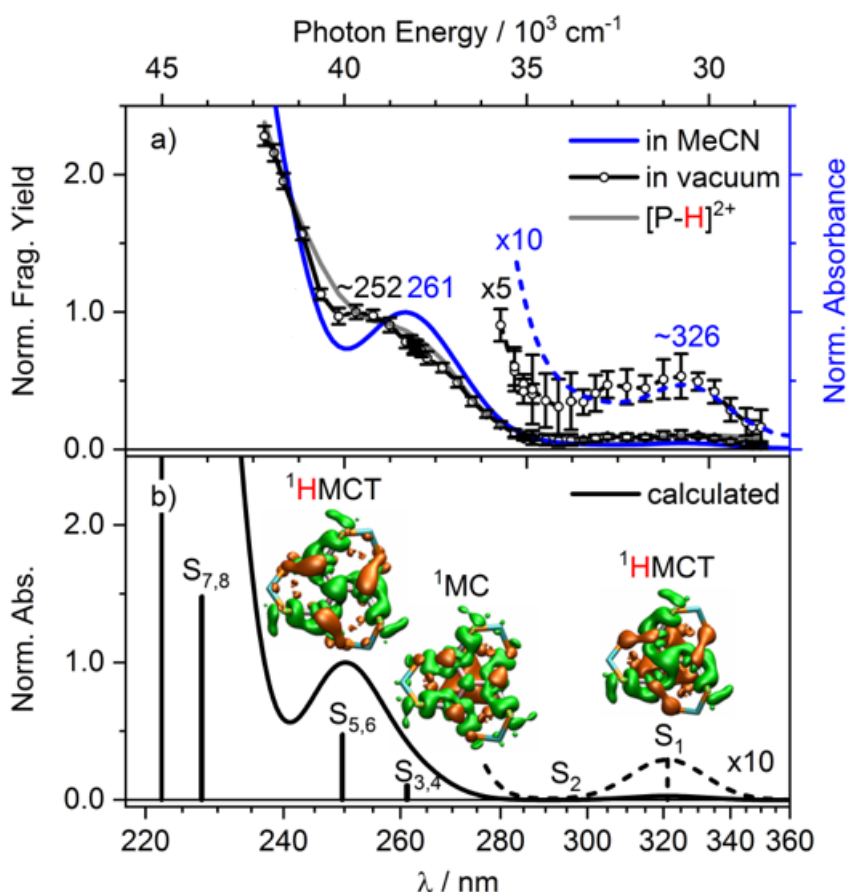


Figure 4.3: a) Normalized UV-PD spectrum of $[P]^{2+}$ (black circles) compared with the UV absorbance spectrum of $[P](PF_6)_2$ in MeCN (blue line). Error bars represent one standard deviation. The yield of the H-loss channel obtained by isotope pattern deconvolution is shown in grey. b) Unscaled calculated electronic absorption (FWHM = 0.3 eV) and stick spectra (PBE0 evGW-BSE/def2-SV(P)) of $[P]^{2+}$. Inset: transition density plots for the labeled S_1 , $S_{3,4}$, $S_{5,6}$ transitions (isovalue: $\pm 0.001 a_0^{-3}$, cyclohexyl and methylene hydrogen atoms are omitted). Green represents a loss of electron density whereas orange represents a gain of electron density. Magnified spectra in the 277–360 nm range ($\times 5$, $\times 10$) are shown as dotted lines. Reprinted with permission from Ref. 82. Copyright 2019 John Wiley & Sons.

To validate the more robust CD-GW scheme, a series of BSE excited state calculations have been done, where quasiparticle energies were optimized for 5, 10, 15 and 20 highest occupied and lowest unoccupied orbitals, respectively. Figure 4.4 illustrates the resulting absorption spectra in comparison with the previous calculated spectrum (Figure 4.3b), where quasiparticle energies were computed from AC-GW that is equivalent to CD-GW optimizing only one single occupied and unoccupied orbitals, i.e. HOMO and LUMO.

As can be clearly seen, when more orbitals are involved, the resulting absorption spectrum is more blue-shifted until convergence is reached. The difference among spectra with 10, 15

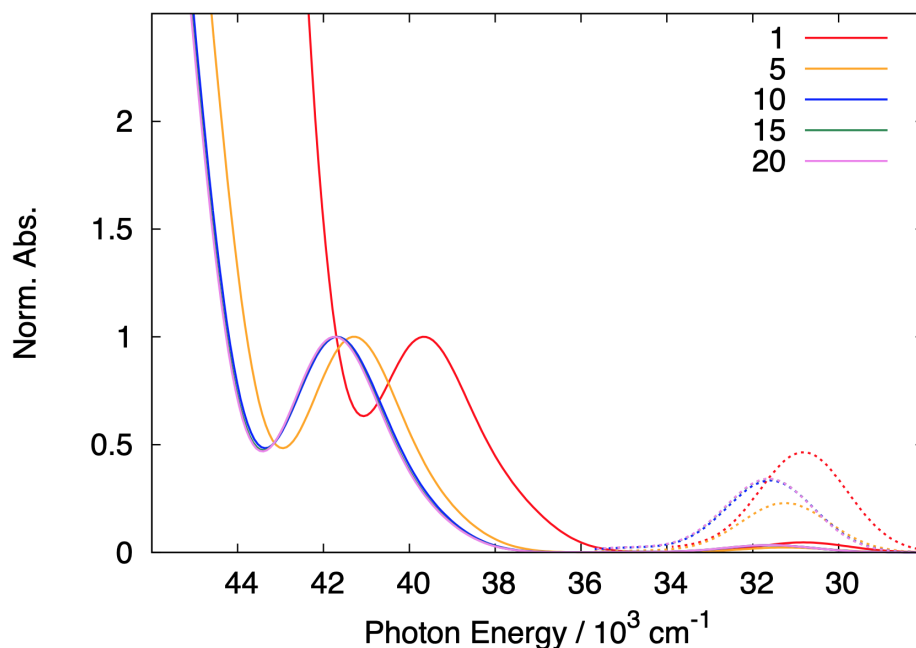


Figure 4.4: Calculated electronic absorption spectra (FWHM = 0.3 eV) of $[P]^{2+}$ at the PBE0 CD-evGW-BSE/def2-SV(P) level of theory, where 1, 5, 10, 15 and 20 highest occupied and lowest unoccupied orbitals were optimized for CD-evGW, respectively. Magnified spectra in the 280-360 nm range ($\times 10$) are shown as dotted lines.

and 20 occupied/unoccupied orbitals is extremely minor, and the latter two almost completely overlap. Therefore, in general, it is more than enough to optimize 10 highest occupied and 10 lowest unoccupied orbitals for a CD-GW calculation. It should be noted that although in this case the AC-GW/BSE spectrum suggests a better agreement with the experimental spectrum, while the CD-GW(10)/BSE spectrum shows a pronounced blueshift of around 2000 cm^{-1} , this is purely coincidental. Theoretically, when more orbitals are included in the calculation, the CD-GW results will more closely resemble the benchmark SR-GW that computes the quasiparticle energies for *all* orbital levels. Therefore, our method of choice is CD-GW, and in the rest of this thesis, if not specified, always 10 highest occupied and 10 lowest unoccupied orbitals are optimized in CD-GW.

4.4 Conclusion

In summary, the silver(I) hydride complex $[Ag_3(\mu_3\text{-H})(\mu_2\text{-L}^{\text{Cy}})_3]^{2+}$ ($[P]^{2+}$) possesses a nearly equilateral triangular Ag_3 core, capped by a central μ_3 -hydrido ligand and stabilized by slightly twisted bis-phosphine ligands, as inferred from combined experimental and theoretical structural analyses. The gas-phase photofragment action spectrum shows hydride-to- Ag_3 charge-

transfer ($^1\text{HMCT}$) and metal-core-centered (^1MC) transitions in the spectral range of 350–240 nm, in accordance with the hypsochromic shifts observed in MeCN solution. This has been directly compared with the results of *GW/BSE* calculations, which excellently reproduced the experimental spectra and facilitated the assignment of the character of electronic transitions by means of transition density plots. Hence, the low-scaling *AC-GW* and *CD-GW* variants make calculations feasible for systems with hundreds of atoms and thousands of basis functions. And the combined experimental and theoretical results provide a basis for further detailed spectroscopic investigations, specifically for studying metal–metal interactions under electronic excitation and identification of hydride charge-transfer processes.

5 A tetranuclear silver(I) iodide complex: cube and chair isomers

5.1 Introduction

Design, synthesis, and characterization of polynuclear d^{10} metal complexes have attracted widespread interest due to their intrinsic aesthetic appeal and potential applications in heterogeneous catalysts and luminescent materials. Compared to the copper(I) and gold(I) congeners, the photophysical properties of silver(I) complexes are relatively less studied mainly due to their thermal instability and light sensibility. A classical example of multinuclear Ag(I) complexes is $\text{Ag}_4\text{I}_4(\text{PPh}_3)_4$, which contains a metal-halide core and neutral phosphine bridging ligands. This tetramer can exist in a cubane- or chair-like conformation (Figure 5.1), and both were found to be luminescent originating from a $4d \rightarrow 5s$ metal-centered excited state.^[85,86] The cubane-like isomer emits at a lower energy due to the higher delocalization over the $4d$ and $5s$ orbitals of the Ag(I) centers. In this chapter, a similar tetranuclear silver(I) iodide complex will be presented, which is bridged by diphenyl-2-pyridylphosphine (PyrPhos) derivatives with a methyl group in *para* position of the pyridine ring. The tetramer will be denoted as $\text{Ag}_4\text{I}_4\text{L}_4$ (L = MePyrPhos) in further discussions.

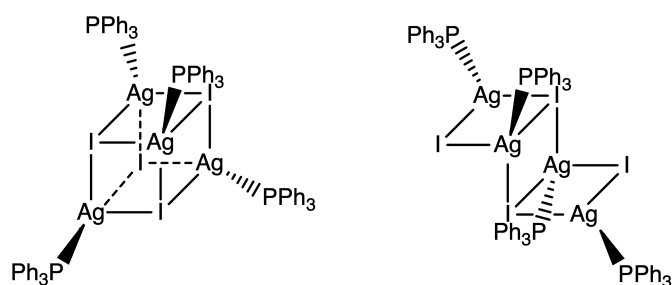


Figure 5.1: Cube and chair isomers of $\text{Ag}_4\text{I}_4(\text{PPh}_3)_4$. The chair isomer can be considered as derived from the cube isomer via cleavage of two Ag–I bonds in one Ag_2I_2 face followed by rotation of one adjacent Ag_2I_2 face by approximately 180° .

5.2 Cubane-like isomer

5.2.1 Structural examination and geometry optimization

In the solid state structure of $\text{Ag}_4\text{I}_4\text{L}_4$ (Figure 5.2), the $\text{Ag}_4\text{I}_4\text{P}_4$ core shows a highly distorted cubane-like configuration with two interpenetrating silver and iodine tetrahedra situated on alternate corners of the cube. Each silver atom is coordinated by three μ_3 -bridging iodine atoms and further coordinated to a phosphine ligand. The distortion from the idealized T_d symmetry due to steric hindrance can be seen in the variation of the following molecular parameters. First, the $\text{Ag}\cdots\text{Ag}$ distances span from 3.157 to 3.427 Å, with an average of 3.302 Å, which are all in the range of argentophilic $d^{10}\text{-}d^{10}$ interactions. Second, the $\text{I}\cdots\text{I}$ distances span from 4.492 to 4.813 Å, with an average of 4.636 Å, which are all greater than twice the van der Waals radius of iodine (4.32 Å)^[81], indicating the repulsion of iodine ions. And for each nonplanar Ag_2I_2 moiety, shorter $\text{I}\cdots\text{I}$ distances are in general accompanied by longer $\text{Ag}\cdots\text{Ag}$ distances, and vice versa. Third, the Ag-I bond lengths range from 2.816 to 2.926 Å, with an average of 2.887 Å, and the Ag-I-Ag bond angles range from 65.64 to 73.31°, with an average of 69.79°.

In the quantum chemical calculation, the ground-state equilibrium geometry of cubane-like $\text{Ag}_4\text{I}_4\text{L}_4$ was optimized in S_4 symmetry at the PBE0-D3(BJ) level of theory starting from the distorted cube configuration. The def2-TZVP basis set was taken for Ag, I, P, N, and C atoms in pyridine rings, and the def2-SV(P) basis set was taken for the rest of the atoms. This combination will be referred to as "TZVP" in further discussions. A true energy minimum with only real harmonic vibrational frequencies was achieved, and hence the favorable S_4 symmetry was retained. This optimized ground-state structure (Figure 5.3) is in good agreement with the experimental X-ray diffraction results, only being more symmetric, featuring shorter $\text{Ag}\cdots\text{Ag}$ distances (average 3.009 Å) and longer $\text{I}\cdots\text{I}$ distances (average 4.873 Å) as well as acuter Ag-I-Ag bond angles (average 61.48°). And the average Ag-I bond length is 2.940 Å, which is slightly longer than the experimental result.

5.2.2 Absorption spectra

The $\text{Ag}_4\text{I}_4\text{L}_4$ tetramer has very low solubility in dichloromethane (DCM). And dimethyl sulfoxide (DMSO), which is a good alternative solvent for hardly soluble compounds, has a self-absorption band that starts around 310-320 nm and unfortunately cannot be used here. Hence, chloroform (CHCl_3) was used as solvent, but it should be noted that CHCl_3 has a strong self-absorption band at around 270 nm. As shown in Figure 5.4, the spectrum of $\text{Ag}_4\text{I}_4\text{L}_4$ in CH_3Cl (black solid line) exhibits a broad absorption band from 300 to 350 nm, which is not related to the bridging ligands (black dashed line). Besides, there appears an unexpected bump at 425

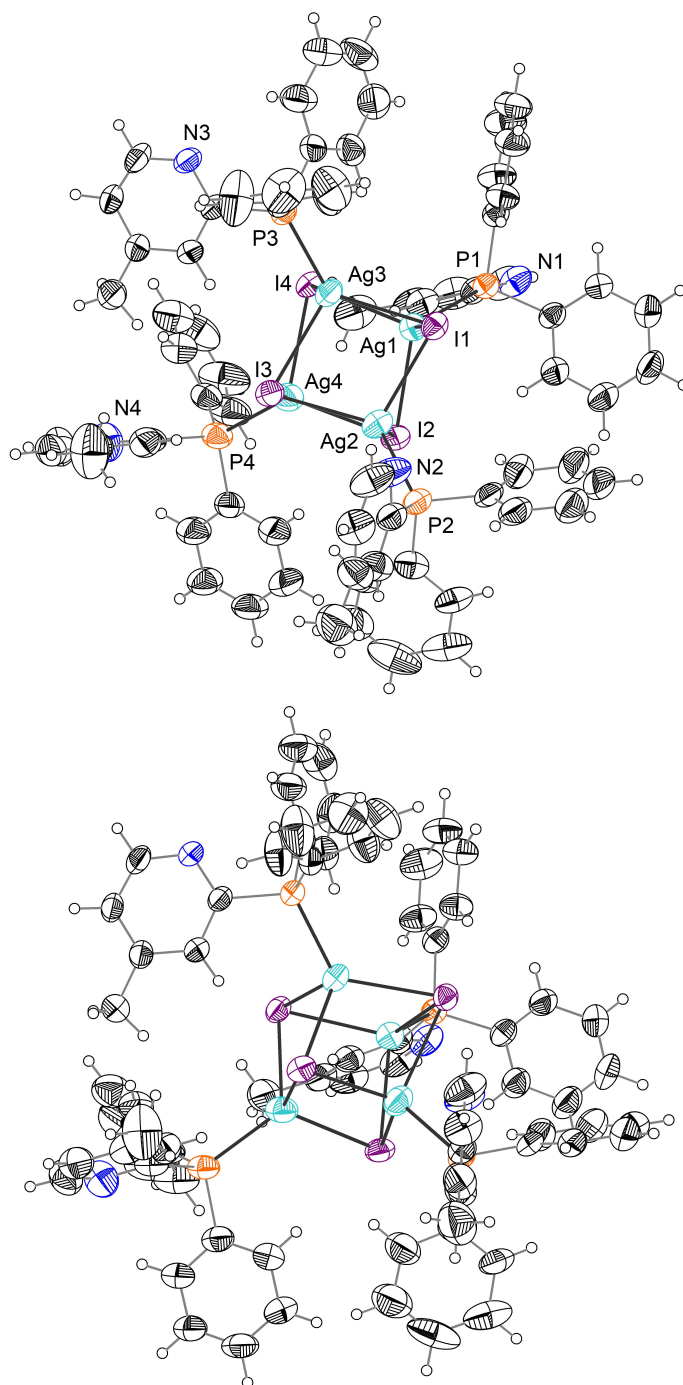


Figure 5.2: ORTEP plots of $\text{Ag}_4\text{I}_4\text{L}_4$ (top and side view) shown at the 50% probability level. Results provided by Jasmin Busch (IOC), measured and solved by Olaf Fuhr (INT).

nm, which was not seen in the solid phase spectrum from a neat film on a CaF_2 window. However, the device could only record up to 320 nm. And it is not possible to record absorption spectra in a KBr matrix at the moment. Hence, no satisfying solid phase spectra is available for comparison.

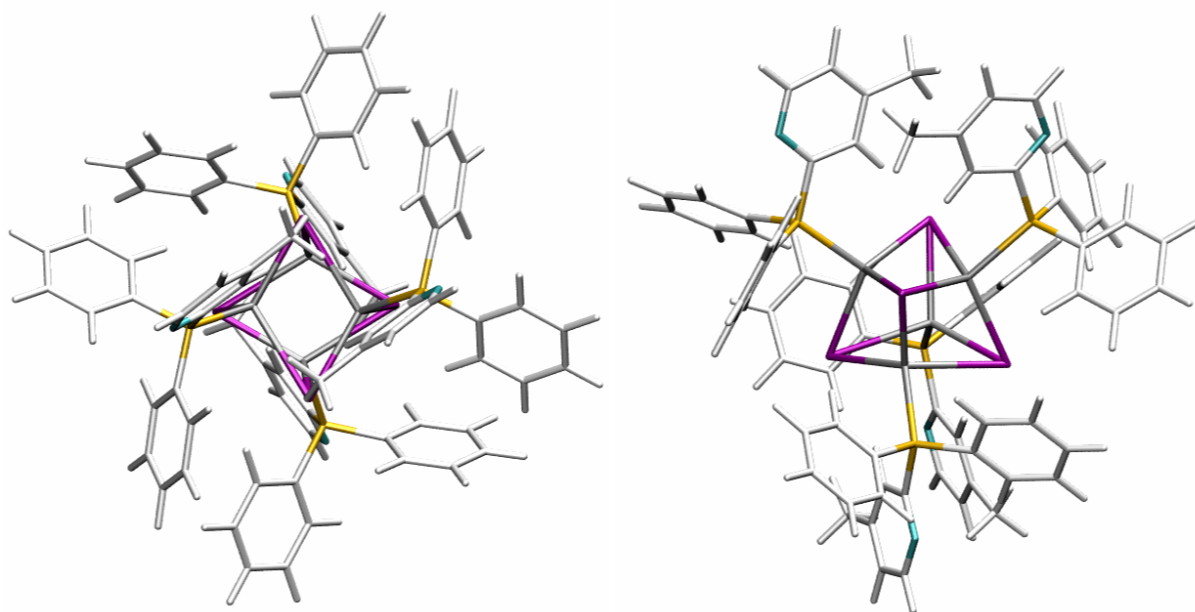


Figure 5.3: Optimized ground-state structure of Ag₄I₄L₄ (top and side view) at the PBE0-D3(BJ)/TZVP level of theory. Color code: Ag (silver), I (purple), P (yellow), N (cyan), C and H (white).

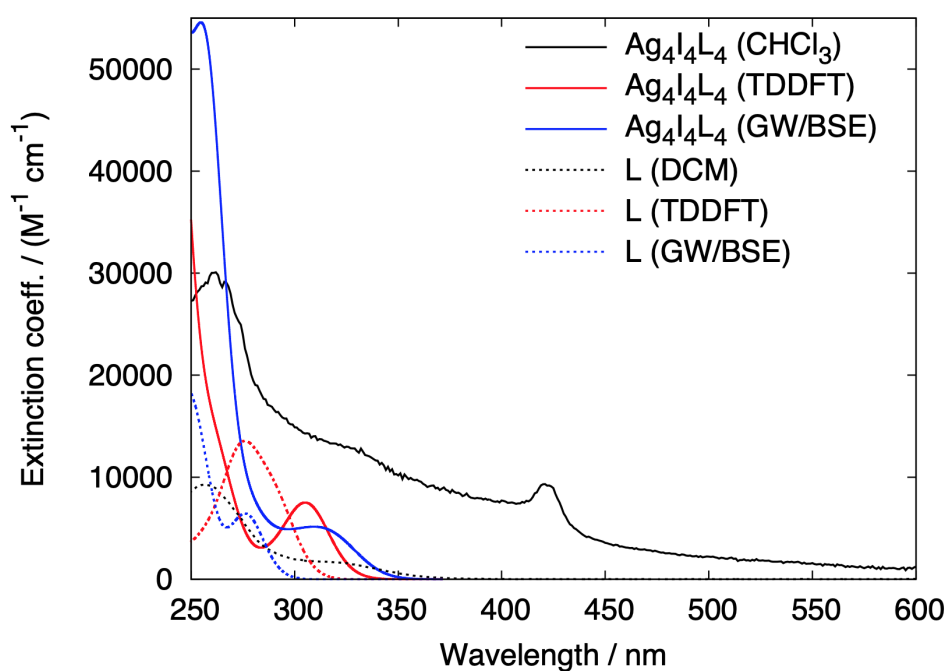


Figure 5.4: UV/Vis spectra of Ag₄I₄L₄ in CHCl₃ (black solid line) and L in DCM (black dashed line) compared to calculated absorption spectra (FWHM = 0.3 eV) using TD-CAM-B3LYP (red lines) and PBE0 CD-evGW/BSE (blue lines).

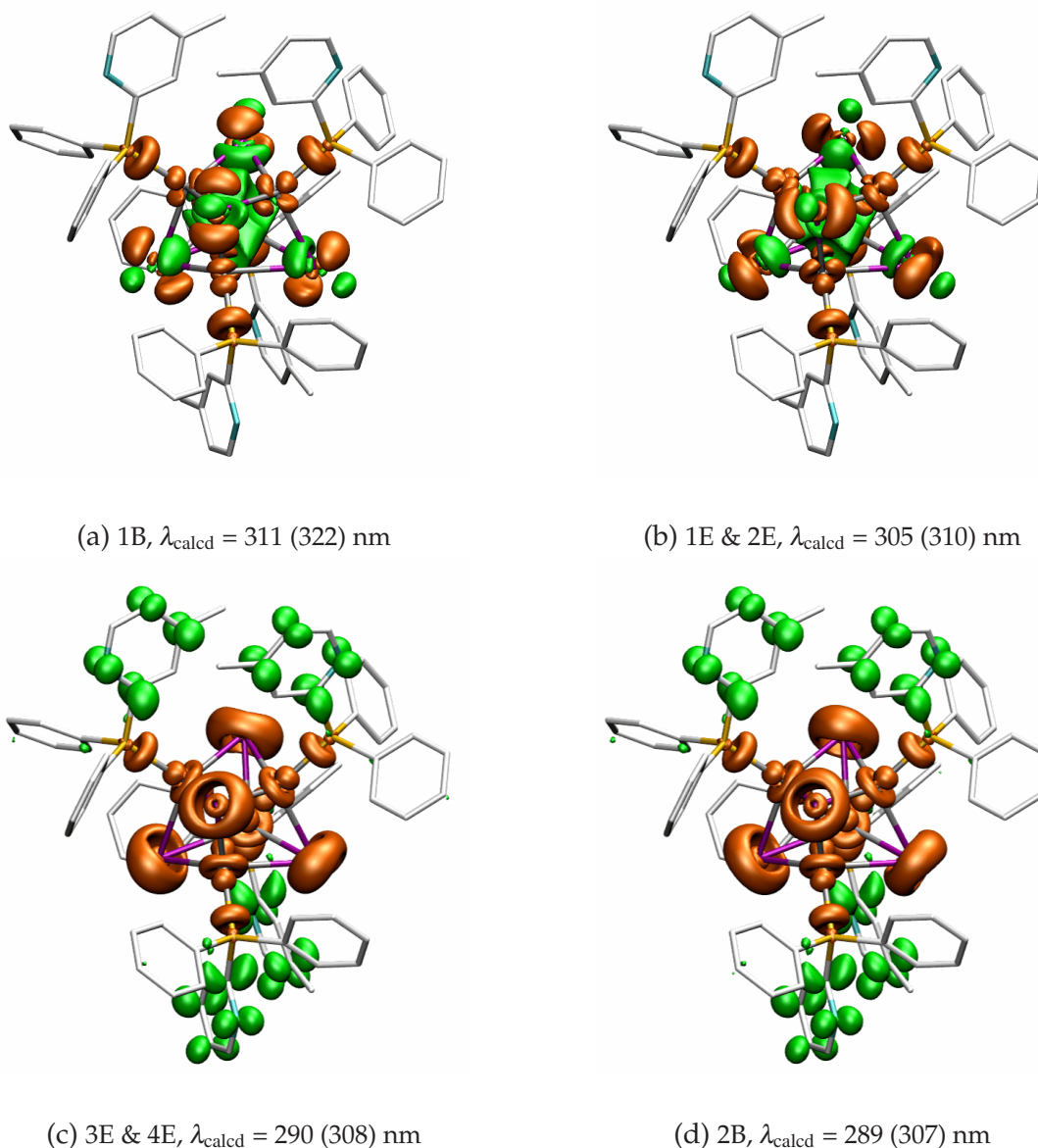


Figure 5.5: Transition density plots and excitation energies for the transitions involved in the TD-CAM-B3LYP absorption band centered at 305 nm (isovalue: $\pm 0.0015a_0^{-3}$, all hydrogen atoms are omitted for clarity). Green represents a gain of electron density whereas orange represents a loss of electron density. The corresponding PBE0 CD-evGW/BSE excitation energies are listed in parentheses for comparison.

The electronic excitation energies were calculated using TDDFT with CAM-B3LYP functional^[87] and CD-evGW/BSE with PBE0 functional employing the TZVP basis set. The calculated absorption spectra of $\text{Ag}_4\text{I}_4\text{L}_4$ are in good mutual agreement, and both agrees well with the experimental results. The TDDFT spectrum (Figure 5.4, red solid line) displays a narrow band centered at 305 nm, while the GW/BSE spectrum (Figure 5.4, blue solid line) dis-

plays a broad band centered at 310 nm, For both methods, this band has contributions from a number of excitations in B and E symmetry, and the corresponding transition density plots are given in Figure 5.5. The 1B and degenerate 1E and 2E excited states are mainly centered at the metal–halide core, while the 2B and degenerate 3E and 4E excited states arise mainly from metal–halide to ligand charge-transfer (X+M)LCT.

5.3 Chair-like isomer

5.3.1 Geometry optimization

Experimentally, no crystallization of the chair-like configuration of $\text{Ag}_4\text{I}_4\text{L}_4$ has been achieved so far. In the quantum chemical calculation, the ground-state equilibrium geometry of chair-like $\text{Ag}_4\text{I}_4\text{L}_4$ was optimized in C_i symmetry at the PBE0-D3(BJ)/TZVP level of theory, and a true energy minimum with only real harmonic vibrational frequencies was obtained, which is ca. 4 eV higher in energy than the cubane-like isomer. In contrast to the cubane-like isomer that is defined by six highly nonplanar Ag_2I_2 moieties, the chair-like isomer is defined by three Ag_2I_2 moieties: two nonplanar Ag_2I_2 fragments connected by one strictly planar Ag_2I_2 in the middle (Figure 5.6). The $\text{Ag}\cdots\text{Ag}$ distances differ substantially within the nonplanar (2.908 Å) and planar (3.188 Å) Ag_2I_2 moieties. In comparison, the $\text{I}\cdots\text{I}$ distances show less variation within the nonplanar (4.922 Å) and planar (4.841 Å) Ag_2I_2 moieties. The four silver atoms, the four iodine atoms, as well as the four phosphorus atoms are also precisely coplanar as required by the symmetry. The four Ag atoms form a parallelogram with edges of 4.583 and 2.908 Å, with a short diagonal of 3.188 Å. Likewise, the four I atoms form a parallelogram with edges of 4.536 and 4.922 Å, with a short diagonal of 4.841 Å.

The most important feature of the chair-like isomer is that the metal–halide core atoms have variable coordination numbers (CN). It can be obviously seen from Figure 5.6 that two Ag atoms are trigonal-coordinated (CN = 3), while another two silver atoms are tetrahedral-coordinated (CN = 4). Similarly, two I atoms are μ_2 -bridging (CN = 2), while another two iodine atoms are μ_3 -bridging (CN = 3). Within the nonplanar Ag_2I_2 moieties, the Ag–I bond lengths can be nicely correlated with the coordination numbers. Let m and n be coordination numbers of the Ag and I atoms: as (m, n) increases from (3, 2) to (3, 3), the Ag–I bond length increases from 2.713 to 2.887 Å; as (m, n) increases from (4, 2) to (4, 3), the Ag–I bond length increases from 2.881 to 2.988 Å. The remaining two Ag–I bond lengths within the planar Ag_2I_2 moiety are 2.806 Å. The metal coordination number is closely reflected in the I–Ag–I bond angles. The I–Ag–I bond angle with Ag (CN = 3) is 123°, which is close to the ideal trigonal value of 120°, while the I–Ag–I bond angles with Ag (CN = 4) have an average value of 111°, which is close

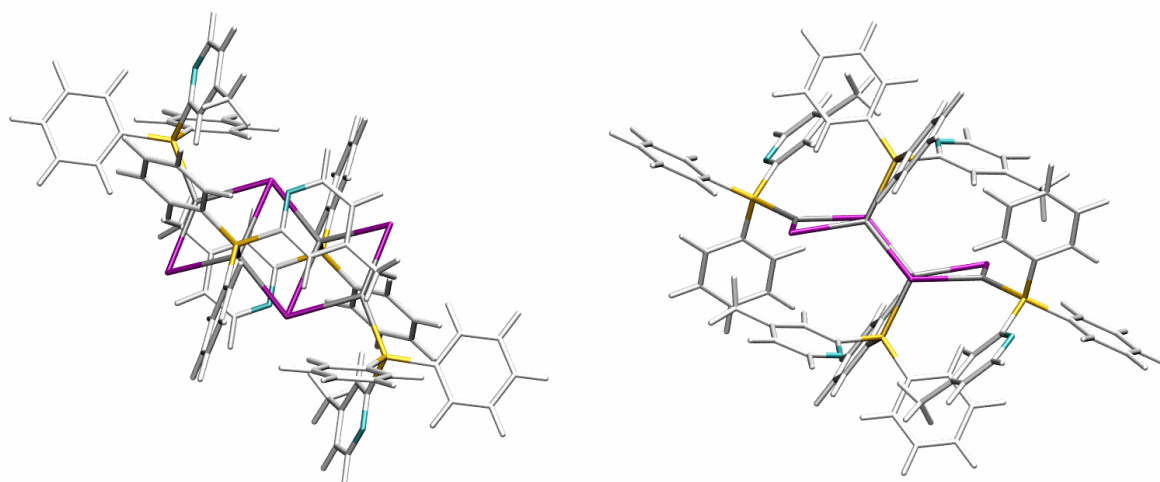


Figure 5.6: Optimized ground-state structure of the chair-like isomer of $\text{Ag}_4\text{I}_4\text{L}_4$ (top and side view) at the PBE0-D3(BJ)/TZVP level of theory. Color code: Ag (silver), I (purple), P (yellow), N (cyan), C and H (white).

to the ideal tetrahedral value of 109.5° . The Ag–I–Ag angles are highly acute within both the nonplanar (62.6° and 59.3°) and planar (66.7°) Ag_2I_2 moieties.

When comparing the structural parameters of the cubane- and chair-like isomers, a resemblance between the nonplanar Ag_2I_2 moieties can be easily seen, while the major difference lies in the Ag \cdots Ag distance. In the chair form, the Ag \cdots Ag distance of 4.536 \AA across the bridge is significantly longer than every Ag \cdots Ag distance in the distorted cube form, indicating a huge relief of repulsion between the phenyl/pyridyl groups of the phosphines attached to these two Ag atoms. This is supposed to be the driving force in the cube \rightarrow chair isomerization.

5.3.2 Absorption spectra

For the chair-like isomer, the electronic excitation energies were calculated in the same manner as for the cubane-like isomer. The predicted absorption spectra are in good mutual agreement (Figure 5.7), featuring an absorption band centered at 272 nm for TDDFT and 270 nm for GW/BSE. For both methods, this band has contributions from two A_u excitations, and the corresponding transition density plots (Figure 5.8) exhibit the (X+M)LCT character.

5.4 Conclusion

In summary, the tetranuclear silver(I) iodide complex $\text{Ag}_4\text{I}_4\text{L}_4$ ($L = \text{MePyrPhos}$) has been shown by quantum chemical calculations to exist in either a cubane- or a chair-like structure, though only the cubane-like isomer has been crystallized experimentally. The cubane-like isomer possesses a metal–halide core with four silver and four iodine atoms situated on al-

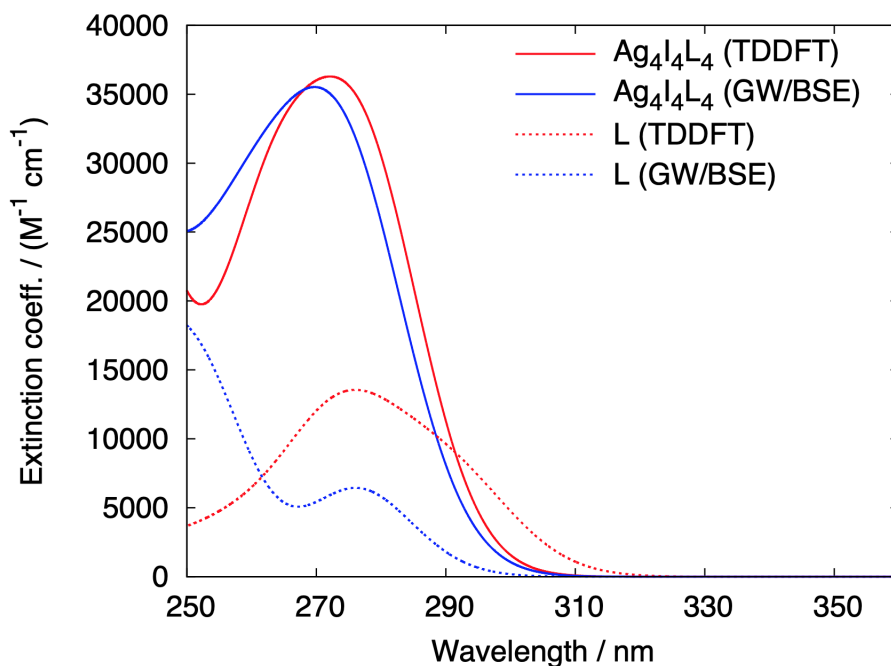
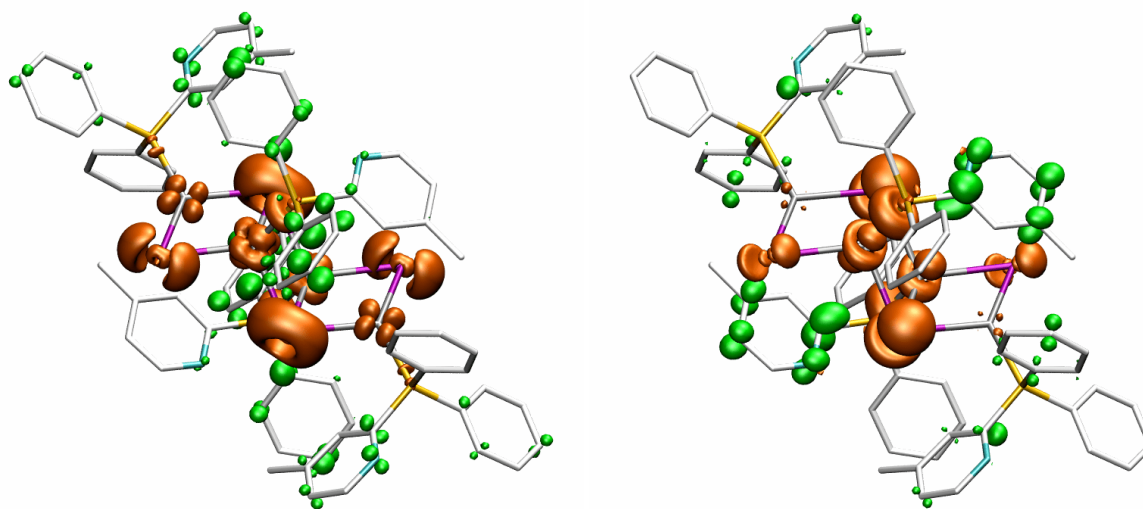


Figure 5.7: Calculated absorption spectra (FWHM = 0.3 eV) of the chair-isomer of $\text{Ag}_4\text{I}_4\text{L}_4$ and ligand L using TD-CAM-B3LYP (red lines) and PBE0 CD-evGW/BSE (blue lines).



(a) $3A_u$, $\lambda_{\text{calcd}} = 276$ (273) nm

(b) $4A_u$, $\lambda_{\text{calcd}} = 266$ (265) nm

Figure 5.8: Transition density plots and excitation energies for the transitions involved in the TD-CAM-B3LYP absorption band centered at 272 nm (isovalue: $\pm 0.0015a_0^{-3}$, all hydrogen atoms are omitted for clarity). Green represents a gain of electron density whereas orange represents a loss of electron density. The corresponding PBE0 CD-evGW/BSE excitation energies are listed in parentheses for comparison.

ternate corners of a highly distorted cube resulting from steric hindrance among the ligands, which is in good agreement with the X-ray diffraction results. The chair-like isomer can be considered as derived from the cubane-like isomer via cleavage of two Ag–I bonds in one Ag_2I_2 face followed by ca. 180° rotation of an adjacent face, and the driving force is the relief of repulsion between the ligands attached to those two opposite Ag atoms. The UV/Vis spectrum in solution shows a broad absorption band in the range of 300–350 nm, which is excellently reproduced by the GW/BSE calculations on the cubane-like isomer. This is assigned to charge-transfer from metal–halide core to ligand (X+M)LCT by means of transition density plots. For the chair-like isomer, the (X+M)LCT absorption peak appears at around 270 nm, which is slightly blueshifted compared to the cubane-like isomer.

6 Photosensitizers based on heteroleptic copper(I) complexes

6.1 Introduction

The exploitation of solar energy is essential for sustainable development, and the most optimal way is to convert solar energy into chemical energy stored in chemical bonds of molecules, which is the natural photosynthesis. In order to build an artificial photosynthetic system, a photosensitizer (PS) and a catalyst (CAT) are needed, which can be the same in some cases. The molecular photocatalysts developed so far are mainly based on rare precious metal complexes, such as Ru^[88], Re^[89], or Ir^[90]. However, viable renewable energy systems require PS or CAT based on low-cost and earth-abundant materials. Such molecular systems have been designed^[91,92], and remarkably, Cu(I) complexes have been found to be potential alternatives to Ru(II)-polypyridine complexes as photosensitizers for photoredox catalysis.^[93,94] Cu(I) complexes exhibit prominent metal-to-ligand charge-transfer (MLCT) transitions, which often absorb in the visible region at relatively low energy. This property makes them very attractive candidates for developing further photosensitizers. However, on one hand, a specific problem for copper complexes is that they may undergo Jahn–Teller flattening distortion in the excited states, which could lead to undesirable deactivation and lifetime shortening. This can be prevented via the use of sterically bulky ligands, such as chelating diphosphines. On the other hand, some of them are not very stable in the coordinating solvents like acetonitrile due to easy ligand replacements, while stability is an important requirement for the photosensitizer. Recently, a few photosensitizers based on heteroleptic copper(I) complexes of general formula [Cu(NN)(PP)]BF₄ have been reported, where NN and PP are the chelating diimine and diphosphine ligands, respectively.^[95] And in this chapter, more examples of such type will be presented. For all compounds, bis[(2-diphenylphosphino)phenyl] ether (DPEPhos) is used as the bulky ancillary diphosphine ligand, while the chromophoric chelating diimine ligands are different. The diimines all contain a neutral moiety (pyridine or quinoline/quinoxaline derivatives) and a triazole moiety, which can be deprotonated during the coordination reaction.

6.2 Copper(I) complexes with triazole–quinoline/quinoxaline ligands

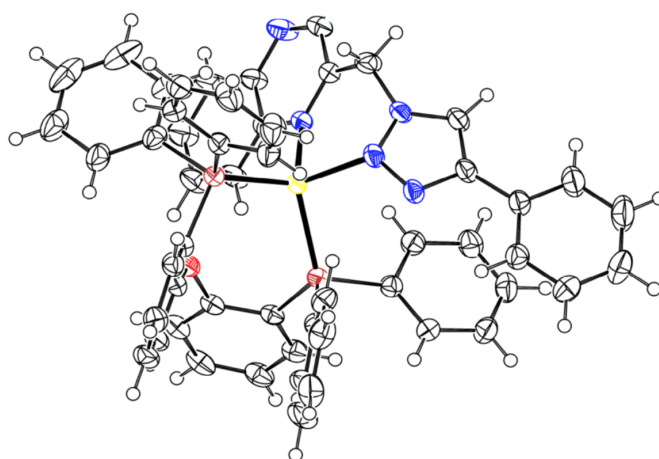
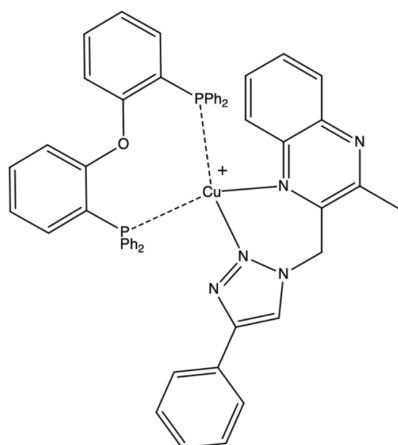
6.2.1 Structural examination and geometry optimization

The structures of the mononuclear copper(I) complexes **1a-c** and the dinuclear species **2** are shown in Figure 6.1. The monomers **1a-c** adopt a distorted tetrahedral geometry with the central copper atom coordinated by one nitrogen atom from the quinoline or quinoxaline ligands and one nitrogen atom from the triazole ligand, and two phosphorous atoms from DPEPhos. The dihedral angles between the Cu(NN) and Cu(PP) planes (**1a**: 78.5°; **1b**: 76.7°; **1c**: 74.3°) manifest the distortion from the idealized tetrahedral geometry. The distances between Cu and N atom of the triazole moiety are very similar in each complex (**1a**: 2.087 Å; **1b**: 2.095 Å; **1c**: 2.059 Å). This is also true for the distances between Cu and N atom of the quinoline/quinoxaline moiety (**1a**: 2.129 Å; **1b**: 2.117 Å; **1c**: 2.139 Å). The Cu–P distances are also similar for the three compounds (**1a**: 2.249 and 2.311 Å; **1b**: 2.256 and 2.299 Å; **1c**: 2.263 and 2.273 Å). The N–Cu–N bite angles (**1a**: 91.1°; **1b**: 89.8°; **1c**: 90.6°) and P–Cu–P bite angles (**1a**: 110.6°; **1b**: 111.7°; **1c**: 113.4°) are similar too.

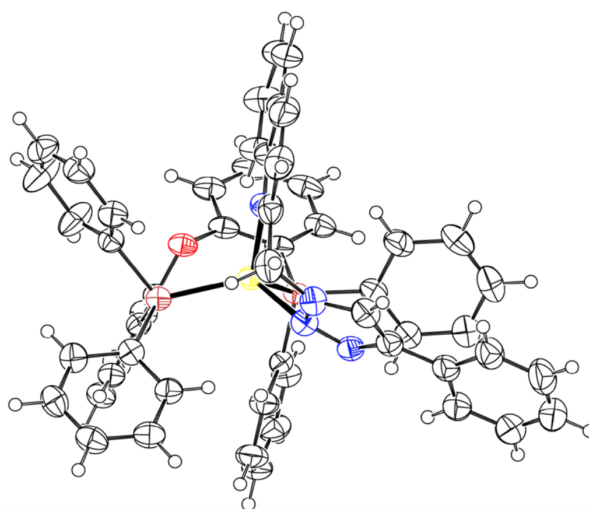
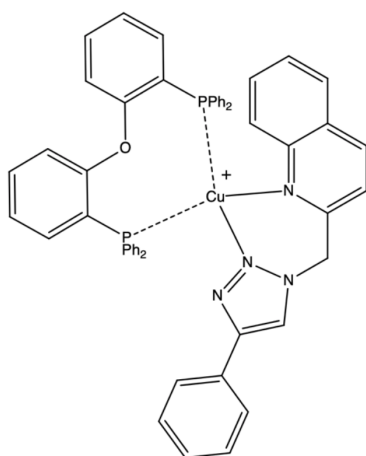
In the quantum chemical calculation, all geometries were optimized at the PBE0-D3(BJ) level of theory. The def2-TZVP basis set was taken for Cu, P, C and N atoms in triazole and quinoline/quinoxaline moieties, and the def2-SV(P) basis set was taken for the rest of the atoms. This combination will be referred to as "TZVP" in further discussions. The ground-state (S_0) geometries of the monomers are in good agreement with the X-ray diffraction analyses, except that the dihedral angles between the Cu(NN) and Cu(PP) planes (**1a**: 85.6°; **1b**: 81.8°; **1c**: 85.9°) are much larger than the experimental values. The Cu–N distances (**1a**: 2.130 and 2.135 Å; **1b**: 2.132 and 2.126 Å; **1c**: 2.105 and 2.126 Å), Cu–P distances (**1a**: 2.257 and 2.316 Å; **1b**: 2.256 and 2.312 Å; **1c**: 2.254 and 2.314 Å), N–Cu–N angles (**1a**: 93.6°; **1b**: 92.9°; **1c**: 93.4°) and P–Cu–P angles (**1a**: 114.4°; **1b**: 114.3°; **1c**: 114.4°) are all similar among the three compounds and agree well with the experiment. The optimized dimer **2** exhibits C_2 symmetry. The dihedral angle between the Cu(NN) and Cu(PP) planes is 82.1°. The Cu–N distances (2.117 and 2.142 Å), Cu–P distances (2.256 and 2.316 Å), N–Cu–N angle (90.0°) and P–Cu–P angle (115.8°) are similar to the corresponding monomer **1a**. The dihedral angle between the two planes formed by Cu and two N atoms of the diimine ligand is 66.4°.

6.2.2 Absorption spectra

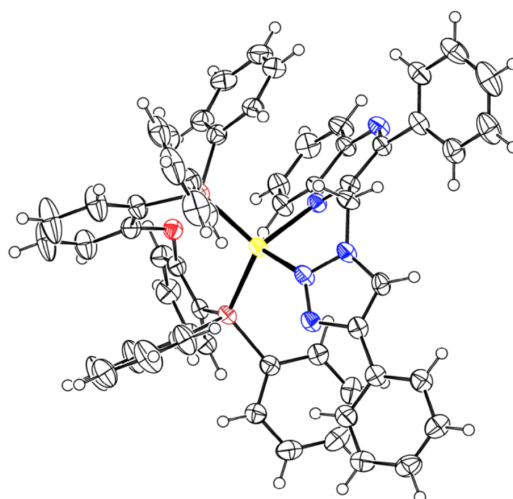
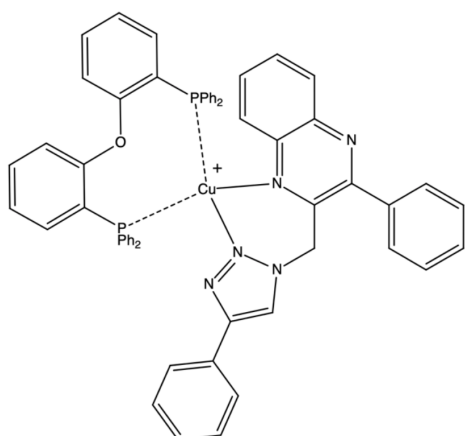
UV/Vis spectra of all the compounds were recorded in spectroscopic dichloromethane (DCM) solutions (Figure 6.2). The absorption spectra of species **1a**, **1c** and **2** are very similar, which is to be expected since they all bear the same quinoxaline ligand. The main difference lies in



1a



1b



1c

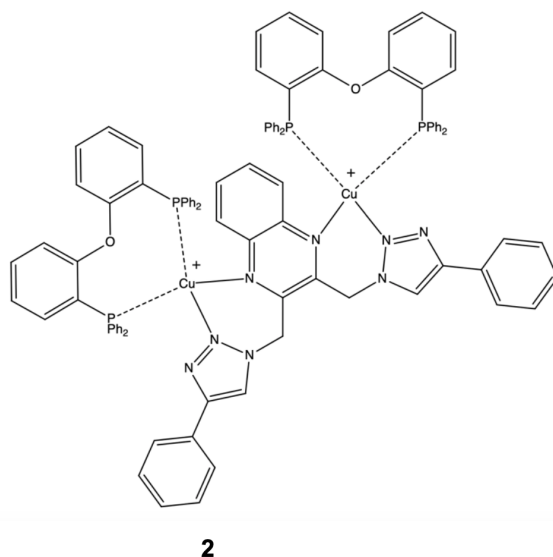


Figure 6.1: Chemical structure and ORTEP drawing of the copper(I) complexes (**1a-c**: mononuclear complexes, **2**: dinuclear complex). Counterions and solvent molecules are omitted for clarity. Crystal structures (not available for **2**) provided by Cecilia Bruschi (IOC), measured and solved by Olaf Fuhr (INT).

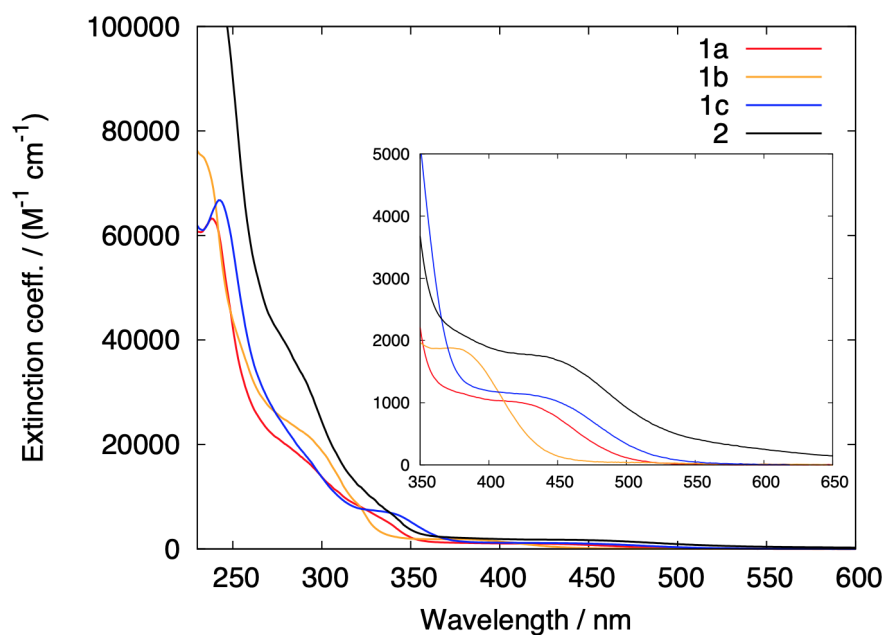
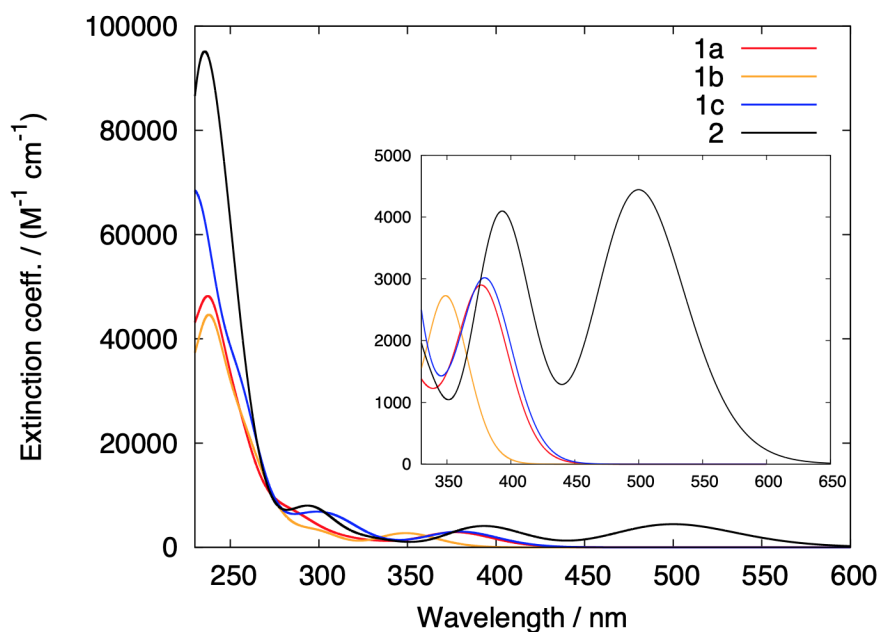
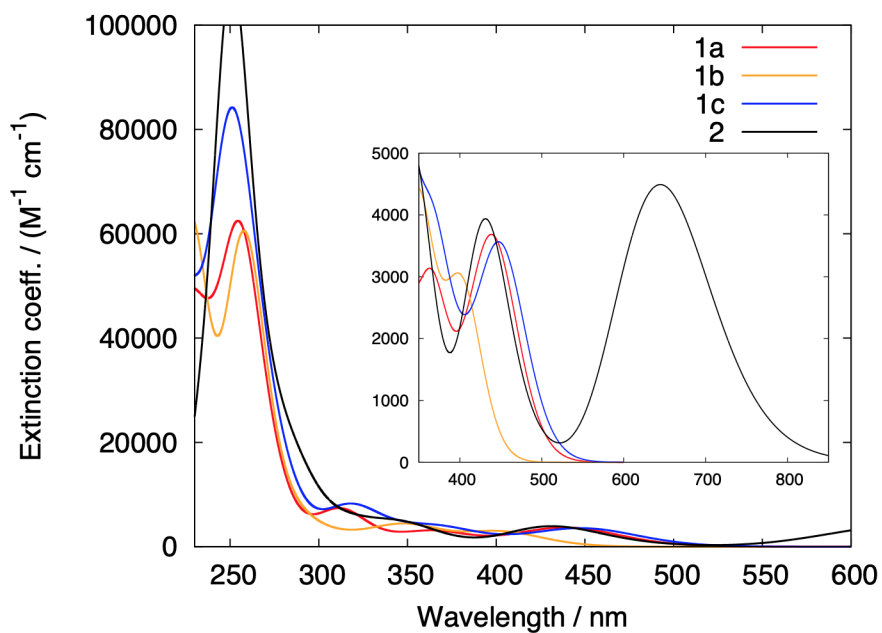


Figure 6.2: Absorption spectra in DCM. Inset: zoom-in in the range of MLCT.

the extinction coefficients, where the dinuclear species **2** almost doubles the values compared to the mononuclear species **1a** and **1c** as it contains two chromophoric units. Besides, **2** shows a prolonged tail at around 600 nm, which is probably due to the cooperativity effect between



(a) TD-CAM-B3LYP/TZVP



(b) PBE0 evGW-BSE/TZVP

Figure 6.3: Absorption spectra (FWHM = 0.4 eV) calculated using (a) TD-CAM-B3LYP/TZVP and (b) PBE0 evGW-BSE/TZVP at the optimized S_0 geometries. Inset: zoom-in in the range of MLCT.

two copper centers. The high-intensity absorption bands in the high-energy UV region (below 300 nm) are assigned to ligand-centered (LC) $\pi \rightarrow \pi^*$ transitions on the chelating diphosphine

ligands. LC transitions centered on the diimine ligands also appear up to 350 nm. The characteristic metal-to-ligand charge-transfer (MLCT) bands occur in the visible region above 400 nm with a shoulder at around 435 nm for **1a**, 455 nm for **1c** and 450 nm for **2**. These MLCT transitions are assigned to charge-transfer from the copper core to the diimine ligand. For complex **1b** that bears a quinoline ligand, its MLCT band is significantly blueshifted compared to the species bearing a quinoxaline ligand, with a shoulder at around 385 nm. This is probably due to one less nitrogen atom in the ring and decreased π conjugation of quinoline compared to quinoxaline.

At the ground-state geometries, the absorption spectra were calculated with TD-CAM-B3LYP and PBE0 CD-evGW/BSE employing TZVP basis set (Figure 6.3). For TD-CAM-B3LYP, the predicted MLCT absorption bands are occurring with relative maxima at 377 nm for **1a**, 349 nm for **1b**, 379 nm for **1c**, 393 and 500 nm for **2**. These transitions are significantly blueshifted by 0.33–0.55 eV compared to the measured spectra, and hence TD-CAM-B3LYP is unsuitable for this class of compounds. For GW/BSE, the MLCT absorption bands are occurring with relative maxima at 438 nm for **1a**, 397 nm for **1b**, 447 nm for **1c**, 431 and 645 nm for **2**, which fit perfectly with the experimental values, only the prolonged tail of complex **2** is slightly redshifted by 0.14 eV.

An NTO analysis confirms the MLCT character of the transitions in the visible region (Figure 6.4). The first absorption band of all four complexes corresponds to charge-transfer from the copper atom to the quinoline/quinoxaline moiety of the diimine ligand, while the triazole moiety is not involved. For complex **1b**, less delocalization of π electrons on quinoline ring can be seen from the particle NTO compared to quinoxaline, which leads to higher energy levels of quinoline π^* orbitals, and hence the absorption is shifted to higher energy. Besides the lowest absorption band at 645 nm, the dinuclear species **2** exhibits one further MLCT transition at 431 nm compared to the monomers. This arises from the communication between the two copper centers.

6.2.3 Structures of the first triplet excited state (T_1)

The tetrahedral geometry of the [Cu(NN)(PP)] core is well retained in the optimized excited states. The dihedral angles between the Cu(NN) and Cu(PP) planes (**1a**: 87.7°; **1b**: 89.7°; **1c**: 87.1°; **1c**: 83.8°) are even closer to the idealized tetrahedral geometry. The increased N–Cu–N bite angles (**1a**: 95.9°; **1b**: 96.6°; **1c**: 95.7°; **2**: 92.2°) and decreased P–Cu–P bite angles (**1a**: 105.6°; **1b**: 106.4°; **1c**: 105.9°; **2**: 109.1°) are also closer to the ideal tetrahedral value of 109.5°.

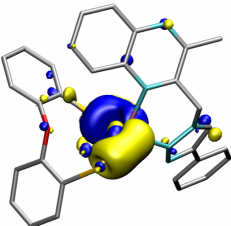
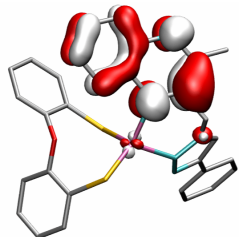
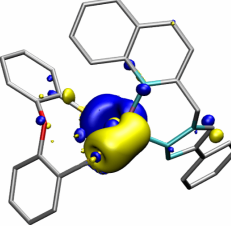
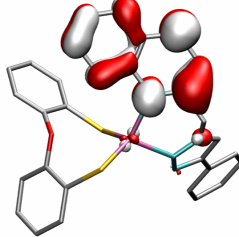
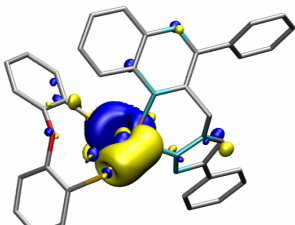
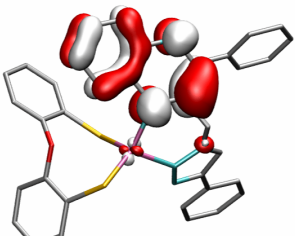
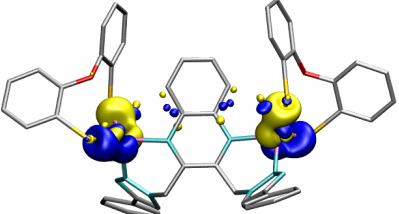
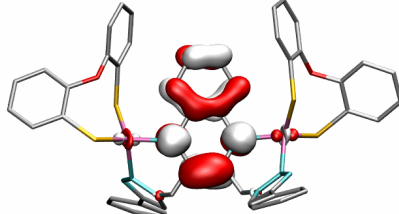
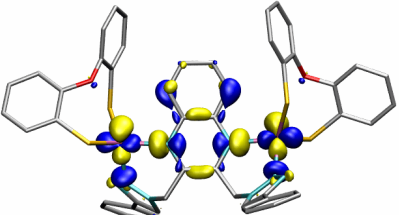
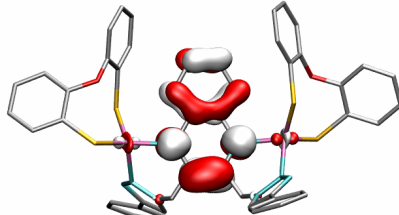
complex	$\lambda_{\text{abs}}/\text{nm}$	hole NTO	particle NTO
1a	443		
1b	403		
1c	452		
2	645		
	431		

Figure 6.4: Dominating occupied (blue/yellow) and virtual (red/white) natural transition orbitals (NTOs, iso-value: $\pm 0.04a_0^{-3/2}$) of the MLCT excitation in the visible region calculated at PBE0 evGW-BSE/TZVP level. Phenyl groups of DPEPhos and all hydrogen atoms are omitted for clarity. Color code: C (silver), N (cyan), O (red), P (yellow), Cu (mauve).

6.3 Copper(I) complexes with triazole–pyridine ligands

6.3.1 Structural examination and geometry optimization

The structures of the four copper(I) complexes bearing triazole and pyridine ligands are shown in Figure 6.5. The dinuclear species **3N** and **3H** are bridged by a *para*-xylene on the triazole moiety and exhibit C_i symmetry. All geometries were optimized at the PBE0-D3(BJ) level of theory. The def2-TZVP basis set was taken for Cu, P, C and N atoms in pyridine, triazole and central benzene ring, and the def2-SV(P) basis set was taken for the rest of the atoms. This combination will again be referred to as "TZVP" in further discussions. In the optimized ground-state (S_0) structures, the dihedral angles between the Cu(NN) and Cu(PP) planes are slightly larger in the neutral species than the protonated species (**1N**: 89.9°; **3N**: 89.8°; **1H**: 87.5°; **3H**: 86.9°). The distances between Cu and N atom of the triazole moiety are slightly shorter in the neutral species (**1N**: 2.018 Å; **3N**: 2.016 Å; **1H**: 2.081 Å; **3H**: 2.089 Å). The distances between Cu and N atom of the pyridine moiety are very similar in each complex (**1N**: 2.089 Å; **3N**: 2.086 Å; **1H**: 2.104 Å; **3H**: 2.111 Å). This is also true for the Cu–P distances (**1N**: 2.218 and 2.284 Å; **3N**: 2.216 and 2.285 Å; **1H**: 2.236 and 2.276 Å; **3H**: 2.240 and 2.276 Å). The N–Cu–N bite angles (**1N**: 80.8°; **3N**: 81.0°; **1H**: 79.7°; **3H**: 79.2°) and P–Cu–P bite angles (**1N**: 113.2°; **3N**: 113.3°; **1H**: 115.3°; **3H**: 115.5°) are similar too. Interestingly, the dihedral angles between the benzene bridging unit and the connected triazole ligand vary between neutral and protonated species (**1N**: 39.9°; **3N**: 40.0°; **1H**: 49.6°; **3H**: 47.2°).

6.3.2 Absorption spectra

At the ground-state geometries, the absorption spectra were calculated with CD-evGW/BSE employing the PBE0 function and TZVP basis set (Figure 6.6). For the protonated species, the absorption band in the visible region with relative maximum at 359 nm (**1H**) and 343 nm (**3H**) corresponds to the characteristic MLCT absorption band. This is also confirmed by an NTO analysis (Figure 6.7). The prolonged tail of **3H** at 402 nm is assigned to a MLCT transition too.

For the neutral species, the first absorption band at 333 nm (**1N**) and 328 nm (**3N**) is mainly centered on the ligand, corresponding to the charge-transfer from the triazole moiety and benzene bridging unit to the pyridine moiety, while the copper atoms are hardly involved.

6.3.3 Rotation of the benzene bridging unit

Theoretically speaking, the central benzene ring in the dinuclear species is expected to be able to rotate freely about the σ bond between the *para* carbon atom and the triazole ligand. As it rotates, the coplanarity of benzene and triazole rings will change accordingly, resulting in

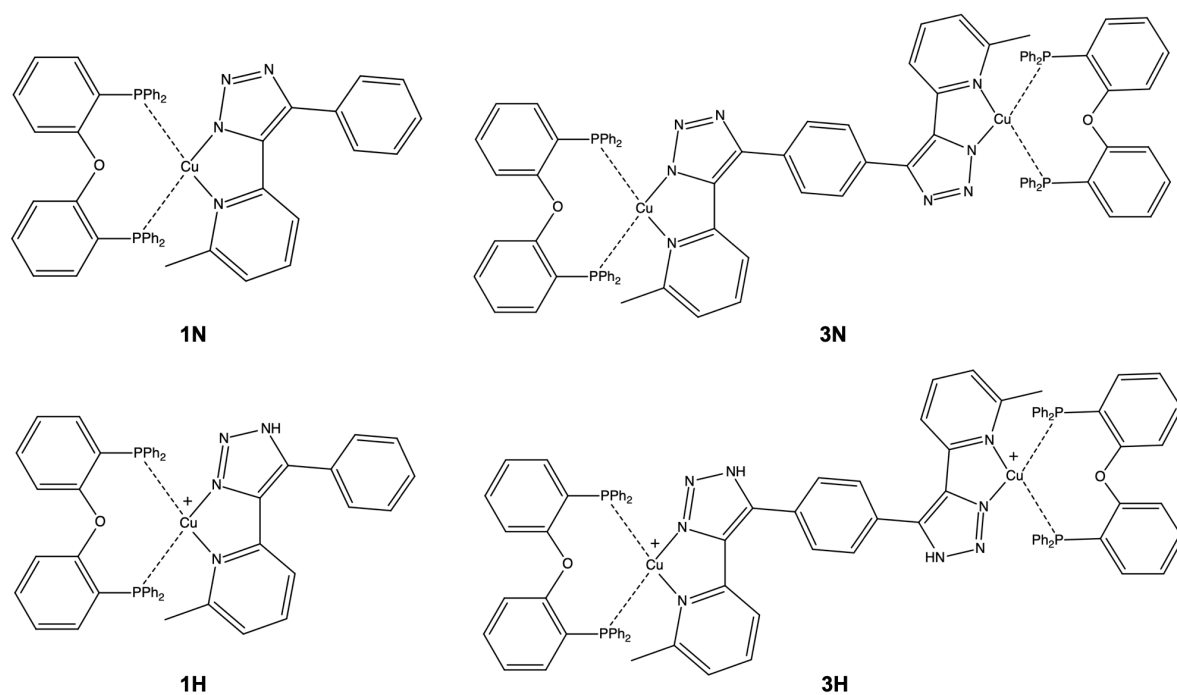


Figure 6.5: Chemical structure of the copper(I) complexes: neutral monomer **1N** and dimer **3N**; protonated monomer **1H** and dimer **3H**.

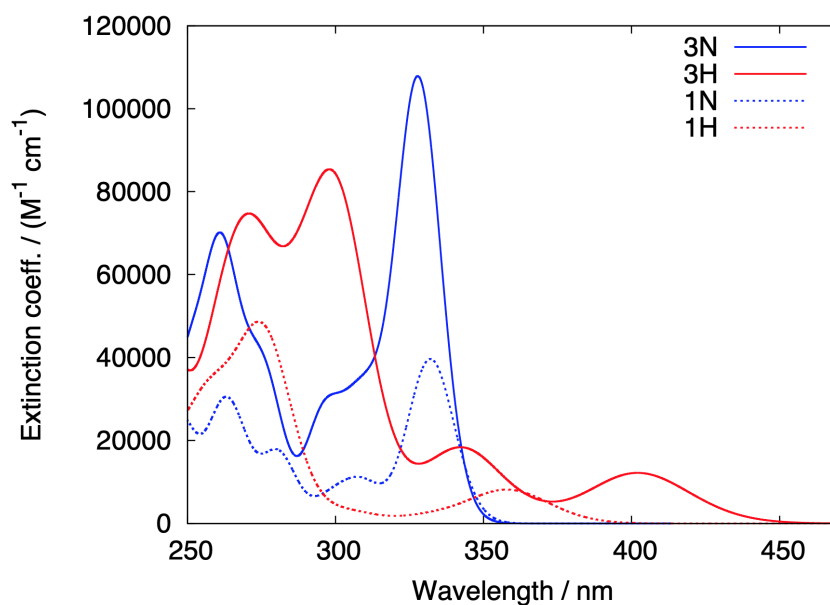


Figure 6.6: Absorption spectra (FWHM = 0.2 eV) calculated using PBE0 evGW-BSE/TZVP at the optimized S_0 geometries.

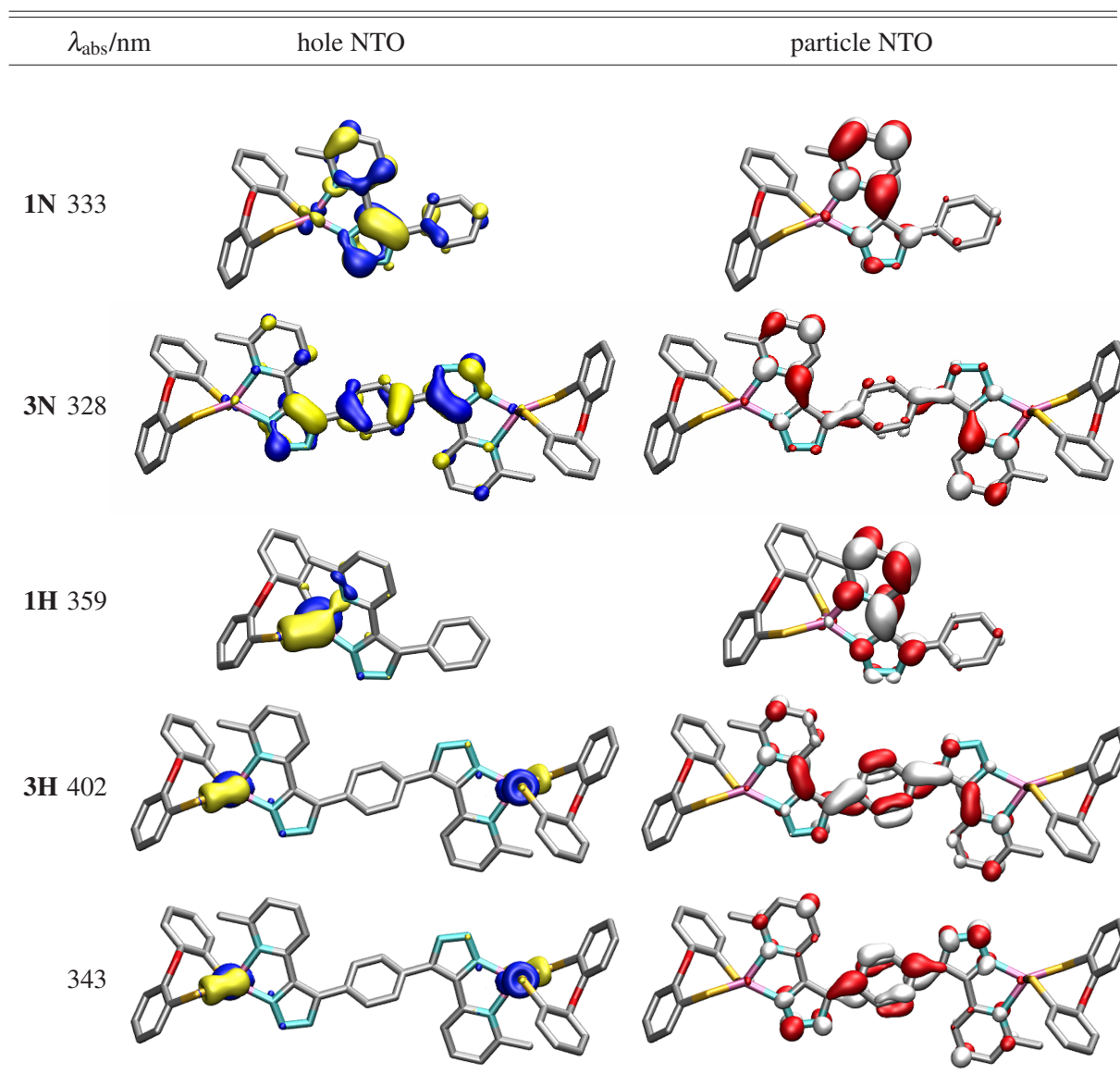


Figure 6.7: Dominating occupied (blue/yellow) and virtual (red/white) natural transition orbitals (NTOs, iso-value: $\pm 0.04a_0^{-3/2}$) of the MLCT excitation in the visible region calculated at PBE0 evGW-BSE/TZVP level. Phenyl groups of DPEPhos and all hydrogen atoms are omitted for clarity. Color code: C (silver), N (cyan), O (red), P (yellow), Cu (mauve).

different extent of π -conjugations. It is interesting to see how the π -electron delocalization as well as the absorption spectra will be affected. Therefore, twelve distinct configurations were obtained by rotating the benzene ring in 3N for every 15 degrees. For each rotation angle, the dihedral angle between benzene and the connected triazole ligand was kept fixed, and the rest of the molecule was optimized. Figure 6.8 shows the change of total energy with respect to the rotation angle. Note that this angle is the rotation angle relative to the equilibrium structure,

not the dihedral angle itself. Since the starting dihedral angle is 40° , as the benzene ring is rotated, it becomes more coplanar with the two triazole ligands, giving rise to larger repulsion and higher total energy. When it is rotated 45° , the three rings are nearly coplanar, and hence the repulsion as well as the total energy reaches a relative maximum. Then the total energy decreases till the benzene is rotated 90° , and increases again to a relative maximum at around 135° before another decline.

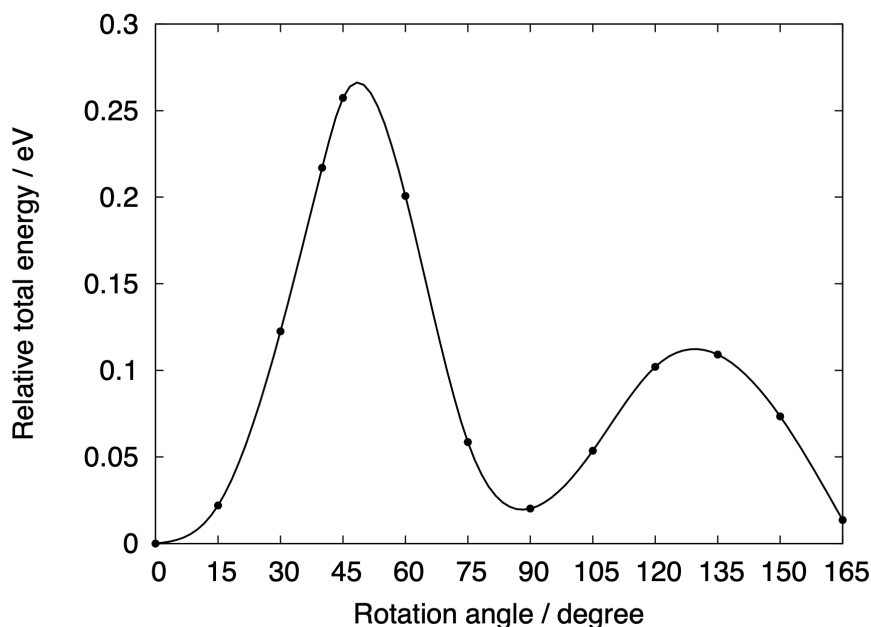


Figure 6.8: Total energy of **3N** with respect to the rotation angle.

At each optimized geometry, the corresponding excitation energies were calculated using PBE0 CD-evGW-BSE/TZVP. Since the HOMO mainly sits at the triazole moiety and benzene bridging unit while the LUMO mainly sits at the pyridine moiety, the HOMO energy changes along with rotation of the benzene ring while the LUMO energy stays nearly the same. The resulting HOMO–LUMO gap displays a sinusoidal trendline with respect to the rotation angle (Figure 6.9). At the rotation angle of 45° , the highly coplanar structure is beneficial for effective π -conjugation, thus improving the charge-transfer properties and resulting in the narrowest π - π^* energy gap. In contrast, at the rotation angle of 135° , the twisted configuration weakens the interaction and reduces the π -conjugation, thus yielding the largest π - π^* energy gap. The energy of the lowest lying singlet excited state (S_1) closely resembles the HOMO–LUMO gap, reflecting the shift of the predicted absorption spectra among different rotation angles.

The transition density plots for selected rotation angles are displayed in Figure 6.10. From 0° to 45° , an enhanced π -conjugation as well as intermolecular π -electron interactions can be

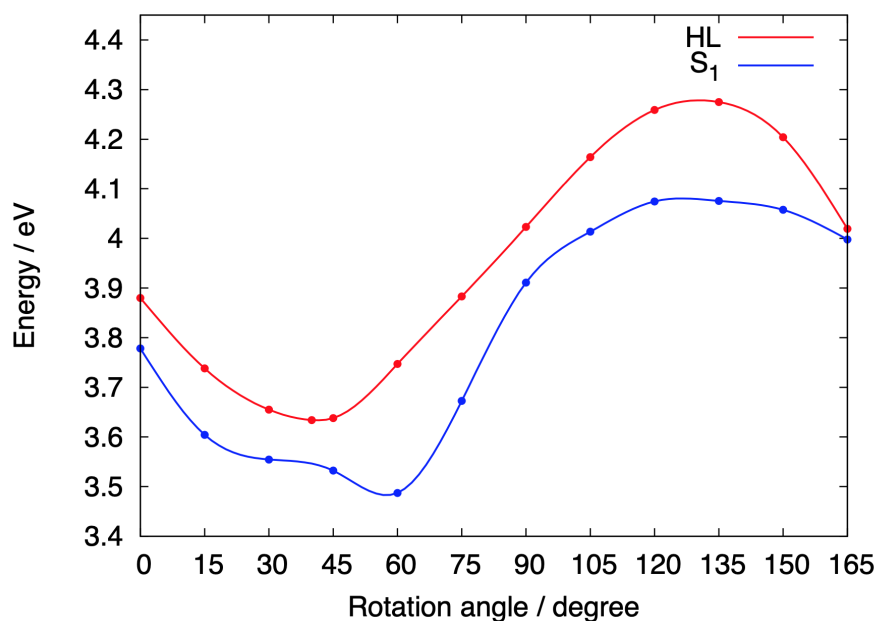


Figure 6.9: HOMO-LUMO gap (HL) and the first singlet excitation energy (S_1) of 3N with respect to the rotation angle.

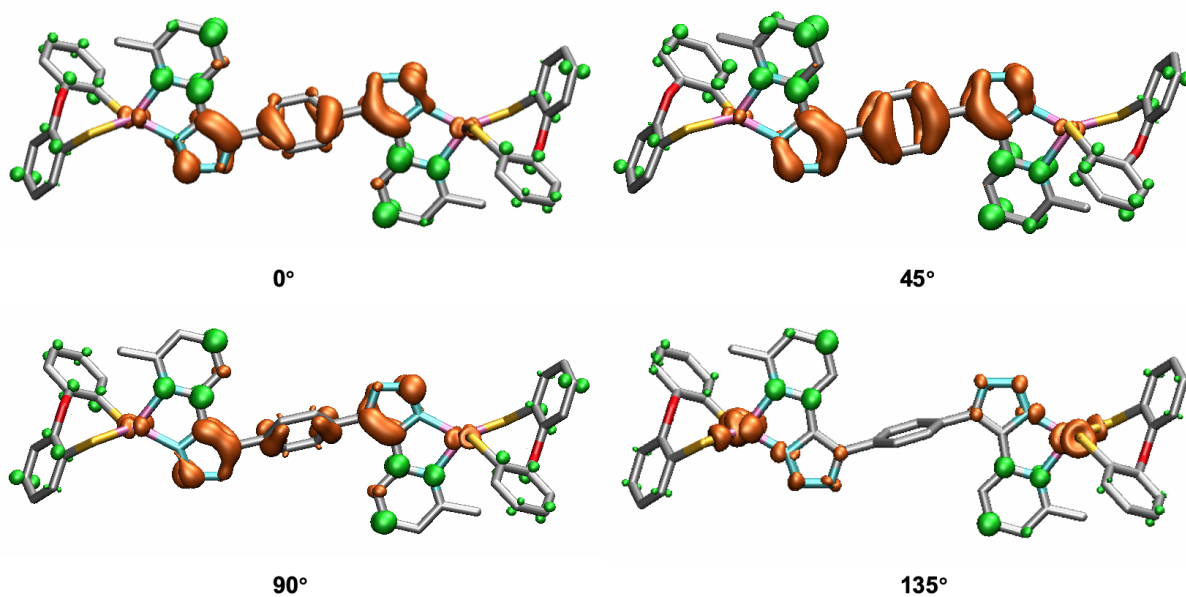


Figure 6.10: Transition density plots of the first absorption peak of 3N at rotation angles of 0° , 45° , 90° and 135° (isovalue: $\pm 0.0015a_0^{-3}$). Phenyl groups of DPEPhos and all hydrogen atoms are omitted for clarity. Green represents a gain of electron density whereas orange represents a loss of electron density.

clearly seen. The electron density is mainly transferred from the benzene and triazole moiety to the pyridine moiety, which benefits from the highly coplanar structure with effective π -conjugation. From 45° to 90° , the π -conjugation is slowly reduced, and further weakened till 135° , where the central benzene ring is completely excluded from the charge-transfer. On the other hand, the metal centers become more and more involved, exhibiting MLCT character of electron density from copper to the pyridine ligands. Then after 135° , the π -conjugation is gradually recovered and the central benzene ring starts to gain back intensity from the metal centers in the charge-transfer process.

To investigate the cooperative effects, the same calculations were performed for the **1N** monomer at different rotation angles. A comparison of the first singlet excitation energy of **1N** and **3N** is given in Figure 6.11. The calculated energies of **1N** closely resemble **3N**, which is as expected since they have the same diimine ligands and thus similar charge-transfer character. Compared to the dimer, the monomer S_1 is slightly higher in the range of 15° – 60° , and slightly lower in the range of 75° – 180° .

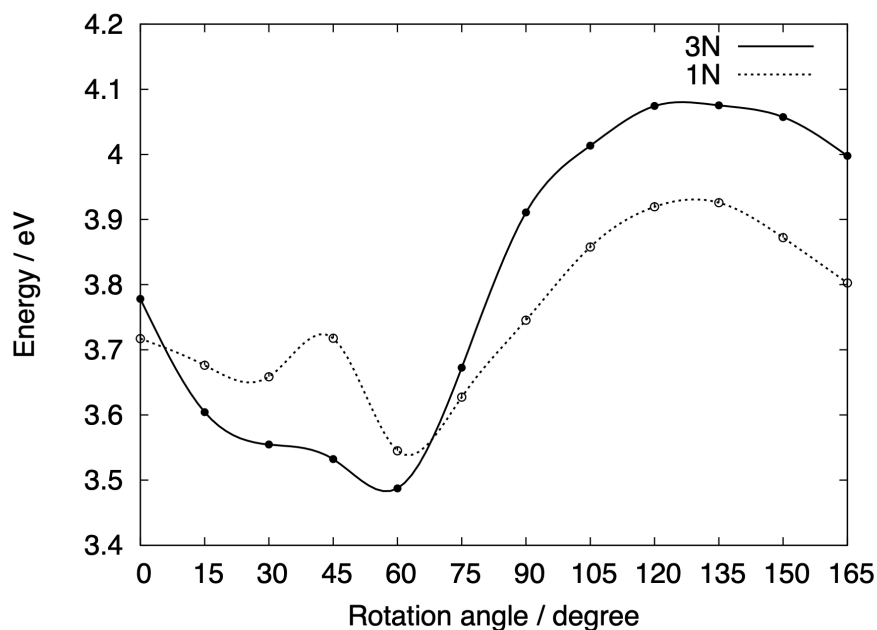


Figure 6.11: The first singlet excitation energy (S_1) of **1N** and **3N** with respect to the rotation angle.

The transition density plots for selected rotation angles are displayed in Figure 6.12. In general, the monomer features less effective π -conjugation due to lack of one triazole unit, and the benzene unit is much less involved in the charge-transfer. On the other hand, the copper atom plays a more crucial role and exhibits stronger MLCT character, and the diphosphine unit is more involved in the charge-transfer. At small rotation angles, where excitations in **3N** are

dominated by the LC transitions, **1N** yields slightly higher S_1 energies due to more pronounced MLCT character. While at large rotation angles, where the MLCT transitions become more important in **3N**, the transfer of electron density to the diphosphine unit in **1N** leads to slightly lower S_1 energies.

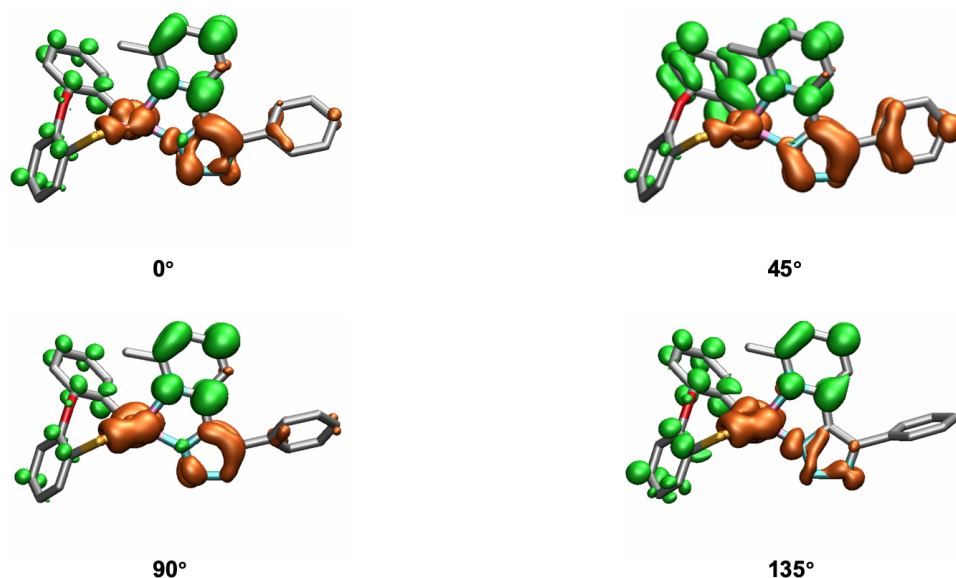


Figure 6.12: Transition density plots of the first absorption peak of **1N** at rotation angles of 0°, 45°, 90° and 135° (isovalue: $\pm 0.0015a_0^{-3}$). Phenyl groups of DPEPhos and all hydrogen atoms are omitted for clarity. Green represents a gain of electron density whereas orange represents a loss of electron density.

6.3.4 Structures of the first triplet excited state (T_1)

Overall, the excited state distortions from the theoretical calculations are very subtle, yet more pronounced for the protonated species than the neutral species. For the neutral species, the calculated dihedral angle between the Cu(NN) and Cu(PP) planes (**1N**: 88.4°; **3N**: 88.5°) only changed by 1° compared to the S_0 state. Hence, there is hardly any distortion in the excited states. On the contrary, the dihedral angles of the protonated species in the T_1 state (**1H**: 77.6°; **3H**: 80.1°) revealed prominent flattening distortions, especially for **1H**, where a distortion of almost 10° was observed. Therefore, the protonation of the triazole ligand yields a significant increase of the flexibility.

6.4 Conclusion

In summary, a series of photosensitizers based on heteroleptic copper(I) complexes with chelating diimine and diphosphine ligands have been investigated. The [Cu(NN)(PP)] core adopts a slightly distorted tetrahedral geometry with the central copper atom coordinated by two nitrogen atoms from the diimine and two phosphorous atoms from the diphosphine. Organometallic photosensitizers employing earth-abundant metals have very promising applications in solar energy conversion, and key to the characterization of their photoresponse is the determination of important experimental and theoretical spectroscopic properties. Complexes with a neutral [Cu(NN)(PP)] core present mainly LC transitions, while complexes with a charged core exhibit prominent MLCT transitions that absorb in the relatively low-energy visible region, and the absorption is further redshifted for the dinuclear species as a result of cooperative effect. Furthermore, the excited state flattening distortions of these copper(I) complexes are rather minor, which is desirable because structural relaxation in the excited state could lead to deactivation and lifetime shortening.

7 Highly luminescent gold(III) pincer complexes

7.1 Introduction

Phosphorescent emitters based on gold(III) are far less studied in the context of phosphorescent organic light-emitting diodes (PhOLEDs) than systems incorporating other heavy metals like iridium(III), ruthenium(II) or platinum(II). However, gold(III) based systems mainly employing a 2,6-diphenylpyridine (C^NC) pincer ligand have attracted dramatically increasing interest.^[96–100] The (C^NC) pincer diminishes radiationless relaxation pathways of excited complexes due to its rigid nature, and in combination with an additional strong donor, e.g. carbenes, alkyl donors or thiolates as second ligand beside the pincer motif, high ligand field splitting is expected, thereby shifting metal centered d-states to higher energies. These metal centered states are regularly seen to be responsible for radiationless relaxation pathways.^[101] Compared to the tetradentate systems, where all coordination sites of the central Au atom are occupied, the tridentate Au(III) complexes are obviously more attractive for further applications in chemical or catalytic transformations.

The pincer's structure can be modified, e.g. by substituting the central pyridine by pyrazine, thereby affecting emission quantum yields and wavelengths.^[102] In fact, the non-palindromic (C^CN) pincer has been shown to exhibit high emission quantum yields, which makes its Au(III) complexes particularly interesting for OLED fabrication.^[103] This was assigned to a higher ligand field splitting of the Au(III) complex compared to the palindromic (C^NC) congener which was investigated by TDDFT.^[101,104] Moreover, the central phenyl donor of the (C^CN) ligand exhibits a stronger *trans* influence than the central pyridine in the (C^NC) ligand, resulting in different complexes reactivity: [(C^CN)Au(III)] based carboxylates favor thermal decarbonylation reactions^[105] whereas the (C^NC) carboxylates show elimination of CO₂^[106].

In this work, two non-palindromic (C^CD) pincer ligands with pyridine (D = N) and imidazolium (D = C') substituents are presented, in combination with phenylacetylene or pentafluorophenyl donors giving rise to four different highly phosphorescent [(C^CD)Au(III)] complexes (Figure 7.1). Their photophysical properties are investigated by the two-component TDDFT and GW/BSE method including spin-orbit coupling, hoping to shed light on the elec-

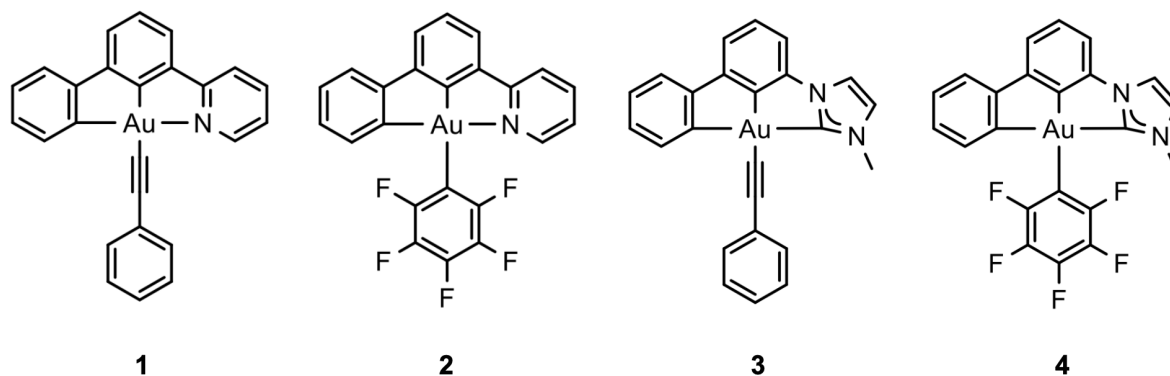


Figure 7.1: Chemical structures of $[(C^{\wedge}C^{\wedge}N)Au(III)CCPh]$ (**1**), $[(C^{\wedge}C^{\wedge}N)Au(III)C_6F_5]$ (**2**), $[(C^{\wedge}C^{\wedge}C')Au(III)CCPh]$ (**3**) and $[(C^{\wedge}C^{\wedge}C')Au(III)C_6F_5]$ (**4**).

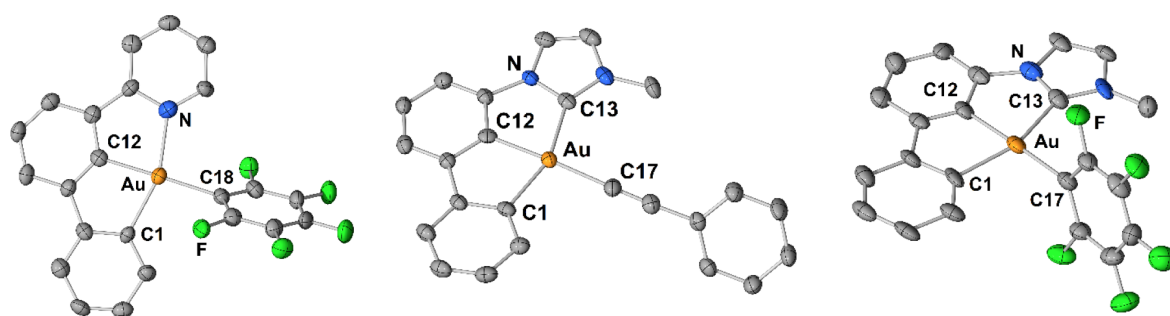


Figure 7.2: Solid state molecular structure of $[(C^{\wedge}C^{\wedge}D)Au(III)]$ complexes **2** (left), **3** (middle) and **4** (right). Hydrogen atoms are omitted for clarity. Reprinted with permission from Ref. 107. Copyright 2020 John Wiley & Sons.

tronic influence of the non-palindromic pincer ligand and reveal non-radiative relaxation pathways accompanied with the different ligands employed.

7.2 Geometry optimization

All geometries were optimized at the PBE0-D3(BJ)/def2-TZVP level of theory. The ground-state (S_0) geometries are in good agreement with the X-ray diffraction analyses (Figure 7.2). All complexes adopt structures with tilted orientation of the aryl entities of the ancillary ligands, i.e. they are not aligned coplanar with the pincer moiety, but tilted against the pincer's plane in a near perpendicular manner. This preference for the tilted arrangement is important with respect to the interpretation of photophysical properties. The $[(C^{\wedge}C^{\wedge}D)Au(III)]$ motif belongs to the C_s point group. Therefore, the $\pi_{CCD} \rightarrow \pi_{CCD}^*$ *intra*-ligand transitions (IL) are of A' symmetry and thus dipole allowed, while the $\pi_{ethinyl} \rightarrow \pi_{CCD}^*$ *inter*-ligand transitions (LL'CT) depends on

the orientation of the aryl entity. In a coplanar arrangement, LL'CT is of A' symmetry and thus dipole allowed; a tilted arrangement changes it to A'' , which is dipole allowed in one direction. The transition intensities are strongly affected by these symmetry properties, and hence are important for a sound discussion of photophysics.

7.3 Excited state calculations at the S_0 geometry

In the experimentally measured spectra (Figure 7.3), the $(C^{\wedge}C^{\wedge}C')$ complexes **3** and **4** exhibit further blueshifted absorptions compared to the $(C^{\wedge}C^{\wedge}N)$ congeners **1** and **2**. This is due to the higher energy levels of imidazole π^* orbitals as well as the higher-lying gold centered d-orbitals caused by stronger ligand field splitting, which clearly shows the electron rich nature of Au(III) in the presence of the $(C^{\wedge}C^{\wedge}C')$ pincer. The vibronically structured bands between 330 nm and 280 nm with peak distances between 1200 cm^{-1} and 1400 cm^{-1} are typical for the pincer's ligand breathing mode, which probably arise from $\pi \rightarrow \pi^*$ IL transitions. The possibility can be ruled out that LL'CT transitions are responsible for the first absorption bands, since the absorption profiles of complexes **1** and **2** do not obviously differ.

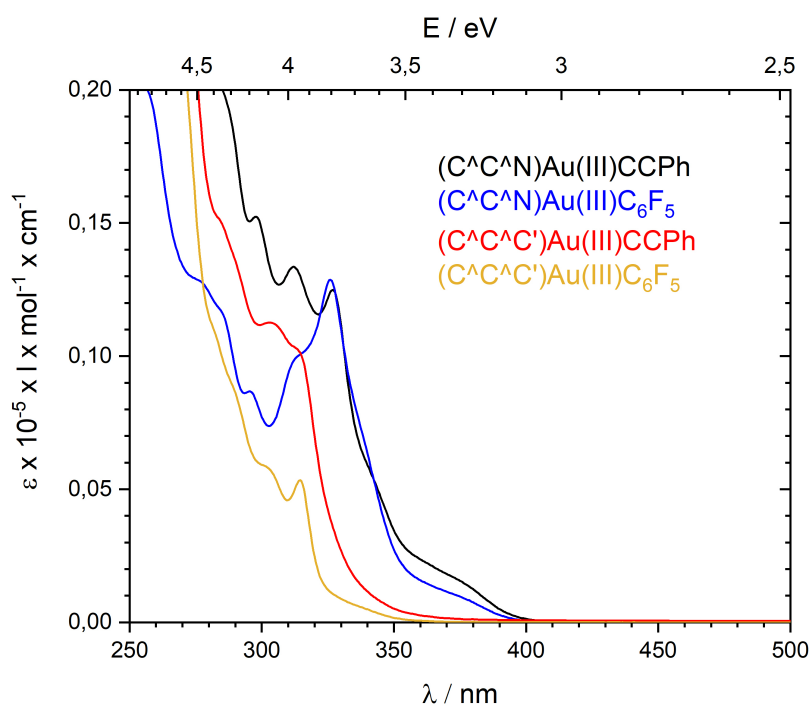


Figure 7.3: Experimental UV/Vis spectra of complexes **1**, **2**, **3** and **4**. Reprinted with permission from Ref. 107. Copyright 2020 John Wiley & Sons.

At the ground-state geometries, the absorption spectra were calculated with TDDFT and CD-evGW/BSE employing the PBE0 or CAM-B3LYP functional and def2-TZVP basis set. Overall, the predicted spectra (Figures 7.4 and 7.5) agree well with the experiment.

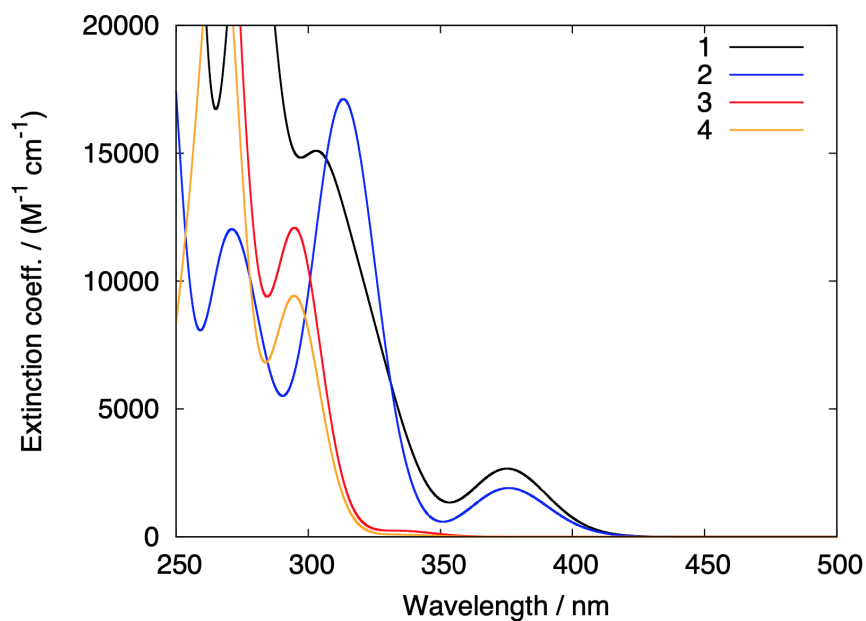
For TD-PBE0 (Figure 7.4a), a blueshift of approximately 0.15 eV and 0.25 eV is observed for complexes **1/2** and **3/4**, respectively. For evGW/BSE (Figure 7.5), a blueshift of approximately 0.25 eV and 0.3 eV is observed for complexes **1/2** and **3/4**, respectively. These are all within the accuracy range of the methods. However, TD-CAM-B3LYP failed to reproduce the experiment values, and the predicted spectra (Figure 7.4b) are significantly too much blueshifted, especially for complexes **3/4**, a blueshift of approximately 0.55 eV is observed. Hence, the CAM-B3LYP functional is not suitable for this class of complexes. The prolonged tail in the absorption spectra of the (C[^]C[^]N) complexes **1** and **2** is dominated by a $\pi \rightarrow \pi^*$ IL transition located at the pincer ligand (Figure 7.6).

7.4 Two-component excited state calculations at the T₁ geometry

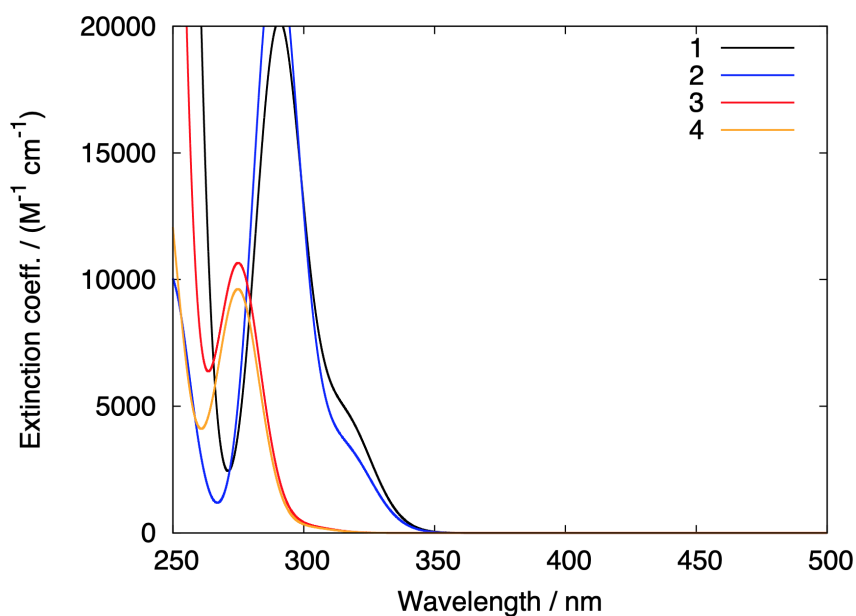
The investigated complexes show intense luminescence in solution at room temperature with emission lifetimes in the micro- and sub-microsecond region indicating phosphorescence. All complexes share very similar emission pattern (Figure 7.7), which is rather astonishing given that the absorption spectra are quite different. This can only be due to the fact that all these complexes have a triplet excitation at around the same energy, from which vibronic transitions generate the phosphorescence spectroscopy. Indeed, the vibronic structure with band distances of about 1300 cm⁻¹ indicates pincer $\pi \leftarrow \pi^*$ centered transitions. This is further confirmed by the lifetimes (Table 7.1) that are of the same order of magnitude. The emission wavelengths of the (C[^]C[^]C[']) complexes **3** and **4** are negligibly shifted to higher energies, and the PhCC or C₆F₅ ligands have no impact on the emission profile. Thus, the transition is detached from these ligands.

Table 7.1: Photophysical data of gold complexes in dichloromethane at 293 K.

complex	$\lambda_{\text{abs}}/\text{nm}$	$\lambda_{\text{em}}/\text{nm}$	Φ	$\tau/\mu\text{s}$
1	298, 312, 327, 376	473, 507, 543, 588	0.03	0.8
2	295, 314, 326, 370	475, 510, 546, 589	0.09	4.1
3	303, 314	471, 505, 540, 581	0.03	1.0
4	302, 314	470, 504, 539, 582	0.10	0.5



(a)



(b)

Figure 7.4: Absorption spectra (FWHM = 0.3 eV) of complexes 1, 2, 3 and 4 calculated using TDDFT/def2-TZVP with (a) PBE0 or (b) CAM-B3LYP functional at the optimized S₀ geometries.

Emission quantum yields Φ in dichloromethane solution at room temperature range between 3% and 10% (Table 7.1), which are higher than the yields of many palindromic analogues^[108].

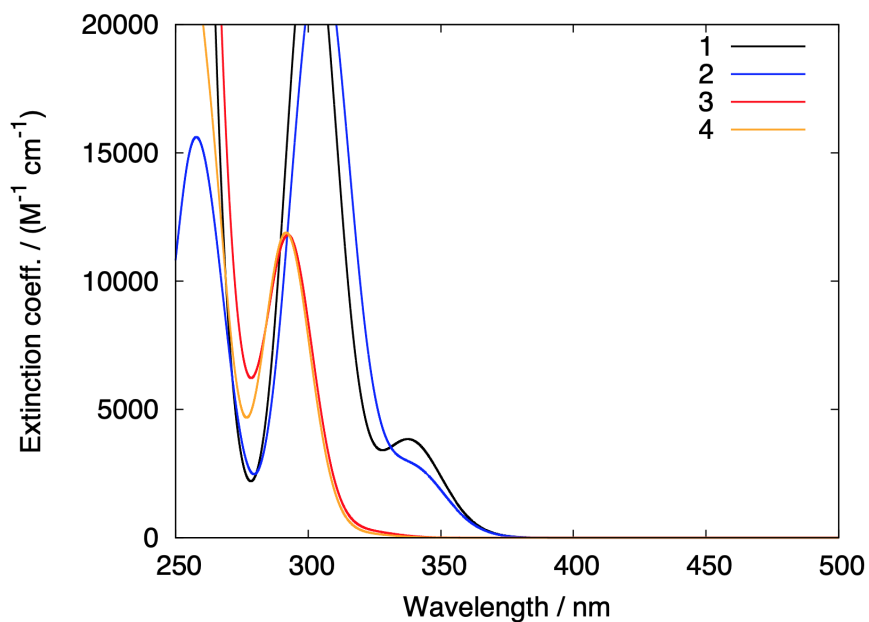


Figure 7.5: Absorption spectra (FWHM = 0.3 eV) of complexes **1**, **2**, **3** and **4** calculated using PBE0 evGW-BSE/def2-TZVP at the optimized S_0 geometries.

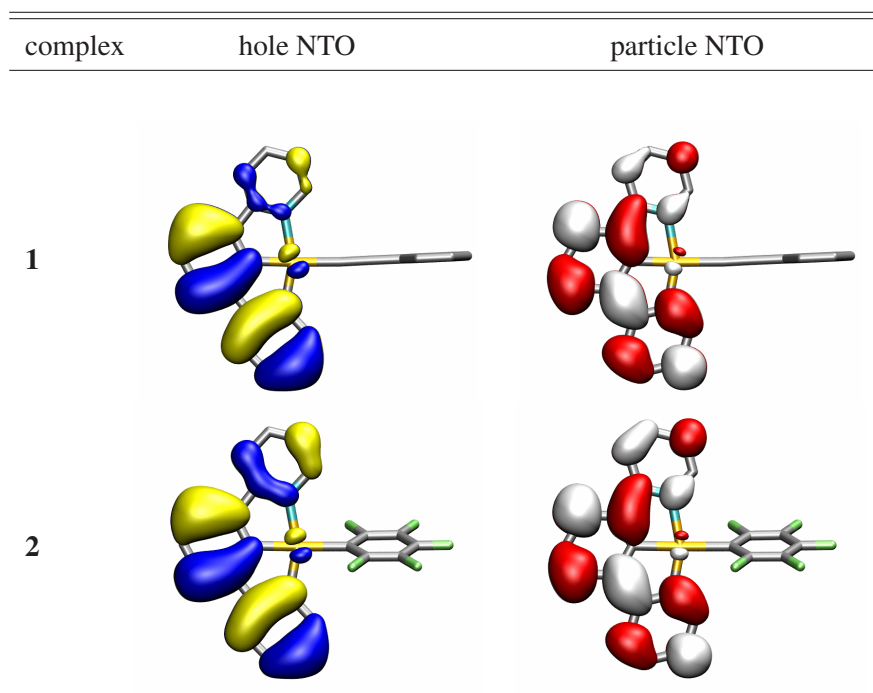


Figure 7.6: Dominating occupied (blue/yellow) and virtual (red/white) natural transition orbitals (NTOs, iso-value: $\pm 0.02a_0^{-3/2}$) of the lowest singlet excitation calculated at PBE0 evGW-BSE/def2-TZVP level. Hydrogen atoms are omitted for clarity.

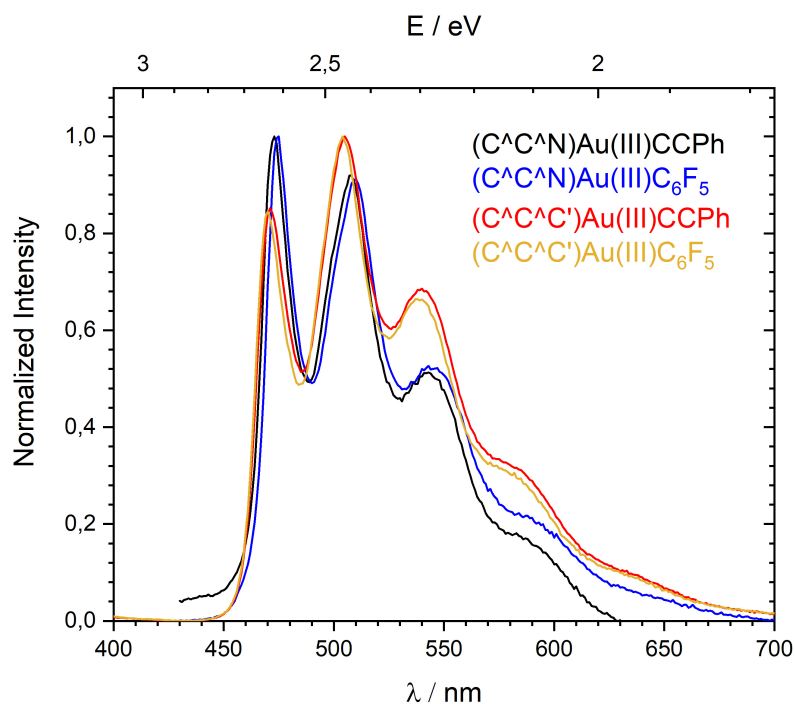


Figure 7.7: Experimental emission spectra in solution of complexes **1**, **2**, **3** and **4**. Reprinted with permission from Ref. 107. Copyright 2020 John Wiley & Sons.

Obviously, the quantum yields are not affected by the pincer motif but the adjacent ligand, since the C_6F_5 substituted systems **2** and **4** phosphoresce up to three times more efficient than the PhCC analogues **1** and **3**. This is especially noteworthy, since the opposite finding was reported for the luminescence of cyclometalated $[(C^A^N)Au(III)]^{[109]}$ and $[(C^A^C')Au(III)]^{[110]}$ complexes, where higher emission quantum yields were found for phenylethynyl substituted complexes than for pentafluorophenyl substituted ones. This may be understood from the weaker donor strength of (per)fluorinated aryl ligands resulting in smaller ligand field splitting of the gold(III) atom, while in contrast, the PhCC ligand is a sufficiently strong donor to enable phosphorescence. Obviously, the non-palindromic pincer motifs in the present study overcompensate the weaker ligand-field splitting, i.e. the ligand-field splitting of **2** and **4** is strong enough despite the weak pentafluorophenyl donor. However, this does not explain why the pentafluorophenyl substituted complexes outperform the phenylethynyl substituted ones regarding phosphorescence quantum yields.

To gain more insight into the mechanism of phosphorescence, two-component (2c) TDDFT and evGW/BSE calculations using the PBE0 functional and dhf-TZVP-2c basis set were performed. At the optimized first triplet excited state (T_1), TDDFT predicts the shift of the emission lines for all four complexes to nearly the same value with calculated $0 \leftarrow 0$ triplet emission

Table 7.2: First triplet excitation T_1 and most intense triplet excitation T_{int} in the energetic range between S_1 and T_1 for gold complexes at the optimized T_1 geometries. Excitation energies of triplets are given at their center of mass. Oscillator strengths f and electric dipole radiative lifetime τ are taken from the most intense component.

(a)				
2c TD-PBE0	1	2	3	4
$T_1/\text{eV (nm)}$	2.02 (615)	2.02 (613)	1.93 (641)	1.92 (645)
$f_1/\text{a.u.}$	3.132×10^{-6}	2.637×10^{-6}	7.189×10^{-6}	4.991×10^{-6}
$\tau_1/\mu\text{s}$	1809	2139	858	1249
$T_{\text{int}}/\text{eV (nm)}$	2.81 (441)	2.81 (441)	3.06 (405)	3.05 (406)
$f_{\text{int}}/\text{a.u.}$	7.599×10^{-4}	4.132×10^{-4}	3.448×10^{-4}	1.519×10^{-4}
$\tau_{\text{int}}/\mu\text{s}$	3.8	7.1	7.1	16.3
(b)				
2c evGW/BSE	1	2	3	4
$T_1/\text{eV (nm)}$	2.56 (484)	2.48 (499)	2.35 (528)	2.32 (535)
$f_1/\text{a.u.}$	1.183×10^{-8}	7.561×10^{-8}	1.382×10^{-5}	7.474×10^{-6}
$\tau_1/\mu\text{s}$	297192	49423	303	574
$T_{\text{int}}/\text{eV (nm)}$	3.27 (379)	3.08 (403)	3.33 (373)	3.29 (377)
$f_{\text{int}}/\text{a.u.}$	4.626×10^{-3}	4.216×10^{-4}	6.377×10^{-5}	7.402×10^{-5}
$\tau_{\text{int}}/\mu\text{s}$	0.5	5.8	32.6	28.8

energies of 615 nm/2.02 eV (**1**), 613 nm/2.02 eV (**2**), 641 nm/1.93 eV (**3**) and 645 nm/1.92 eV (**4**), respectively (Table 7.2a). This is in close resemblance of experimental findings of nearly identical phosphorescence spectra for all complexes. The evGW/BSE emission energies are further blueshifted and fail to predict the position of the peaks well (Table 7.2b). However, predicted oscillator strengths and transition probabilities of the singlet–triplet excitations are underestimated within the TDDFT framework and improved within the GW/BSE scheme. The evGW/BSE lifetimes roughly resemble the trend of the experimentally observed lifetimes in Table 7.1, though in terms of absolute values, differences of up to an order of magnitude remain for complexes **3** and **4**. An NTO analysis reveals that both T_1 excitations listed in Table 7.2a and Table 7.2b are pure *intra*-ligand (IL) excitations, as described previously. And the π orbital of the emissive $\pi \leftarrow \pi^*$ ^3IL state is almost exclusively centered at the (bi)phenyl unit of the respective pincer ligand (Figure 7.8).

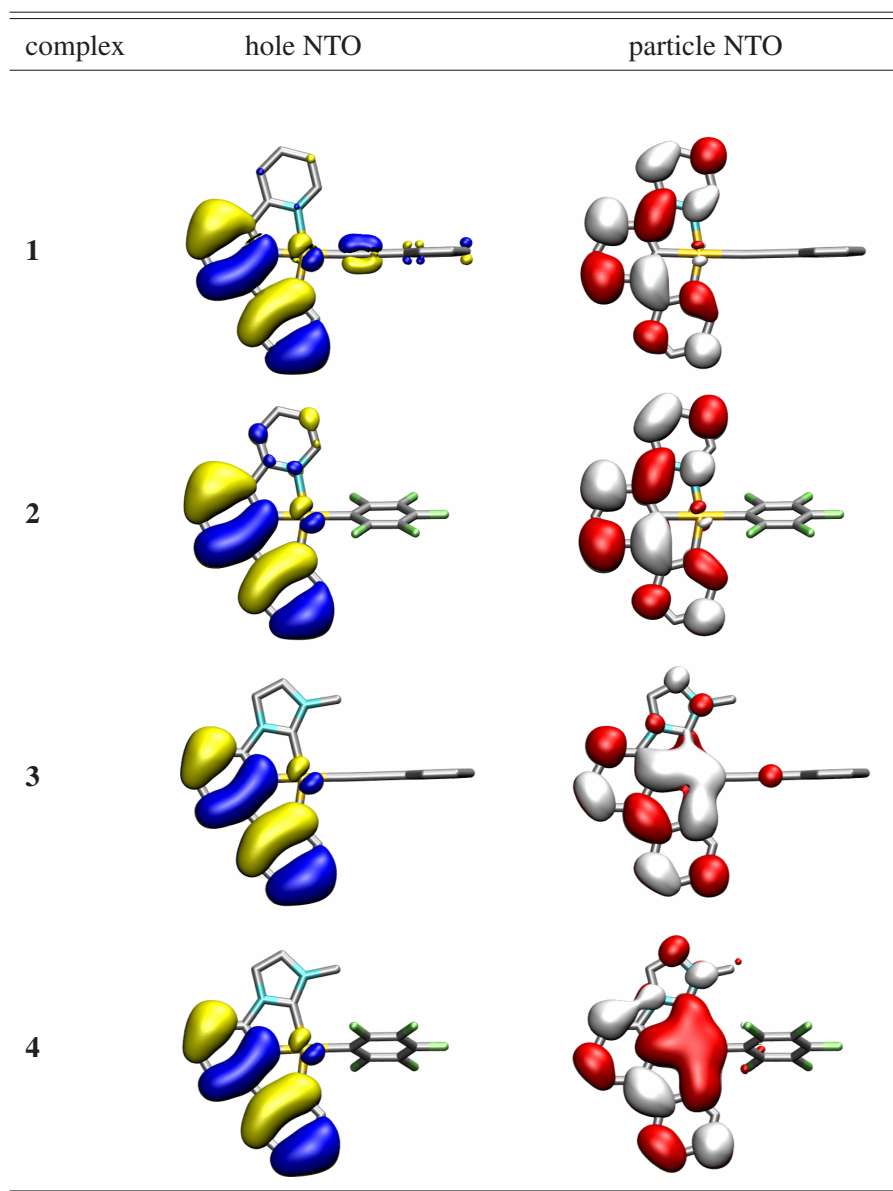


Figure 7.8: Dominating occupied (blue/yellow) and virtual (red/white) natural transition orbitals (NTOs, iso-value: $\pm 0.02a_0^{-3/2}$) of the lowest triplet excitation calculated at PBE0 evGW-BSE/def2-TZVP level. Hydrogen atoms are omitted for clarity.

Even though there is good agreement between the predicted and observed spectra, the quantum yield needs further investigation, as the difference between the PhCC and C_6F_5 -ligated systems cannot be explained by the emission spectra alone. A main difference between these complexes is given by their ability to rotate about the Au-C axis. For the phenylethynyl complexes **1** and **3**, rotational barriers of only 0.8 kJ/mol and 1.5 kJ/mol were obtained, and thus a rapid rotation of the ligand at room temperature is assumed. However, due to steric hindrance, no rotation is observed for the bulkier pentafluorophenyl ligand, and a stable transition-state

geometry could not be located. In the nearly coplanar transition-state geometry of complexes **1** and **3**, the first triplet excited state changes its character from *intra-* (IL) to *inter-*ligand charge-transfer (LL'CT, Figure 7.9), which allows for an efficient pathway to release the excess energy of the excited state, suppressing the phosphorescence of complexes **1** and **3**. This is also confirmed by the higher oscillator strengths and shorter radiative lifetimes as shown in Table 7.4. In the tilted geometry, this LL'CT state is also present, but only as a higher-lying excited state. Therefore, for the bulkier C₆F₅ ligand, this non-radiative relaxation pathway is closed as the overlap between the π systems is never sufficiently high at any reasonable geometry to yield a significant transition dipole moment.

Table 7.4: First triplet excitation T₁ and most intense triplet excitation T_{int} in the energetic range between S₁ and T₁ for gold complexes at the optimized transition-state (TS) geometries. Excitation energies of triplets are given at their center of mass. Oscillator strengths f and electric dipole radiative lifetime τ are taken from the most intense component.

	2c TD-PBE0		2c evGW/BSE	
	1	3	1	3
T ₁ /eV (nm)	2.22 (557)	1.93 (641)	2.70 (460)	2.35 (527)
f ₁ /a.u.	3.271 × 10 ⁻⁵	9.793 × 10 ⁻⁶	1.168 × 10 ⁻⁷	2.332 × 10 ⁻⁵
$\tau_1/\mu\text{s}$	142	630	27167	179
T _{int} /eV (nm)	2.83 (438)	3.05 (406)	3.30 (375)	3.42 (363)
f _{int} /a.u.	4.250 × 10 ⁻³	4.315 × 10 ⁻³	9.939 × 10 ⁻⁴	2.828 × 10 ⁻⁴
$\tau_{\text{int}}/\mu\text{s}$	0.7	0.6	2.1	7.0

Hence, an unhindered rotating π system suppresses phosphorescence. But even for the PhCC complexes, the overall transition probability is still not high in the coplanar configuration, explaining why only diminished emission quantum yields are observed instead of full quenching. The difference between magnitudes of transition dipole moment for tilted (LL'CT: A'') and coplanar geometry (LL'CT: A') nicely corresponds to a qualitative picture based on group theory considerations.

7.5 Conclusion

In summary, the photophysical properties of four different highly phosphorescent gold(III) pincer complexes were investigated by one- and two-component TDDFT and GW/BSE calculations. The non-palindromic (C[^]C[^]D) pincer motifs with pyridine (D = N) and imidazolium (D

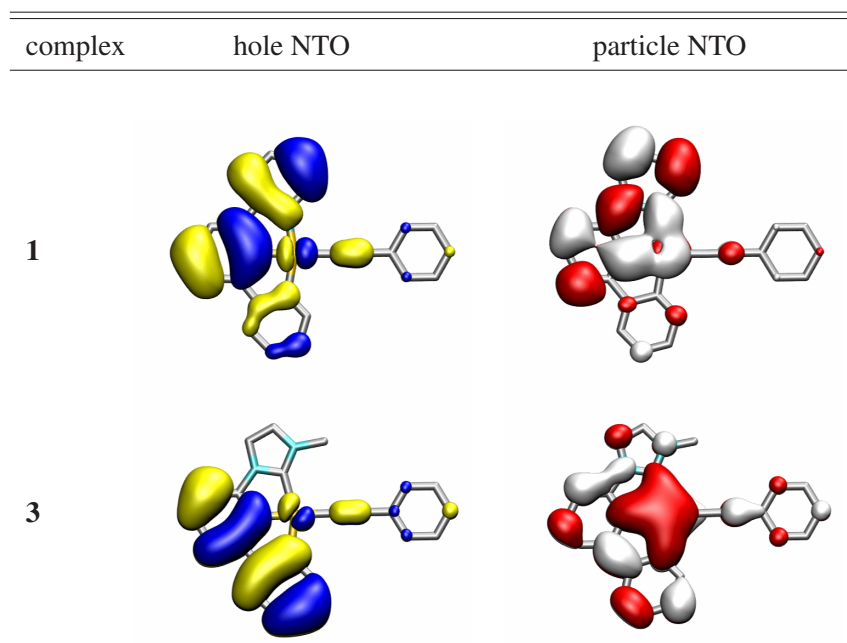


Figure 7.9: Dominating occupied (blue/yellow) and virtual (red/white) natural transition orbitals (NTOs, iso-value: $\pm 0.02a_0^{-3/2}$) of the lowest triplet excitation of the coplanar transition state calculated at PBE0 evGW-BSE/def2-TZVP level. Hydrogen atoms are omitted for clarity.

= C') substituents have shown outstanding electronic properties compared to the palindromic (C[^]N[^]C) congeners. A strong ligand field splitting is reflected in blue shifted absorptions and high emission quantum yields in solution at room temperature. Interestingly, the tilted phenylacetylene or pentafluorophenyl ligands have almost no effect on either the absorption or the emission profiles. However, they do affect the quantum yields, and the C₆F₅ substituted systems phosphoresce more efficiently than the PhCC analogues. This is nicely explained by the non-radiative relaxation pathways via a coplanar transition state, which is also supported by the group theory considerations. Thus, the quantum chemical calculations successfully clarify the electronic influence of the non-palindromic pincer ligand and the non-radiative relaxation pathways of the phenylacetylene ligand. And the combined experimental and theoretical results provide a basis for further investigations on systematically tuning the chemical and photophysical properties of the pincer complexes with different functional groups in the pincer moieties.

8 Bimetallic gold(I) amidinate complexes as model systems for investigation of photophysical properties

8.1 Introduction

The most prominent metallophilic interaction is the interaction between gold atoms, which has been coined as aurophilicity. The strength of aurophilic interactions correlates with the intermetallic distance, and the cooperative effects are important for the luminescence properties. On the other hand, the correlation between the luminescence and the arrangement of the metal atoms is not yet fully understood due to limitations of theoretical methods, synthesis procedure and spectroscopic experiment. Therefore, it makes sense to first build up a series of simple model bimetallic gold complexes with aurophilic interaction, followed by a systematic investigation of the luminescence properties in both gas phase and solid state. Within this library, ligands that can be easily altered in terms of their electronic and steric properties will be used. Hence, by slightly modifying the substituent of the ligand, the effects of the ligand on the photophysical properties can be studied in a systematic way.

Amidates are good candidates as anionic bridging ligands for this purpose, since the substituents on the nitrogen atoms as well as on the ligand backbones can be varied in a wide range with moderate synthetic work. The amidinate ligands coordinate to Au(I) ions in a bridging mode and bring the metal ions close together, giving rise to short Au...Au distances. The two gold atoms are coplanar with the central carbon and two nitrogen atoms of both amidinate ligands (Figure 8.1). By introducing aromatic groups with electron donating and withdrawing substituents in *para* position, the electronic influence of the ligand on the photophysical properties can be investigated. And by introducing aromatic groups with bulky substituents in *ortho* position, the steric demand of the amidinate can be varied. By combining the synthesis, the spectroscopic data and the quantum chemical calculation results, it is hoped to push the understanding of the influence of aurophilic interaction on the luminescence properties further.

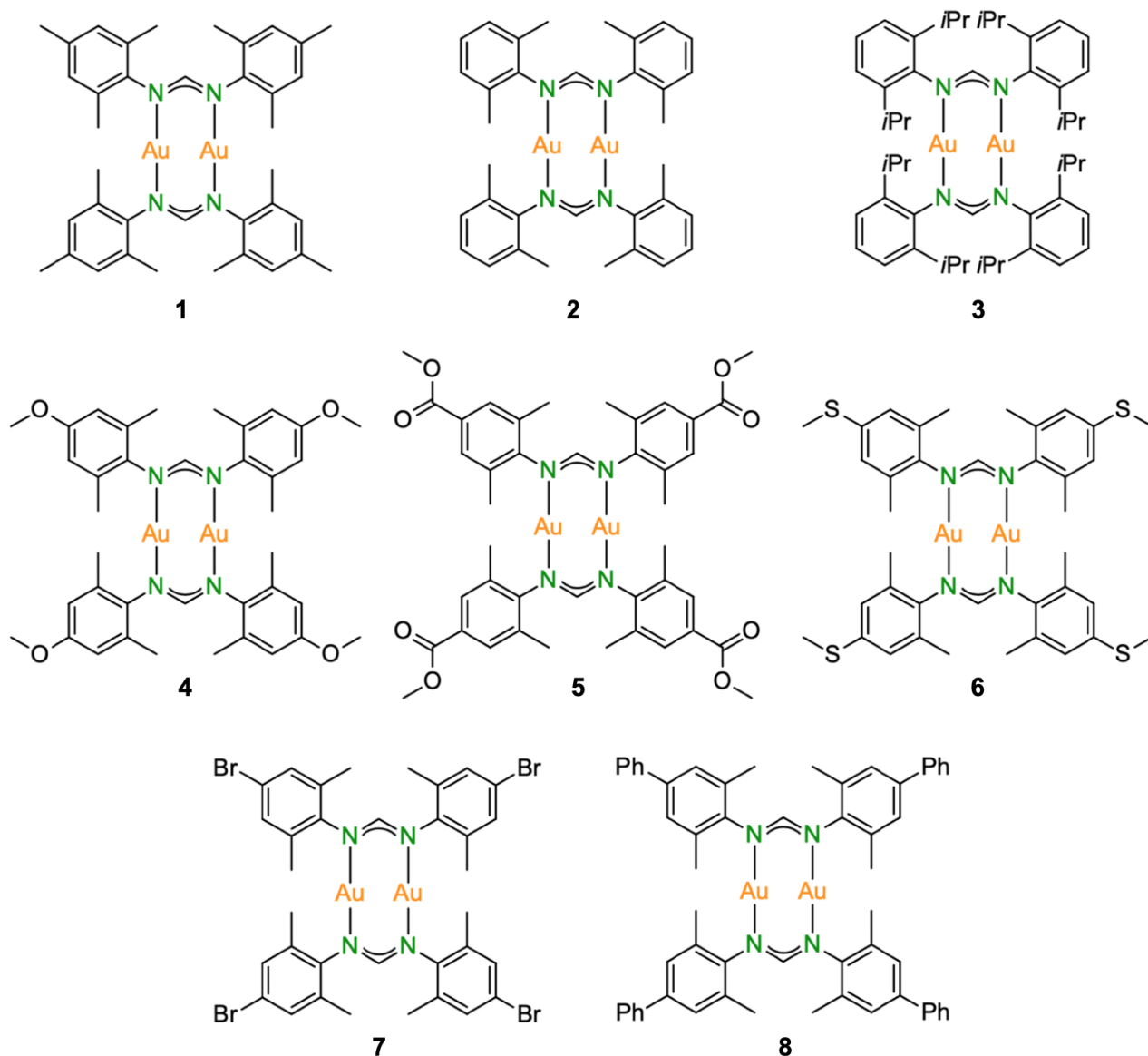


Figure 8.1: Structures of the bimetallic gold(I) amidinate model systems.

8.2 Structural examination and geometry optimization

Figure 8.1 shows the eight model compounds that will be investigated in this work. The steric modification includes the isopropyl group (complex 3), and the electronic modification includes the electron-donating methyl (complex 1), phenyl (complex 8), methoxy (complex 4), methylthio (complex 6) groups, and the electron-withdrawing methoxycarbonyl (complex 5) and bromo (complex 7) groups.

In the solid state structures, the intermetallic Au \cdots Au distances range from 2.711 to 2.738 Å, which are rather similar for different systems (Table 8.1). The Au \cdots Au distances are all much shorter than twice the van der Waals radius of gold (3.32 Å)^[81], indicating the prominent aurophilic interactions. In the quantum chemical calculation, all geometries were optimized in C_i symmetry at the PBE0-D3(BJ)/def2-TZVP level of theory except for complex **3** (in C_1 symmetry) and complex **7** (in C_2 symmetry). The ground-state (S_0) geometries are in good agreement with the X-ray diffraction analyses, only featuring slightly longer Au \cdots Au distances (around 2.751 Å), which are extremely similar for all complexes.

Table 8.1: Intermetallic Au \cdots Au distances based on the X-ray diffraction analyses (XRD) and quantum chemical calculations (DFT).

$r(\text{Au}\cdots\text{Au})/\text{Å}$	1	2	3	4	5	6	7	8
XRD	2.727	2.711	2.738	2.714	2.719	n.a.	2.720	2.737
DFT	2.753	2.753	2.746	2.752	2.751	2.751	2.751	2.752

The two-body dispersion energies, which are closely related to the distances, are presented in Table 8.2. It can be seen that though the dispersion energies for the ligands vary substantially among different complexes, they remain the same for the metal core. This is easy to understand since the Au–Au terms are rather small or even neglectable compared to the L–L terms. Therefore, the steric or electronic modifications on the ligands have almost no effect on the Au \cdots Au distances. Moreover, the partial charges of the gold centers are calculated via a natural population analysis (NPA), which gives pretty much the same results for all the complexes (Table 8.3). This further confirms that the electron donating or withdrawing substituents on the ligands have rather minor effects on the electronic state of the gold atoms.

Table 8.2: Two-body dispersion energies for the metal core (Au–Au) and the ligands (L–L).

$E_{\text{disp}}/\text{kcal}$	1	2	3	4	5	6	7	8
Au–Au	-0.941	-0.941	-0.941	-0.941	-0.941	-0.941	-0.941	-0.941
L–L	-63.030	-55.705	-100.861	-65.173	-71.816	-71.348	-61.756	-91.225

Table 8.3: Calculated partial charges of Au atoms based on a natural population analysis (NPA).

partial charge/e	1	2	3	4	5	6	7	8
Au	0.498	0.502	0.514	0.494	0.510	0.498	0.502	0.502

8.3 Excited state calculations at the S_0 geometry

At the ground-state geometries, the absorption spectra were calculated with CD-evGW/BSE employing the PBE0 functional and def2-TZVP basis set, and the predicted spectra are displayed in Figure 8.2.

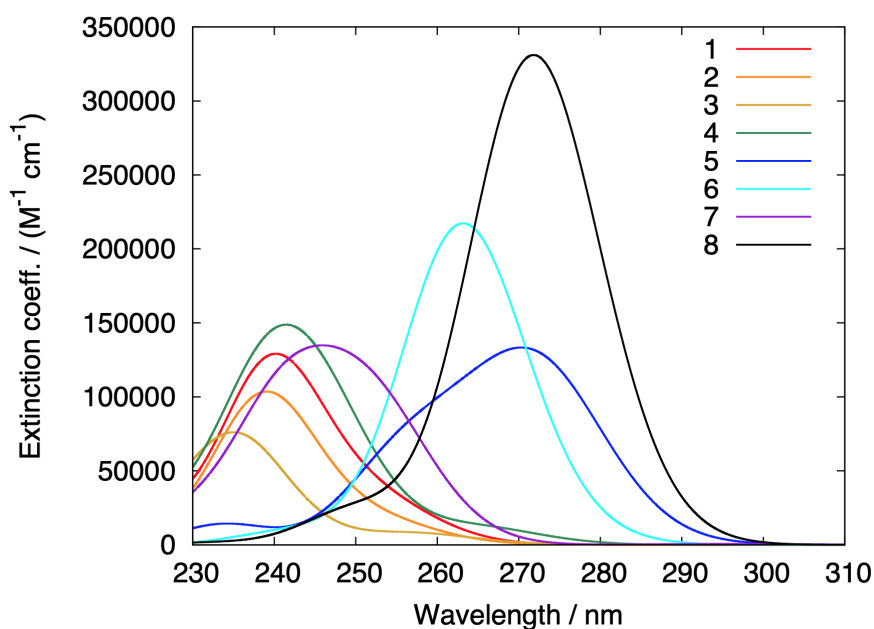


Figure 8.2: Absorption spectra (FWHM = 0.3 eV) of complexes 1–8 calculated using PBE0 evGW-BSE/def2-TZVP at the optimized S_0 geometries.

The three alkyl substituted complexes **1**, **2** and **3** exhibit very similar absorption profile (red, orange and yellow lines). For complexes **1** and **2**, the absorption peak at 240 nm and 239 nm originates from two degenerate excited states with metal-to-ligand charge-transfer (MLCT) character, and the *para*-substituted complex **1** shows a slightly higher absorption intensity. After introducing bulkier isopropyl groups, the predicted absorption spectrum of complex **3** is slightly blueshifted (235 nm) with decreased intensity.

The introduction of the electron donating methoxy groups does not alter the absorption profile of complex 4 (green line) obviously, only resulting in slightly higher intensity of the MLCT peak centered at 241 nm. However, when methoxy groups are replaced by methylthio groups, significant redshift (263 nm) and increased intensity is observed in the predicted absorption spectrum of complex 6 (cyan line). On the other hand, after introducing the electron withdrawing methoxycarbonyl and bromo groups, the predicted absorption spectra of complex 5 (blue line) and complex 7 (violet line) feature a broad MLCT absorption band centered at 270 nm and 246 nm, respectively. Interestingly, the phenyl substituted complex 8 shows the most redshifted absorption peak (272 nm) with the largest intensity (black line).

The transition density plots for the MLCT transitions in a few selected complexes are presented in Figure 8.3. The electron donating and withdrawing properties of the substituents are reflected in the change of electron density. However, the charge-transfer from the gold center to the aromatic groups of the amidinate ligands does not obviously differ, and is actually quite similar among all the complexes. Therefore, the electronic effects of the ligands on the absorption properties are very limited.

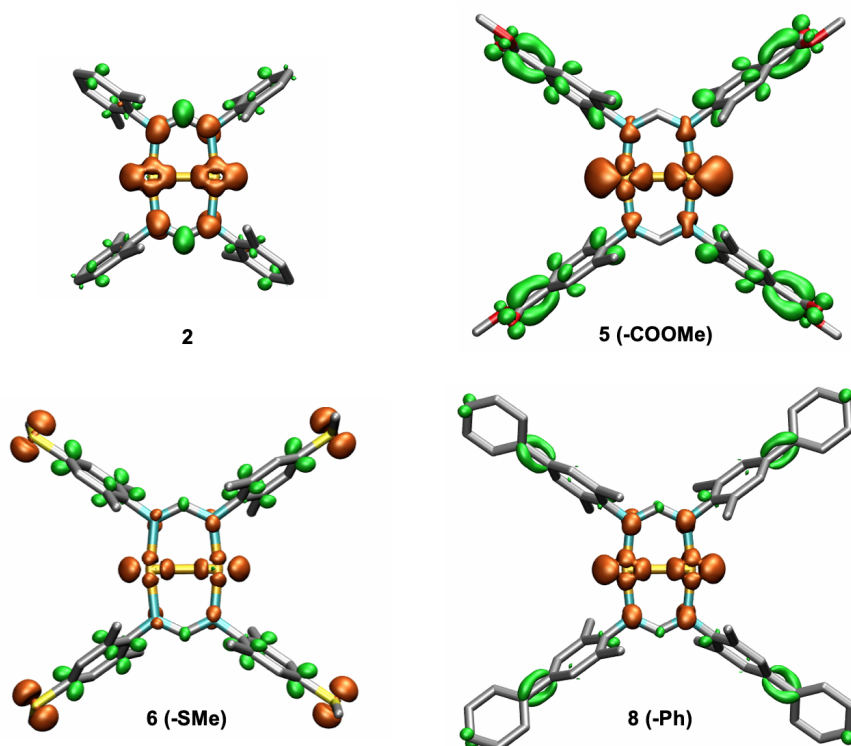


Figure 8.3: Transition density plots for the MLCT absorption bands of complexes 2, 5, 6 and 8 (isovalue: $\pm 0.0015a_0^{-3}$, all hydrogen atoms are omitted for clarity). Green represents a gain of electron density whereas orange represents a loss of electron density.

8.4 Two-component excited state calculations at the T_1 geometry

The optimized structure of the first triplet excited state (T_1) removes the coplanarity of the ground-state geometry. The central carbon atom of one amidinate ligand is located out of the Au_2N_4 plane. The phenyl substituted complex **8** is the only exception, where the coplanarity of two gold atoms with the central carbon and two nitrogen atoms of both amidinate ligands is better retained.

At the optimized T_1 geometries, two-component (2c) CD-evGW/BSE calculations using the dhf-TZVP-2c basis set were performed to investigate luminescence properties. Note that for complex **8**, the dhf-SV(P)-2c basis set was used for all atoms in the *para*-substituted phenyl rings in order to facilitate the computation. The predicted spectra are displayed in Figure 8.4. For complexes 1–7, the typical MLCT peak in the visible range is now split into two distinct (shoulder) peaks, and the high-energy peak consists of one component of the second triplet excited state (T_2), which starts to gain intensity from strong mixing with the singlet states. This is also the most intense triplet excitation in the energetic range between S_1 and T_1 . The phenyl substituted complex **8** shows no MLCT peak in the visible range, only a high-intensity peak in the UV region, which is assigned to ligand-centered transitions. This could be related to the structure, since complex **8** possesses a slightly different T_1 geometry from all the other complexes.

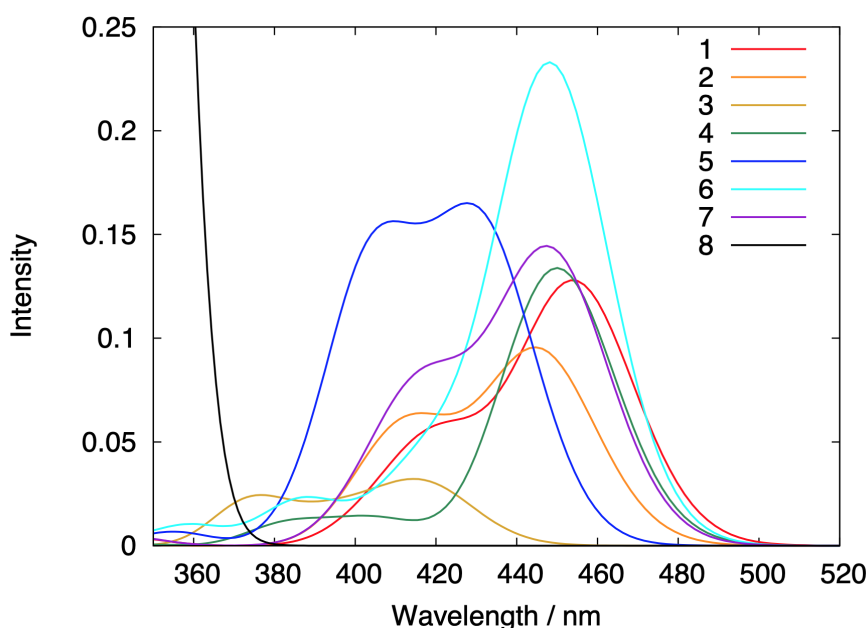


Figure 8.4: Emission spectra (FWHM = 0.2 eV) of complexes 1–8 calculated using PBE0 evGW-BSE/dhf-TZVP-2c at the optimized T_1 geometries.

Table 8.4: First and second triplet excitations T₁ and T₂ for gold complexes 1–7 at the optimized T₁ geometries. Excitation energies of triplets are given at their center of mass. Oscillator strengths f and electric dipole radiative lifetime τ are taken from the most intense component.

	1	2	3	4
T ₁ /eV (nm)	1.93 (641)	1.99 (624)	2.25 (550)	1.98 (625)
f ₁ /a.u.	4.274×10 ⁻⁵	4.460×10 ⁻⁵	1.885×10 ⁻⁵	3.059×10 ⁻⁵
τ ₁ /μs	144	131	241	191
T ₂ /eV (nm)	2.91 (426)	2.95 (420)	3.09 (401)	3.05 (407)
f ₂ /a.u.	4.571×10 ⁻²	4.728×10 ⁻²	1.493×10 ⁻²	1.241×10 ⁻²
τ ₂ /μs	0.058	0.055	0.158	0.199
	5	6	7	
T ₁ /eV (nm)	2.18 (569)	2.03 (612)	1.99 (623)	
f ₁ /a.u.	1.142×10 ⁻⁴	6.224×10 ⁻⁵	4.584×10 ⁻⁵	
τ ₁ /μs	42.5	90.1	127	
T ₂ /eV (nm)	3.01 (412)	2.95 (420)	2.91 (423)	
f ₂ /a.u.	1.284×10 ⁻¹	4.378×10 ⁻²	6.764×10 ⁻²	
τ ₂ /μs	0.019	0.060	0.039	

The calculated triplet excitation energies as well as oscillator strengths and lifetimes (in the mixed velocity/length representation) are listed in Table 8.4. All complexes turn out to present similar lifetimes in the range of tens or few hundreds of microseconds/nanoseconds. Unfortunately, the experimental photophysical data are not available yet, and hence a direct comparison between measured and predicted values is not possible at the moment.

An NTO analysis further confirms the MLCT character of the triplet excited states for complexes 1–7. The NTOs are quite similar among all the complexes, and those of complex 2 are presented in Figure 8.5 as an example. Due to the distorted symmetry, the electron density is not evenly distributed on two amidinate ligands anymore, but exclusively centered on one side where the central carbon atom is located out of the Au₂N₄ plane.

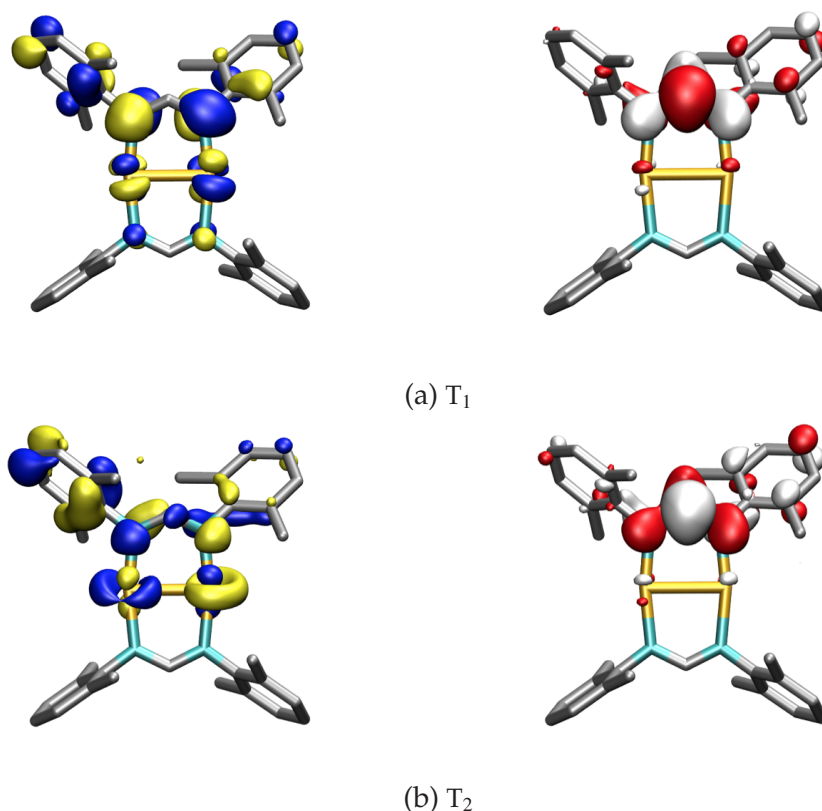


Figure 8.5: Dominating occupied (blue/yellow) and virtual (red/white) natural transition orbitals (NTOs, iso-value: $\pm 0.04a_0^{-3/2}$) of the (a) first triplet excitation T_1 and (b) second triplet excitation T_2 of complex 2. All hydrogen atoms are omitted for clarity.

8.5 Conclusion

In summary, a series of simple bimetallic gold(I) amidinate model complexes with various steric and electronic modifications on the ligands have been investigated theoretically. Both X-ray diffraction analyses and theoretical calculations show that the Au \cdots Au distances in all complexes are very similar, indicating that different substituents on the amidinate ligands have little influence on bringing the metal atoms together or pulling them apart. Likewise, the calculated absorption and emission spectra exhibit similar MLCT character among the complexes bearing different electron donating or withdrawing groups. This further confirms that the effects of the amidinate ligands on the electronic state of the gold(I) atoms are rather minor. Therefore, suggestions for further synthetic work would be that instead of modifying the ligand structures of the dinuclear gold(I) amidinate complexes, substituents should be directly bonded to the metal core via oxidative-addition reaction, which can lead to significant changes in the Au \cdots Au distances. For example, in Ref. 111, the oxidative addition of benzoyl peroxide to a bimetallic gold(I) amidinate complex (same as 2 in this work) resulted in the first stable

bimetallic Au(II) amidinate complex possessing Au–O bonds, which has the shortest Au···Au distance (2.48 Å) known for Au(II) amidinate complex. Such gold(II) amidinate complexes are probably better models for investigating the electronic influence of structural modifications on the photophysical properties.

9 Summary

In this thesis, the optical properties of mono- and oligonuclear transition metal complexes were investigated theoretically. Coinage metal (Cu, Ag, Au) complexes have attracted increasing chemical interest for their potential applications in optical devices such as efficient emitters for new OLED materials and photocatalysis for small-molecule activation. The determination of important experimental and theoretical spectroscopic data is crucial for the characterization of their photoresponse, including absorption spectra and assignment of transitions, quantum yields and lifetimes of electronically excited states, correlation between ground- and excited-state molecular structures and optical properties. Theoretical spectroscopy can provide more insight into the nature of electronic transitions, help to interpret the experimental UV/Vis absorption and luminescence spectra, and give a hint for future design of model systems. Nevertheless, challenges are that charge-transfer excitations play a critical role in the transition metal complexes, and a balance between accuracy and efficiency should be achieved for large systems of hundreds of atoms. The time-dependent density functional theory (TDDFT) has been the most popular *ab initio* method for excited-state calculations in large complexes due to its favorable scaling with respect to system size. However, charge-transfer states are particularly problematic for standard functionals. Therefore, an equally efficient computational protocol in the framework of the Bethe–Salpeter equation (BSE) was employed and validated in this work.

First of all, the performance of BSE with different GW starting points has been extensively assessed regarding singlet and triplet valence excited states as well as charge-transfer states of small to medium-sized organic molecules. The partially self-consistent GW schemes, namely eigenvalue-only self-consistent GW (evGW) and quasiparticle self-consistent GW (qsGW) have shown comparable accuracy to TDDFT in the case of valence states. The systematic underestimation of triplet excitation energies of GW/BSE, which is also a well-known problem for TDDFT, can be easily cured by a hybrid BSE/TDDFT ansatz, namely correlation-kernel-augmented BSE (cBSE). For the charge-transfer states, the GW/BSE results are in very good agreement with the reference values, which is a remarkable advantage over TDDFT. The CPU times for the TDDFT and BSE methods are of the same order of magnitude due to the same scaling. For the GW part, the CPU times for the qsGW calculations are an order of magnitude larger than for the evGW case since many more iterations are needed to converge the calcula-

tions. Given the fact that no significant advantage of qsGW in comparison with evGW has been observed, the latter is recommended for real-world applications of the BSE formalism.

Furthermore, the low-scaling AC-GW and CD-GW variants have made calculations feasible for large systems. Both schemes were applied to a triangular silver(I) hydride complex with hundreds of atoms and thousands of basis functions, and the MLCT absorption peaks from the experimental spectra were excellently reproduced in the calculations. In fact, CD-GW is equivalent to AC-GW when only HOMO and LUMO are optimized. If more orbitals are included in the calculation, then the resulting excitation energies will more closely resemble the standard GW that computes the quasiparticle energies for *all* orbital levels, and also the computation will be more demanding. Nevertheless, it has been shown that when 10 highest occupied and 10 lowest unoccupied orbitals are optimized, the convergence of calculated excitation energies are nearly reached. Therefore, in general, it is more than enough to optimize 10 highest occupied and 10 lowest unoccupied orbitals for a CD-GW calculation. This scheme was further applied to a tetranuclear silver(I) iodide complex, and the predicted (X+M)LCT absorption band of the cubane-like isomer was in good agreement with the experiment too. Besides, according to the calculations, a chair-like isomer also exists, exhibiting a slightly blueshifted (X+M)LCT peak.

For a series of heteroleptic copper(I) complexes with chelating diimine and diphosphine ligands, the absorption spectra and excited-state structures were studied. Complexes with a charged [Cu(NN)(PP)] core exhibit prominent MLCT absorptions in the relatively low-energy visible region, which is further redshifted for the dinuclear species as a result of cooperative effect. This property has been observed in both experimental and theoretical spectroscopy, making them very attractive candidates for new photosensitizers based on earth-abundant metals. For the complexes with a neutral core, the LC transitions are dominating at the equilibrium structure. The excited state flattening distortions of the tetrahedral [Cu(NN)(PP)] core are rather minor, which is favorable for their potential use as photosensitizer in solar energy conversion.

The photophysical properties of a series of highly luminescent gold(III) pincer complexes were investigated by one- and two-component computations. The electronic influence of the non-palindromic pincer ligand and the non-radiative relaxation pathways of the phenylacetylene ligand have been successfully clarified by the calculations, which in combination with the experimental results provide a basis for further studies on systematically tuning the photophysical properties with different functional groups in the pincer moieties. Likewise, a series of bimetallic gold(I) amidinate model complexes were investigated regarding the effects of different ligands on the photophysical properties. The calculated absorption and emission spectra turned out to exhibit similar MLCT feature among the complexes with various steric and electronic substituents on the ligands, indicating that the effects of the amidinate ligands on the

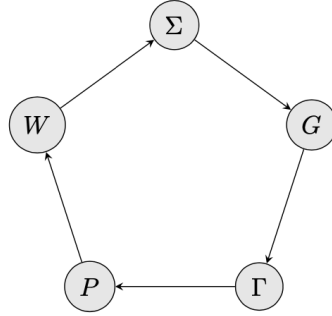
electronic state of the gold(I) centers are rather minor. Therefore, it is suggested that structural modifications should be made directly on the gold atoms.

Overall, the CD-evGW/BSE method has presented a balanced description for all the complexes involved in this thesis, and thus its applicability to d^8/d^{10} transition metal complexes has been successfully validated. In contrast, the TDDFT method employing the CAM-B3LYP functional, which adds the long-range correction in order to fix the charge-transfer problems for standard functionals, tends to overestimate the excitation energies and yield strongly blueshifted absorption spectra in some cases. Future studies include further refinement of experimental and theoretical approaches towards excited-state structure determination, lifetimes of electronically excited states and relaxation pathways, and search of suitable model systems for interpretation of cooperative effects as well as correlations between molecular structure and photophysical properties. Combined efforts from both experiment and theory are essential for a better understanding of excited state transitions and optical properties of transition metal complexes.

A Appendix

A.1 Diagrammatic representation

Hedin's equations are five coupled integral equations



$$\Sigma(1,2) = i \int d(34) G(1,3) \Gamma(3,4;2) W(4,1^+) \quad (\text{A.1})$$

$$G(1,2) = G_0(1,2) + \int d(34) G_0(1,3) \Sigma(3,4) G(4,2) \quad (\text{A.2})$$

$$\Gamma(1,2;3) = \delta(1,2)\delta(1,3) + \int d(4567) \frac{\delta \Sigma(1,2)}{\delta G(4,5)} G(4,6) \Gamma(6,7;3) G(7,5) \quad (\text{A.3})$$

$$P(1,2) = -i \int d(34) G(1,3) \Gamma(3,4;2) G(4,1^+) \quad (\text{A.4})$$

$$W(1,2) = v(1,2) + \int d(34) v(1,3) P(3,4) W(4,2) \quad (\text{A.5})$$

A diagrammatic representation of Hedin's equations is shown in Fig. A.1. The Green's functions G_0 and G are denoted by single and double straight lines with arrows, respectively. The bare and screened Coulomb interaction V and W are denoted by single and double wiggly lines, respectively.

And for the Bethe–Salpeter equation

$$L(1,2;3,4) = L_0(1,2;3,4) + \int d(5678) L_0(1,6;3,5) K(5,8;6,7) L(7,2;8,4) \quad (\text{A.6})$$

$$K(5,6,7,8) = \delta(5,6)\delta(7,8)v(5,7) - \delta(5,7)\delta(6,8)W(5,6) \quad (\text{A.7})$$

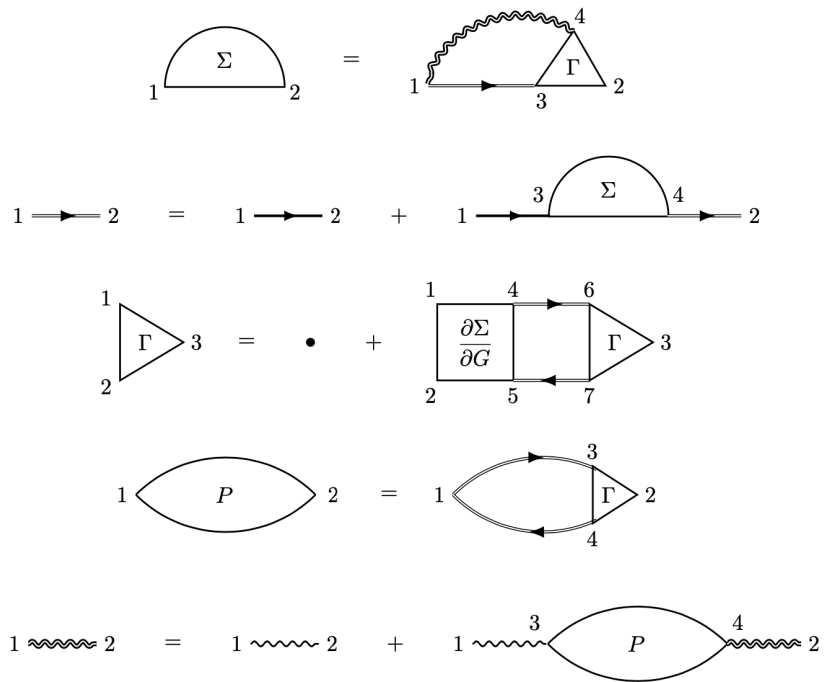


Figure A.1: Diagrammatic representation of Hedin's equations

the diagrammatic representation is shown in Fig. A.2.

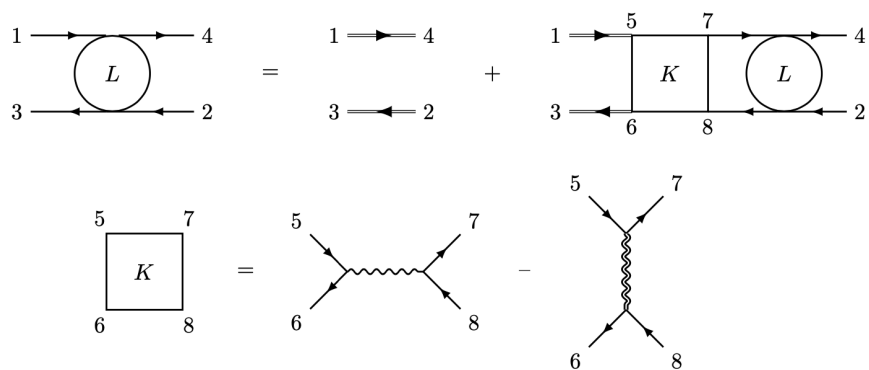


Figure A.2: Diagrammatic representation of the Bethe-Salpeter equation

B List of Publications

- 2020 W. Feuerstein, C. Holzer, **X. Gui**, L. Neumeier, W. Klopper, F. Breher. *Synthesis of new donor-substituted biphenyls: Pre-ligands for highly luminescent (C[∧]C[∧]D) gold(III) pincer complexes*. Chem. Eur. J. 26, 17156 (2020).
- 2019 S. V. Kruppa, C. Groß, **X. Gui**, F. Bäßler, B. Kwasigroch, Y. Sun, R. Diller, W. Klopper, G. Niedner-Schatteburg, C. Riehn, W. R. Thiel. *Photoinitiated charge transfer in a triangular silver(I) hydride complex and its oxophilicity*. Chem. Eur. J. 25, 11269 (2019).
- 2018 C. Holzer, **X. Gui**, M. E. Harding, G. Kresse, T. Helgaker, W. Klopper. *Bethe–Salpeter correlation energies of atoms and molecules*. J. Chem. Phys. 149, 144106 (2018).
- 2018 **X. Gui**, C. Holzer, W. Klopper. *Accuracy assessment of GW starting points for calculating molecular excitation energies using the Bethe–Salpeter formalism*. J. Chem. Theory Comput. 14, 2127 (2018).

C Permissions for reuse or republication

This work partly contains material that has already been published in scientific journals. Permissions for reuse or reprint of the relevant content has been obtained from the corresponding publisher/copyright owner.

- Chap. 3: adapted in part with permission from *Accuracy Assessment of GW Starting Points for Calculating Molecular Excitation Energies Using the Bethe–Salpeter Formalism*, X. Gui, C. Holzer, W. Klopper, *J. Chem. Theory Comput.* **14**, 2127 (2018). Copyright 2018 American Chemical Society.
- Chap. 4: adapted in part with permission from *Photoinitiated Charge Transfer in a Triangular Silver(I) Hydride Complex and Its Oxophilicity*, S. V. Kruppa, C. Groß, X. Gui, F. Bäßler, B. Kwasigroch, Y. Sun, R. Diller, W. Klopper, G. Niedner-Schatteburg, C. Riehn, W. R. Thiel, *Chem. Eur. J.* **25**, 11269 (2019). Copyright 2019 John Wiley & Sons.
- Chap. 7: adapted in part with permission from *Synthesis of New Donor-Substituted Biphenyls: Pre-ligands for Highly Luminescent (C⁺C⁻D) Gold(III) Pincer Complexes*, W. Feuerstein, C. Holzer, X. Gui, L. Neumeier, W. Klopper, F. Breher, *Chem. Eur. J.* **26**, 17156 (2020). Copyright 2020 John Wiley & Sons.

Bibliography

- [1] Niedner-Schatteburg, G. In *Clusters – Contemporary Insight in Structure and Bonding*; Dehnen, S., Ed.; Springer International Publishing: Cham, 2017.
- [2] Laurent, A. D.; Jacquemin, D. *Int. J. Quantum Chem.* **2013**, *113*, 2019.
- [3] Ziaei, V.; Bredow, T. *J. Phys.: Condens. Matter* **2018**, *30*, 395501.
- [4] Holzer, C.; Klopper, W. *J. Chem. Phys.* **2018**, *149*, 101101.
- [5] Gui, X.; Holzer, C.; Klopper, W. *J. Chem. Theory Comput.* **2018**, *14*, 2127.
- [6] Blase, X.; Duchemin, I.; Jacquemin, D. *Chem. Soc. Rev.* **2018**, *47*, 1022.
- [7] Ziaei, V.; Bredow, T. *Phys. Rev. B* **2017**, *96*, 195115.
- [8] Rangel, T.; Hamed, S. M.; Bruneval, F.; Neaton, J. B. *J. Chem. Phys.* **2017**, *146*, 194108.
- [9] Hung, L.; Bruneval, F.; Baishya, K.; Ögüt, S. *J. Chem. Theory Comput.* **2017**, *13*, 2135.
- [10] Azarias, C.; Habert, C.; Budzák, Š.; Blase, X.; Duchemin, I.; Jacquemin, D. *J. Phys. Chem. A* **2017**, *121*, 6122.
- [11] Jacquemin, D.; Duchemin, I.; Blase, X. *J. Phys. Chem. Lett.* **2017**, *8*, 1524.
- [12] Escudero, D.; Duchemin, I.; Blase, X.; Jacquemin, D. *J. Phys. Chem. Lett.* **2017**, *8*, 936.
- [13] Jacquemin, D.; Duchemin, I.; Blondel, A.; Blase, X. *J. Chem. Theory Comput.* **2017**, *13*, 767.
- [14] Azarias, C.; Duchemin, I.; Blase, X.; Jacquemin, D. *J. Chem. Phys.* **2017**, *146*, 034301.
- [15] Ziaei, V.; Bredow, T. *J. Chem. Phys.* **2016**, *145*, 174305.
- [16] Bruneval, F.; Rangel, T.; Hamed, S. M.; Shao, M.; Yang, C.; Neaton, J. B. *Comput. Phys. Comm.* **2016**, *208*, 149.
- [17] Cardia, R.; Mallocci, G.; Rignanese, G.-M.; Blase, X.; Molteni, E.; Cappellini, G. *Phys. Rev. B* **2016**, *93*, 235132.

- [18] Blase, X.; Boulanger, P.; Bruneval, F.; Fernandez-Serra, M.; Duchemin, I. *J. Chem. Phys.* **2016**, *144*, 034109.
- [19] Jacquemin, D.; Duchemin, I.; Blondel, A.; Blase, X. *J. Chem. Theory Comput.* **2016**, *12*, 3969.
- [20] Duchemin, I.; Jacquemin, D.; Blase, X. *J. Chem. Phys.* **2016**, *144*, 164106.
- [21] Jacquemin, D.; Duchemin, I.; Blase, X. *Mol. Phys.* **2016**, *114*, 957.
- [22] Jacquemin, D.; Duchemin, I.; Blase, X. *J. Chem. Theory Comput.* **2015**, *11*, 5340.
- [23] Jacquemin, D.; Duchemin, I.; Blase, X. *J. Chem. Theory Comput.* **2015**, *11*, 3290.
- [24] Blase, X.; Attaccalite, C. *Appl. Phys. Lett.* **2011**, *99*, 171909.
- [25] Duchemin, I.; Deutsch, T.; Blase, X. *Phys. Rev. Lett.* **2012**, *109*, 167801.
- [26] van Setten, M. J.; Weigend, F.; Evers, F. *J. Chem. Theory Comput.* **2013**, *9*, 232.
- [27] Koval, P.; Foerster, D.; Sánchez-Portal, D. *Phys. Rev. B* **2014**, *89*, 155417.
- [28] Caruso, F.; Rinke, P.; Ren, X.; Rubio, A.; Scheffler, M. *Phys. Rev. B* **2013**, *88*, 075105.
- [29] Caruso, F.; Rinke, P.; Ren, X.; Scheffler, M.; Rubio, A. *Phys. Rev. B* **2012**, *86*, 081102.
- [30] Blase, X.; Attaccalite, C.; Olevano, V. *Phys. Rev. B* **2011**, *83*, 115103.
- [31] van Schilfgaarde, M.; Kotani, T.; Faleev, S. *Phys. Rev. Lett.* **2006**, *96*, 226402.
- [32] Kaplan, F.; Harding, M. E.; Seiler, C.; Weigend, F.; Evers, F.; van Setten, M. J. *J. Chem. Theory Comput.* **2016**, *12*, 2528.
- [33] Govoni, M.; Galli, G. *J. Chem. Theory and Comput.* **2015**, *11*, 2680.
- [34] Wilhelm, J.; Del Ben, M.; Hutter, J. *J. Chem. Theory Comput.* **2016**, *12*, 3623.
- [35] Vlček, V.; Rabani, E.; Neuhauser, D.; Baer, R. *J. Chem. Theory Comput.* **2017**, *13*, 4997.
- [36] Golze, D.; Wilhelm, J.; van Setten, M. J.; Rinke, P. *J. Chem. Theory Comput.* **2018**, *14*, 4856.
- [37] Szabo, A.; Ostlund, N. S. *Modern Quantum Chemistry: Introduction to Advanced Electronic Structure Theory*; Dover Publications: New York, 1996.
- [38] Levine, I. N. *Quantum Chemistry*, 7th ed.; Pearson: London, 2014.
- [39] Jensen, F. *Introduction to Computational Chemistry*, 3rd ed.; Wiley: Chichester, 2017.

- [40] McWeeny, R. *Methods of molecular quantum mechanics*, 2nd ed.; Academic Press: London, 1992.
- [41] Casida, M. E. In *Recent advances in density functional methods*; Chong, D. P., Ed.; World Scientific: Singapor, 1995; Chapter 5.
- [42] Onida, G.; Reinin, L.; Rubio, A. *Rev. Mod. Phys.* **2002**, *74*, 601.
- [43] Bruneval, F.; Ph.D. thesis; Ecole Polytechnique; 2005.
- [44] Hohenberg, P.; Kohn, W. *Phys. Rev.* **1964**, *136*, B864.
- [45] Kohn, W.; Sham, L. J. *Phys. Rev.* **1965**, *140*, A1133.
- [46] Mahan, G. D. *Many-Particle Physics*, 3rd ed.; Springer Science+Business Media: New York, 2013.
- [47] Hirata, S.; Head-Gordon, M. *Chem. Phys. Lett.* **1999**, *314*, 291.
- [48] Dyson, F. J. *Phys. Rev.* **1949**, *75*, 486.
- [49] Dyson, F. J. *Phys. Rev.* **1949**, *75*, 1736.
- [50] Hedin, L. *Phys. Rev.* **1965**, *139*, A796.
- [51] Hedin, L.; Lundqvist, S. *Solid State Physics* **1970**, *23*, 1.
- [52] Salpeter, E. E.; Bethe, H. A. *Phys. Rev.* **1951**, *84*, 1232.
- [53] Faleev, S. V.; van Schilfgaarde, M.; Kotani, T. *Phys. Rev. Lett.* **2004**, *93*, 126406.
- [54] Holzer, C.; Klopper, W. *J. Chem. Phys.* **2019**, *150*, 204116.
- [55] Furche, F.; Ahlrichs, R.; Hättig, C.; Klopper, W.; Sierka, M.; Weigend, F. *WIREs: Comput. Mol. Sci.* **2014**, *4*, 91.
- [56] TURBOMOLE V7.4 2019, a development of University of Karlsruhe and Forschungszentrum Karlsruhe GmbH, 1989-2007, TURBOMOLE GmbH, since 2007; <http://www.turbomole.com>.
- [57] Andrae, D.; Häußermann, U.; Dolg, M.; Stoll, H.; Preuß, H. *Theor. Chem. Acc.* **1990**, *77*, 123.
- [58] Weigend, F.; Ahlrichs, R. *Phys. Chem. Chem. Phys.* **2005**, *7*, 3297.
- [59] Weigend, F.; Baldes, A. *J. Chem. Phys.* **2010**, *133*, 174102.

- [60] Figgen, D.; Rauhut, G.; Dolg, M.; Stoll, H. *Chemical Physics* **2005**, *311*, 227.
- [61] Williams, T.; Kelley, C.; et al.; Gnuplot V4.2 2009: an interactive plotting program; <http://gnuplot.sourceforge.net>.
- [62] Humphrey, W.; Dalke, A.; Schulten, K. *J. Mol. Graph.* **1996**, *14*, 33.
- [63] Schreiber, M.; Silva-Junior, M. R.; Sauer, S. P. A.; Thiel, W. *J. Chem. Phys.* **2008**, *128*, 134110.
- [64] Silva-Junior, M. R.; Sauer, S. P. A.; Schreiber, M.; Thiel, W. *Mol. Phys.* **2010**, *108*, 453.
- [65] Silva-Junior, M. R.; Schreiber, M.; Sauer, S. P. A.; Thiel, W. *J. Chem. Phys.* **2010**, *133*, 174318.
- [66] Kánnár, D.; Szalay, P. G. *J. Chem. Theory Comput.* **2014**, *10*, 3757.
- [67] Kánnár, D.; Szalay, P. G. *J. Mol. Model.* **2014**, *20*, 2503.
- [68] Perdew, J. P.; Burke, K.; Ernzerhof, M. *Phys. Rev. Lett.* **1996**, *77*, 3865.
- [69] Ernzerhof, M.; Scuseria, G. E. *J. Chem. Phys.* **1999**, *110*, 5029.
- [70] Jacquemin, D.; Duchemin, I.; Blondel, A.; Blase, X. *J. Chem. Theory Comput.* **2017**, *13*, 767.
- [71] Peach, M. J. G.; Benfield, P.; Helgaker, T.; Tozer, D. J. *J. Chem. Phys.* **2008**, *128*, 044118.
- [72] Krause, K.; Klopper, W. *J. Comp. Chem.* **2017**, *38*, 383.
- [73] Thilgen, C.; Herrmann, A.; Diederich, F. *Helv. Chim. Acta* **1997**, *80*, 183.
- [74] Hawkins, J. M.; Nambu, M.; Meyer, A. *J. Am. Chem. Soc.* **1994**, *116*, 7642.
- [75] Crassous, J.; Rivera, J.; Fender, N. S.; Shu, L.; Echegoyen, L.; Thilgen, C.; Herrmann, A.; Diederich, F. *Angew. Chem. Int. Ed.* **1999**, *38*, 1613.
- [76] Furche, F.; Ahlrichs, R. *J. Am. Chem. Soc.* **2002**, *124*, 3804.
- [77] Jiemchooraj, A.; Norman, P. *J. Chem. Phys.* **2007**, *126*, 134102.
- [78] Hidalgo, F.; Noguez, C. *Phys. Status Solidi B* **2010**, *247*, 1889.
- [79] Jordan, A. J.; Lalic, G.; Sadighi, J. P. *Chem. Rev.* **2016**, *116*, 8318.
- [80] Perutz, R. N.; Procacci, B. *Chem. Rev.* **2016**, *116*, 8506.
- [81] Bondi, A. *J. Phys. Chem.* **1964**, *68*, 441.
- [82] Kruppa, S. V.; Groß, C.; Gui, X.; Bäppler, F.; Kwasigroch, B.; Sun, Y.; Diller, R.; Klopper, W.; Niedner-Schatteburg, G.; Riehn, C.; Thiel, W. *Chem. Eur. J.* **2019**, *25*, 11269.

- [83] Grimme, S.; Antony, J.; Ehrlich, S.; Krieg, H. *J. Chem. Phys.* **2010**, *132*, 154104.
- [84] Grimme, S.; Ehrlich, S.; Goerigk, L. *J. Comput. Chem.* **2011**, *32*, 1456.
- [85] Teo, B.-K.; Calabrese, J. C. *Inorg. Chem.* **1976**, *15*, 2474.
- [86] Henary, M.; Zink, J. I. *Inorg. Chem.* **1991**, *30*, 3111.
- [87] Yanai, T.; Tew, D. P.; Handy, N. C. *Chem. Phys. Lett.* **2004**, *393*, 51.
- [88] Kuramochi, Y.; Itabashi, J.; Toyama, M.; Ishida, H. *ChemPhotoChem* **2018**, *2*, 314.
- [89] Yamazaki, Y.; Ohkubo, K.; Saito, D.; Yatsu, T.; Y. Tamaki; Tanaka, S.; Koike, K.; Onda, K.; Ishitani, O. *Inorg. Chem.* **2019**, *58*, 11480.
- [90] Genoni, A.; Chirdon, D. N.; Boniolo, M.; Sartorel, A.; Bernhard, S.; Bonchio, M. *ACS Catal.* **2017**, *7*, 154.
- [91] Takeda, H.; Cometto, C.; Ishitani, O.; Robert, M. *ACS Catal.* **2017**, *7*, 70.
- [92] Takeda, H.; Kamiyama, H.; Okamoto, K.; Irimajiri, M.; Mizutani, T.; Koike, K.; Sekine, A.; Ishitani, O. *J. Am. Chem. Soc.* **2018**, *140*, 17241.
- [93] Hossain, A.; Bhattacharyya, A.; Reiser, O. *Science* **2019**, *364*, eaav9713.
- [94] Minozzi, C.; Caron, A.; Grenier-Petel, J.-C.; Santandrea, J.; Collins, S. K. *Angew. Chem. Int. Ed.* **2018**, *57*, 5477.
- [95] Gracia, L.-L.; Luci, L.; Bruschi, C.; Sambri, L.; Weis, P.; Fuhr, O.; Bizzarri, C. *Chem. Eur. J.* **2020**, *26*, 9929.
- [96] Lee, C.-H.; Tang, M.-C.; Wong, Y.-C.; Chan, M.-Y.; Yam, V. W.-W. *J. Am. Chem. Soc.* **2017**, *139*, 10539.
- [97] To, W.-P.; Zhou, D.; Tong, G. S. M.; Cheng, G.; Yang, C.; Che, C.-M. *Angew. Chem. Int. Ed.* **2017**, *56*, 14036.
- [98] Lee, C.-H.; Tang, M.-C.; Cheung, W.-L.; Lai, S.-L.; Chan, M.-Y.; Yam, V. W.-W. *Chem. Sci.* **2018**, *9*, 6228.
- [99] Tang, M.-C.; Leung, M.-Y.; Lai, S.-L.; Ng, M.; Chan, M.-Y.; Yam, V. W.-W. *J. Am. Chem. Soc.* **2018**, *140*, 13115.
- [100] Li, L.-K.; Tang, M.-C.; Lai, S.-L.; Ng, M.; Kwok, W.-K.; Chan, M.-Y.; Yam, V. W.-W. *Nature Photonics* **2019**, *13*, 185.

- [101] Lam, E. S.-H.; Lam, W. H.; Yam, V. W.-W. *Inorg. Chem.* **2015**, *54*, 3624.
- [102] Fernandez-Cestau, J.; Bertrand, B.; Blaya, M.; Jones, G. A.; Penfold, T. J.; Bochmann, M. *Chem. Commun.* **2015**, *51*, 16629.
- [103] Beucher, H.; Kumar, S.; Merino, E.; Hu, W.-H.; Stemmler, G.; Cuesta-Galisteo, S.; González, J. A.; Jagielski, J.; Shih, C.-J.; Nevado, C. *Chem. Mater.* **2020**, *32*, 1605.
- [104] Tong, G. S. M.; Chan, K. T.; Chang, X.; Che, C.-M. *Chem. Sci.* **2015**, *6*, 3026.
- [105] Beucher, H.; Merino, E.; Genoux, A.; Fox, T.; Nevado, C. *Angew. Chem. Int. Ed.* **2019**, *58*, 9064.
- [106] Roşca, D. A.; Fernandez-Cestau, J.; Morris, J.; Wright, J. A.; Bochmann, M. *Sci. Adv.* **2015**, *1*, e1500761.
- [107] Feuerstein, W.; Holzer, C.; Gui, X.; Neumeier, L.; Klopfer, W.; Breher, F. *Chem. Eur. J.* **2020**, *26*, 17156.
- [108] Wong, K. M.-C.; Hung, L.-L.; Lam, W. H.; Zhu, N.; Yam, V. W.-W. *J. Am. Chem. Soc.* **2007**, *129*, 4350.
- [109] Bachmann, M.; Fessler, R.; Blacque, O.; Venkatesan, K. *Dalton Trans.* **2019**, *48*, 7320.
- [110] von Arx, T.; Szentkuti, A.; Zehnder, T. N.; Blacque, O.; Venkatesan, K. *J. Mater. Chem. C* **2017**, *5*, 3765.
- [111] Abdou, H. E.; Mohamed, A. A.; Fackler, J. P. *Inorg. Chem.* **2007**, *46*, 9692.

Acknowledgment

There are many people who have helped and supported me during the research and writing of this thesis, and hereby I would like to thank them.

First of all, I would like to express my deepest gratitude to my supervisor, Prof. Wim Klopper, for all the guidance and support throughout my PhD. Thank you for your trust in my capabilities, your words of encouragement and for always arranging time to provide prompt help or feedback. Thank you for the great freedom and flexibility to carry out the work so that I can manage my PhD while having a baby.

I also wish to thank Michael Harding for being my Korreferent and for a careful reading of this thesis as well as the valuable discussions.

Many thanks to all my (ex-)colleagues in the theoretical chemistry group for creating a friendly and relaxed atmosphere in the workplace, as well as the pleasant and joyful moments in mensa. Specifically, Christof Holzer, thank you for the fruitful collaborations and inspiring discussions, and for always being ready and patient to answer my questions; Jiří Chmela, thank you for being a cheerful officemate and flatmate who helped me settle into a new job and a new country; Florian Rehak, thank you for your timely assistance with L^AT_EX; Anna Hehn and Monika Borkowska, thank you for being compassionate and inspiring as a PhD mom.

I would also like to acknowledge the efforts of my experimental collaborators. Sebastian Kruppa, Jasmin Busch, Cecilia Bruschi and Frederic Krätschmer, thank you for the smooth communication and the great job we have done together.

Special thanks to my parents as well as the rest of my family in China, for their unconditional love, faith and support from the other side of the world. I would not be where I am today without them.

Finally, I would like to thank my daughter Amaryntha, for showing me that life is so full of unpredictable beauty and strange surprises. I am really excited about this wonderful journey together and what the future will bring.